DIRECT EXPERIMENTAL OBSERVATION OF 3D VORTEX STATES IN MULTILAYER FE/GD USING SCANNING ELECTRON MICROSCOPY WITH POLARIZATION ANALYSIS (SEMPA)

by

RICH MORASKI

A DISSERTATION

Presented to the Department of Physics
and the Division of the Graduate Studies of the University or Oregon
in partial fulfillment of the requirements
for the degree of
Doctor of Philosophy

March 2023

DISSERTATION APPROVAL PAGE

Student: Rich Moraski

Title: Direct Experimental Observation of 3D Vortex States in Multilayer Fe/Gd Using Scanning Electron Microscopy with Polarization Analysis (SEMPA)

This dissertation has been accepted and approved in partial fulfillment of the requirements for the Doctor of Philosophy degree in the Department of Physics by:

Dietrich Belitz	Chair
Benjamin McMorran	Advisor
Jayson Paulose	Core Member
Cathy Wong	Institutional Representative

and

Krista Chronister	Vice Provost for Graduate Studies

Original approval signatures are on file with the University of Oregon Division of Graduate Studies.

Degree awarded March 2023.
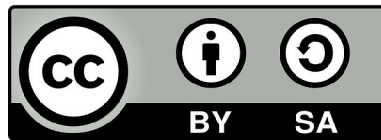
DISSERTATION ABSTRACT

Rich Moraski

Doctor of Philosophy

Department of Physics

March 2023

Title: Direct Experimental Observation of 3D Vortex States in Multilayer Fe/Gd Using Scanning Electron Microscopy with Polarization Analysis (SEMPA)

The global market for power solely for data center usage is estimated to be \$12.4 billion by 2027[1]. In 2021, data center electricity consumption was $\sim$400 TW h, representing almost 2% of the global energy demand[2]. Ongoing efforts in spintronics, which use spin currents instead of traditional charge currents at a fraction of the power[3], are paving the way for significant savings, both financially and environmentally. There has been considerable research into alternatives for memory[4–6] including a magnetic structure known as a skyrmion, a self-supporting magnetic texture characterized by a non-trivial topology. Recent advances in creating room-temperature stable skyrmions has reignited interest in these objects.

Building on previous work in the McMorran group, this research set out to build a more complete understanding of the 3D structure of metastable magnetic skyrmions, specifically in Fe/Gd thin films. This was done using traditional transmission electron microscope (TEM) techniques along with a unique scanning electron microscope with polarization analysis at the University, the SEMPA. Data collected using a TEM in Lorentz mode, providing information integrated through the bulk of the material, was combined with data from SEMPA, providing surface-sensitive information about the top of the material. Analysis of the data suggests a

topologically complex winding nature for the magnetization of skyrmions in this material.

Presented herein is a brief introduction of the magnetic structures found in Fe/Gd multilayer thin films; an analysis using new analytical tools built for this purpose of the data collected; and a user's manual for SEMPA, including maintenance and troubleshooting guidance.

CURRICULUM VITAE

NAME OF AUTHOR: Rich Moraski

GRADUATE AND UNDERGRADUATE SCHOOLS ATTENDED:
University of Oregon, Eugene, OR
George Mason University, Fairfax, VA
University of Virginia, Charlottesville, VA
Longwood University, Farmville, VA
University of Central Florida, Orlando, FL

DEGREES AWARDED:
Doctor of Philosophy, Physics, 2023, University of Oregon
Master of Science, Physics, 2019, University of Oregon
Bachelor of Science, Physics, 2017, George Mason University
Bachelor of Science, Commerce, 1992, University of Virginia

AREAS OF SPECIAL INTEREST:
Condensed Matter Physics
Electron Microscopy
Nanomagnetism
Spintronics

PROFESSIONAL EXPERIENCE:

Graduate Research Assistant, University of Oregon, Eugene, OR, 9/2017 - Present

President, Principle Consultant, Orbium Inc., Eugene, OR, 6/1997 - Present

Senior Program Director, Capital One, Mclean, VA, 12/2015 - 9/2017

Advisory Solutions Consultant for Major Accounts, ServiceNow, Mclean, VA, 9/2014 - 12/2015

Senior Director of Cloud Automation, Windward IT Solutions, Herndon, VA, 2/2012 - 9/2014

Senior Director of Knowledge Engineering, BMC Software, Herndon, VA, 7/2007 - 2/2012

Chief Architect, Director of Knowledge Engineering, RealOps, Herndon, VA, 10/2004 - 7/2007

Chief Architect, Windward Consulting Group, Herndon, VA, 1/2004 - 10/2004

Senior Associate, Booz Allen Hamilton, Vienna, VA, 5/2003 - 1/2004

Senior Manager, Bell Atlantic, Arlington, VA, 7/1992 - 6/1997

PUBLICATIONS

Rich Moraski et al. "Electron Microscopy Spin Analysis of Topological Magnetic Domains in Amorphous Fe/Gd Thin Films". In: *Microscopy and Microanalysis* 28.S1 (2022), pp. 1688–1689

Rich Moraski and Benjamin McMorran. "3D Morphology of Magnetic Bubbles in Layered Ferromagnetic Materials". In: *Microscopy and Microanalysis* 27.S1 (2021), pp. 150–152

Cameron W Johnson et al. "Exact design of complex amplitude holograms for producing arbitrary scalar fields". In: *Optics express* 28.12 (2020), pp. 17334–17346

ACKNOWLEDGEMENTS

I dedicate my dissertation work to my family and many friends. A special thank you is due to my parents, who endured my inquisitiveness from the beginning. My sister and niece, as well as my new family (if 14 years can really be called new) were also as supportive as could be.

Brandon Smith (way more than) helped ease the financial burden of being a full-time student again.

Gromit, Ripley, Wallace, Kevin, Barky, Finn, and Charlie provided unconditional love as only the four-legged can.

None of this, however, would have happened without Carla. I just might love you more than ice cream. *Maybe*.

TABLE OF CONTENTS

LIST OF FIGURES

CHAPTER I

BACKGROUND

Magnetic Bubbles

Stable, circular magnetic domains, generally dubbed magnetic bubbles, have been a topic of interest for over 60 years. Originally observed in orthoferrites, perovskites, and various oxides[7–10], they were soon engineered into thin films by Andrew Bobeck at Bell Laboratories to create "bubble memory," a promising technology at the time for non-volatile data storage due to their stability and relative ease of movement[11]. Tape storage was slow and physically large; magnetic-core memory, while fast, was limited in capacity and prohibitively expensive[12], and spinning hard drives were also still quite large and complex (the IBM 2305[13], for example, introduced in 1970, filled the equivalent of 4 racks to house 20 MB). Bubble memory required no moving parts and comparatively little power to flip bits[14]. While the investigation of wider use of bubble memory continued[15–19], hard drive and, more recently, solid state drive performance advanced at a faster pace.

Concurrently, superconductor research[20–22], often focused on UPt_3 and variants, observed the topology of magnet bubbles called magnetic skyrmions. Originally, "skyrmions" referred to stable soliton solutions of a classical field theory model for nucleons proposed by British physicist Tony Skyrme in 1961[23, 24]. The moniker of this robust, particle-like entity has since been extended to objects elsewhere, including superconductors[25–28] and magnetic materials[29–34].

In the 90's skyrmions were found in a number of thin films[35–37] and have since grown in interest for the budding field of spintronics[38–42], where magnetic
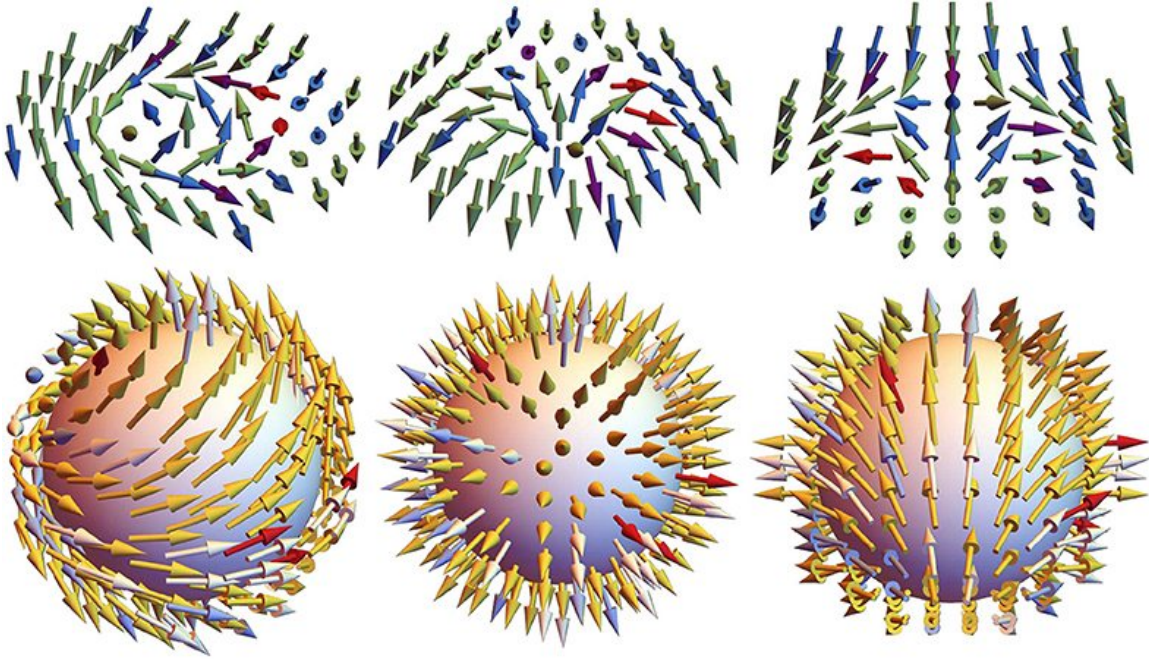
Figure 1.1. A schematic representation of a Bloch skyrmion (top left), a Néel skyrmion (top center), and an antiskyrmion (top right). Projections on the unit sphere are shown on the bottom. Figure reproduced from "Skyrmions and Antiskyrmions in Quasi-Two-Dimensional Magnets" by Kovalev, Alexey A. and Sandhoefner, Shane in Front. Phys., 27 September 2018, used under CC BY.

domains instead of electric charges are moved with a fraction of the current required for conventional electronics[3, 43, 44].

Phenomenological Description of Magnetic Skyrmions

There is some disagreement in the literature about what truly constitutes a magnetic skyrmion: some insist on a strictly mathematical definition, requiring integer values for the differential equation shown in Equation 1.3 and a specific topology induced by a particular Hamiltonian (described below in Dzyaloshinskii-Moriya interaction (DMI)), while others argue that it is the texture itself–small, stable, axisymmetric, whirling, easily moved, particle-like–that matters. This work adheres to the more practical-natured second description while still calculating values for the equation.

The two simplest magnetic skyrmions shapes, as well as a texture called an antiskyrmion, are shown schematically in Figure 1.1. Both skyrmions and antiskyrmions are more or less circular, with diameters from several 10's to a few hundred nanometers. Skyrmions are typically characterized in three dimensions as cylindrical[32, 45–47].

In both cases, the z component of the magnetization vector flips from the center of the texture to the outside (up to down or down to up). Skyrmions are most often labelled as Bloch, where the magnetization changes direction in the plane of the domain wall, or Néel, where the magnetization changes direction perpendicular to the plane of the domain wall. Figure 1.2 shows a schematic of these basic configurations.

Skyrmions and antiskyrmions can be described mathematically by parameterizing a fixed-spin model. In general,

$$\hat{\boldsymbol{m}}(\boldsymbol{r}) = \left(\cos\Phi(\boldsymbol{r})\sin\Theta(\boldsymbol{r}), \sin\Phi(\boldsymbol{r})\sin\Theta(\boldsymbol{r}), \cos\Theta(\boldsymbol{r})\right), \qquad (1.1)$$

where $\hat{\boldsymbol{m}}$ is the normalized local magnetization vector in the magnetic material. For skyrmions with cylindrical symmetry, Equation 1.1 can be expressed in spherical coordinates as

$$\hat{\boldsymbol{m}} = \left(\cos\Phi(\phi)\sin\Theta(\rho), \sin\Phi(\phi)\sin\Theta(\rho), \cos\Theta(\rho)\right), \qquad (1.2)$$

with in and out of plane components $\Theta(\rho)$ and $\Phi(\phi)$, where ρ and ϕ are the radial distance and azimuthal angles.

Magnetic skyrmions are characterized by a non-zero integer skyrmion number[48],

$$N_{\mathrm{sk}} = \frac{1}{4\pi} \int \hat{\boldsymbol{m}} \cdot (\partial_x \hat{\boldsymbol{m}} \times \partial_y \hat{\boldsymbol{m}}) \, dx dy$$

$$= \frac{1}{4\pi} \int_\infty^0 d\rho \int_0^{2\pi} d\phi \, \frac{d\Theta(\rho)}{d\rho} \cdot \frac{d\Phi(\phi)}{d\phi} \cdot \sin \Theta(\rho). \tag{1.3}$$

The proof of this topological invariant is nontrivial and beyond the scope of this work; see [23]. $N_{\mathrm{sk}} = 1$ is a skyrmion (Figure 1.3, Figure 1.4), $N_{\mathrm{sk}} = -1$ is an anti-skyrmion (Figure 1.5), and $N_{\mathrm{sk}} = 0$ is a bubble with trivial topology (Figure 1.6).

The texture's rotation sense is generally characterized by the chirality α. Four specific values indicate Bloch and Néel textures: $\alpha = \frac{\pi}{2}$ is a clockwise Bloch skyrmion, $\alpha = \frac{3\pi}{2}$ is an anti-clockwise Bloch skyrmion (as in Figure 1.3); and $\alpha = 0$ is an inward-pointing Néel skyrmion, $\pm\pi$ is an outward-pointing Néel skyrmion (as in Figure 1.4). This definition of α follows the convention of Chen *et al*[49], namely, the angle between the magnetization in the domain wall and the direction of increasing M_z.

(a) Bloch domain   **(b)** Néel domain
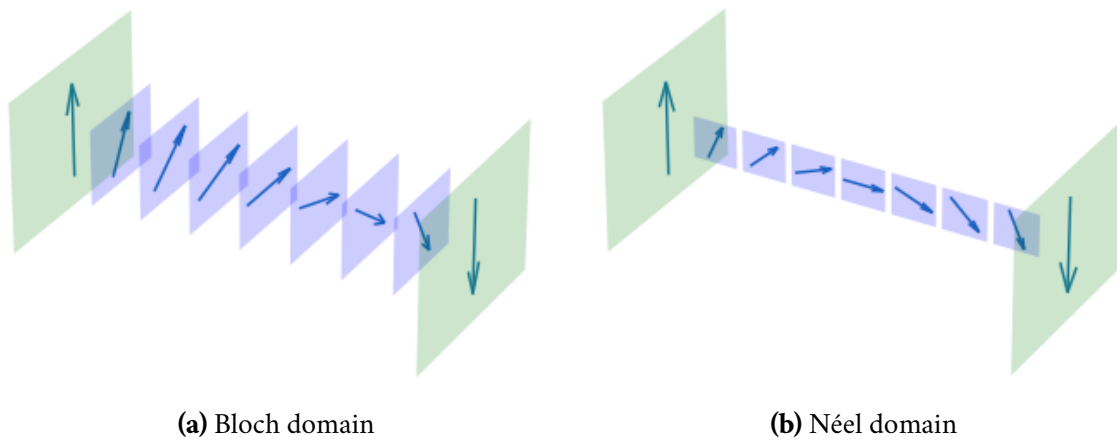
Figure 1.2. Through magnetic domain walls, the magnetization direction changes; in the images above, it transitions from up on the left to down on the right. The two simplest transition mechanisms are in a plane parallel to the ends or orthogonal to those planes. (a) For Bloch walls, the magnetization direction changes parallel to the plane of the domain wall. (b) For Néel walls, the magnetization direction is perpendicular to the plane of the domain wall.
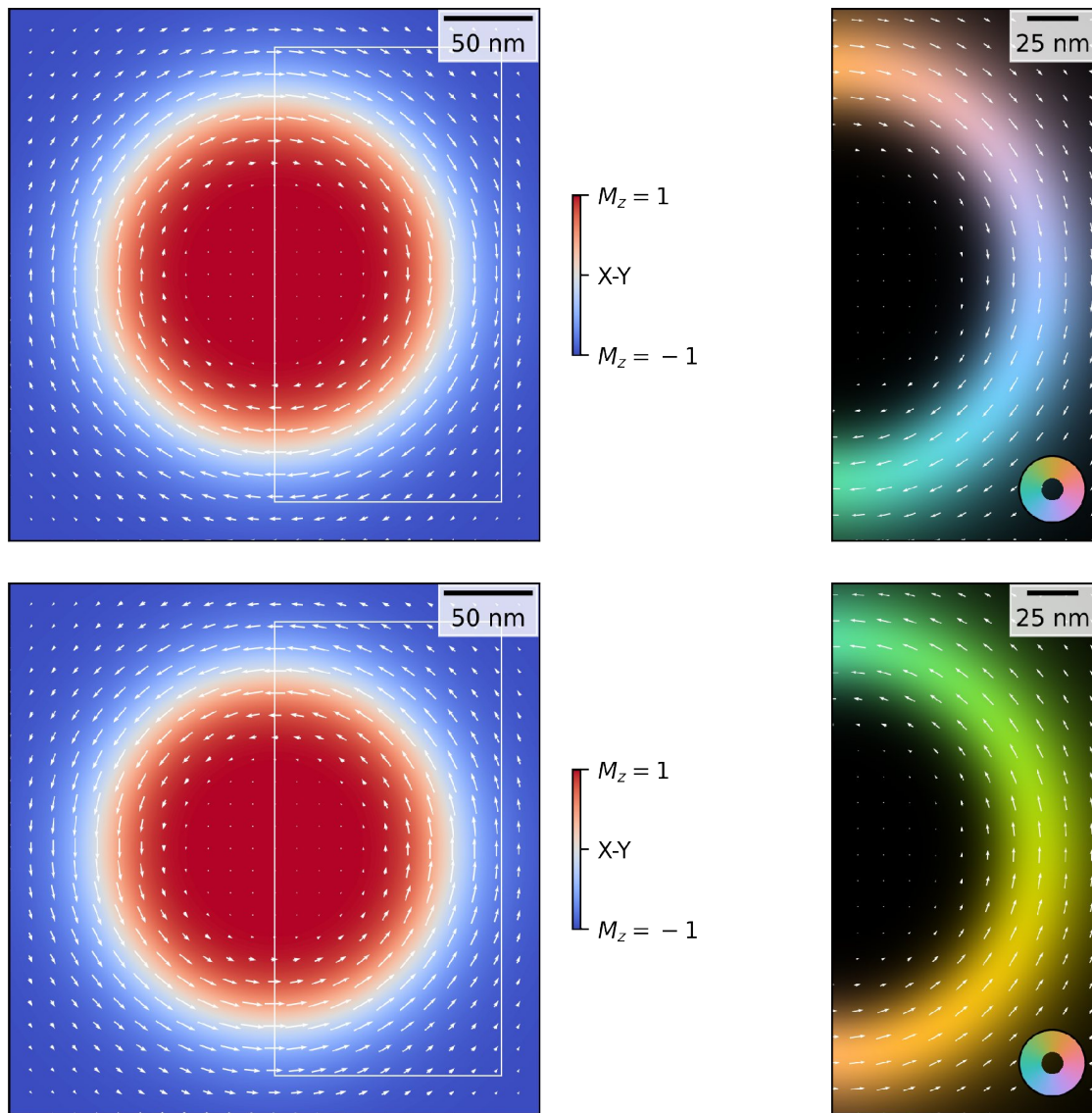
Figure 1.3. Schematics of Bloch skyrmions with $N_{\text{sk}} = 1$. The top images have $\alpha = -\frac{\pi}{2}$ and are clockwise/right-rotating; the bottom have $\alpha = \frac{\pi}{2}$ and are anti-clockwise/left-rotating. The inset at the bottom right of the zoomed images shows the direction of the in-plane magnetization.
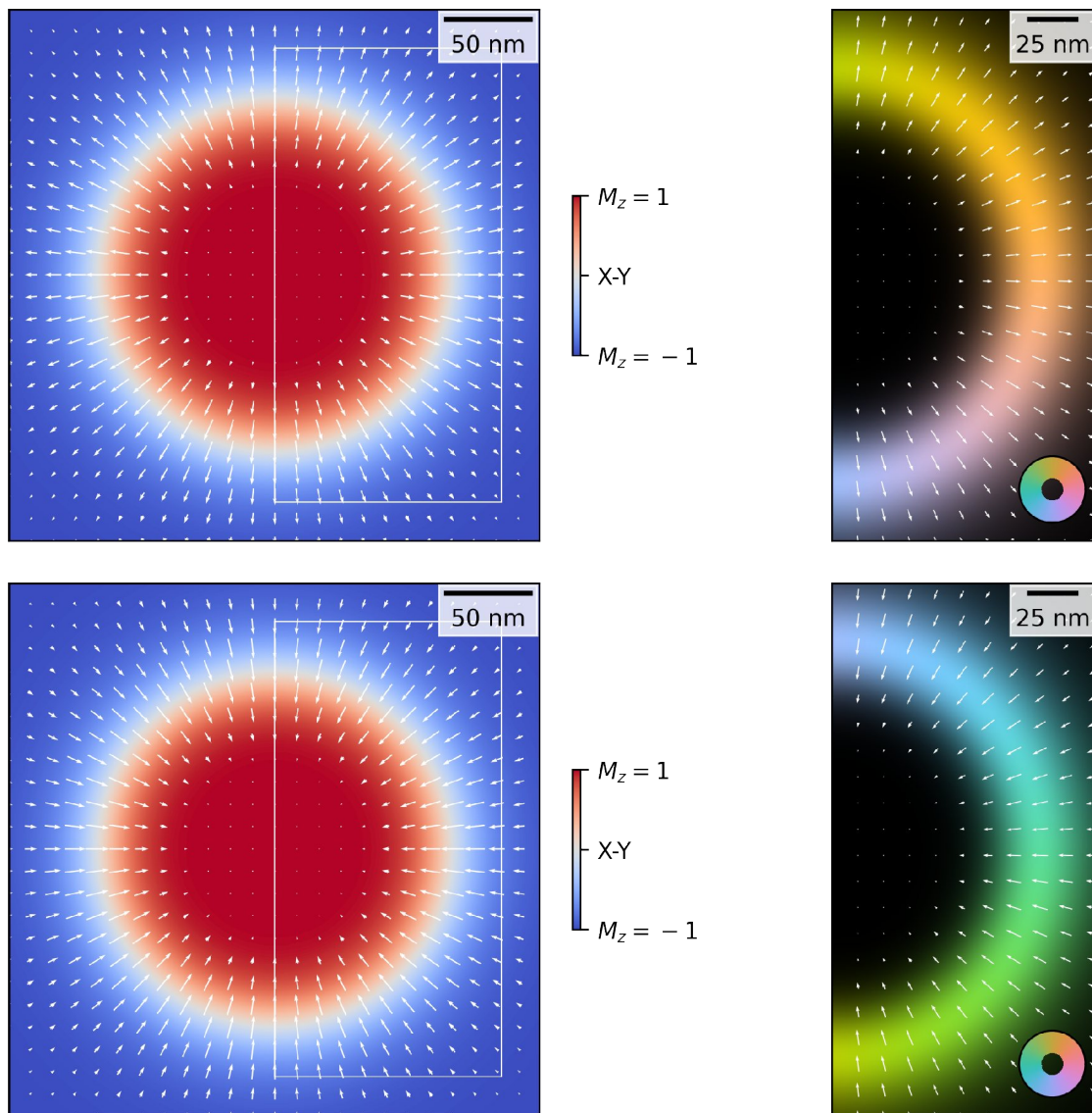
Figure 1.4. Schematics of Néel skyrmions with $N_{\text{sk}} = 1$. The top images have $\alpha = \pi$ with field lines pointing radially outward; the bottom have $\alpha = 0$ with lines pointing inward.
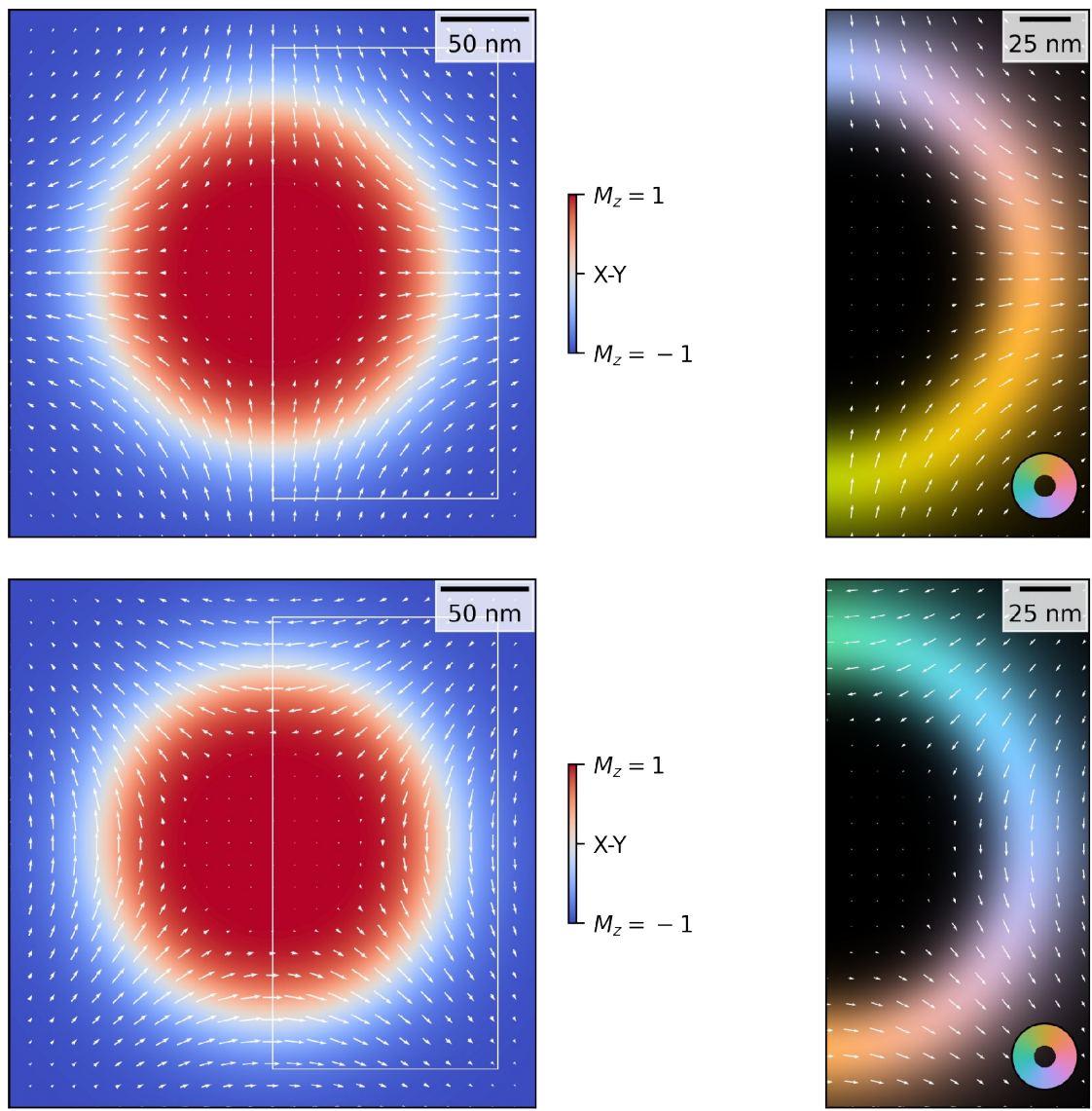
Figure 1.5. Schematics of antiskyrmions with $N_{\mathrm{sk}} = -1$. The top images have $\alpha = 0$, while the bottom have $\alpha = \frac{\pi}{2}$, effectively the first images rotated 90°.
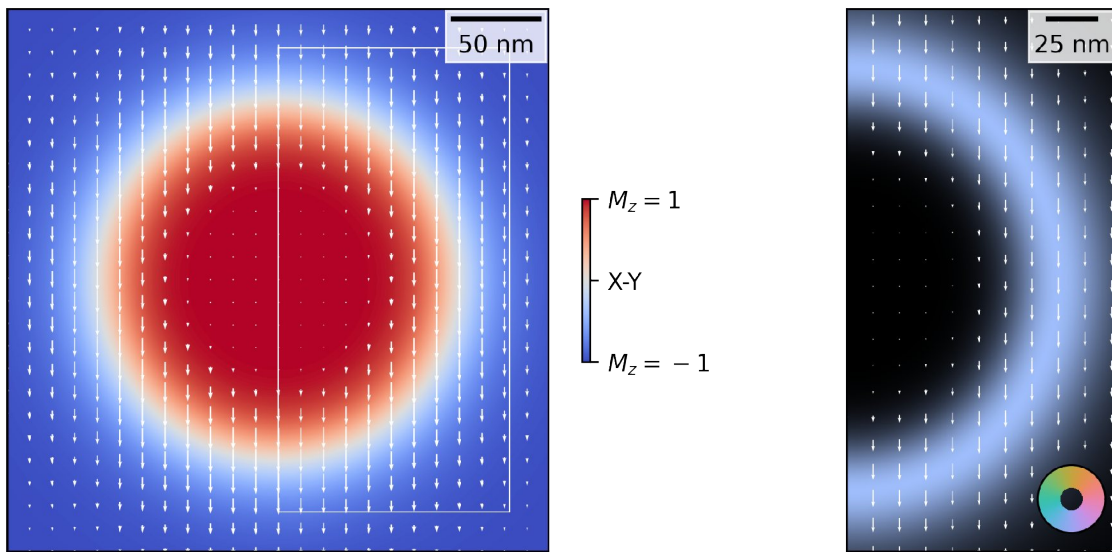
Figure 1.6. Schematics of a bubble with $N_{\mathrm{sk}} = 0$. Field lines simply flow around the bubble, entering and exiting in the same direction.

Stabilization Mechanisms

There are a number of mechanisms responsible for magnetic skyrmion formation[48] that are discussed here.

Dzyaloshinskii-Moriya interaction (DMI)

Spin-canting in non-centrosymmetric magnetic crystals, called DMI after its discoverers, was the first mechanism suggested for magnetic skyrmion creation[50]. Moriya predicted that neighboring electrons in these crystals would have as much as 90% of their spins leaned into the a axis of the crystals with only ~10% pointed into in the c axis. In 2007 Bode *et al* found that DMI was responsible for "directional non-collinear magnetic structure[s]" at surfaces[51]. The great majority of magnetic skyrmion research since has focused on DMI-stabilized textures[52].

DMI has been found to stabilize skyrmions in a number of materials, including MnSi[32, 34, 53–55] and FeGe[56–61], described by the DMI Hamiltonian,

$$H_{\mathrm{DMI}} = \boldsymbol{D} \cdot \sum_{\langle i,j \rangle} \boldsymbol{S_i} \times \boldsymbol{S_j}, \tag{1.4}$$

where $\boldsymbol{D}$ is the material-dependent interaction vector and $\boldsymbol{S_i}$ and $\boldsymbol{S_j}$ are nearest neighbor spins. The net effect is to cause nearest neighbor spins to cant, tilting relative to each other[62]. It is significant to note that the energy of this effect is generally on the order of 1×10^{-2} to 1×10^{-5} that of the energy of the Heisenberg Hamiltonian,

$$H_{\mathrm{H}} = -J \sum_{\langle i,j \rangle} \hat{\boldsymbol{S}}_i \cdot \hat{\boldsymbol{S}}_j, \tag{1.5}$$

where J is the positive-valued coupling constant and the hats indicate unit length spins, which tends to align the spins to minimize energy.

Frustrated exchange interactions

Magnetic frustration in a triangular lattice has been studied theoretically using a three term Heisenberg Hamiltonian,

$$H_{\mathrm{F}} = -J_1 \sum_{\langle i,j \rangle} \hat{\boldsymbol{S}}_{\boldsymbol{i}} \cdot \hat{\boldsymbol{S}}_{\boldsymbol{j}} - J_{2,3} \sum_{\langle\langle i,j \rangle\rangle} \hat{\boldsymbol{S}}_{\boldsymbol{i}} \cdot \hat{\boldsymbol{S}}_{\boldsymbol{j}} - H \sum_i S_{i,z}, \qquad (1.6)$$

where the middle term is for second nearest neighbors, the third term describes spin interactions with a magnetic field H in the z direction, and again all J values are positive. This has been shown to stabilize both skyrmions and antiskymions in a superposition of three wave vectors called the triple-q state[63–65].

Four-spin exchange interaction

A monolayer hexagonal Fe lattice on an Ir substrate has been shown via spin-polarized scanning tunneling microscopy (SP-STM) to stabilize skyrmions due to electrons shared across 4 adjacent lattice sites[66–68].

Long range dipolar interaction

Dipolar exchange in magnetic thin-films prefers an in-plane magnetization. When one film is overlaid with a dissimilar film, strains within the layers as the lattices struggle to align lead to an effect conceptually the same as DMI, called interfacial DMI. When multiple layers are stacked on top of each other, and even more so when heavy metal layers such as Pt or Ir are interspersed[69–71], the effects of the spin canting add up and create perpendicular magnetic anistropy (PMA)[72]. PMA prefers out-of-plane magnetization. The short range dipolar exchange energy competes with the PMA[73], stabilizing skyrmions in defined parameter space[74, 75].

The dipolar Hamiltonian takes the form

$$H_{\mathrm{dip}} = \sum_{i \neq j} \frac{(g\mu_{\mathrm{B}})^2}{r_{ij}^3} \left[3 \left(\hat{\boldsymbol{r}}_{ij} \cdot \boldsymbol{S_i} \right) \left(\hat{\boldsymbol{r}}_{ij} \cdot \boldsymbol{S_j} \right) - \boldsymbol{S_i} \cdot \boldsymbol{S_j} \right], \qquad (1.7)$$

where g is the dimensionless magnetic moment, μ_{B} is the Bohr magneton, and $\boldsymbol{r}$ is the separation between spins S_i and S_j.

Characterizing heterostructures of this sort is the primary subject of this work.

Recently the emergence of skyrmions and other magnetic domains in Fe/Gd multilayer thin films has been studied extensively[76–80], as these materials show great promise for spintronic applications[81–83].

Engineering Skyrmions

Our collaborators at the Center for Memory and Recording Research (CMRR) at UC San Diego, Eric Fullerton and Sergio Montoya, have fabricated Fe/Gd multi-layer thin films using sputter deposition on Si[84]. Samples of these films were studied by two previous members of the McMorran group.

Jordan Chess[85] produced a number of software tools for modeling skyrmion structures (one of which was used to produce the simulated images above). He also used Lorentz-TEM (LTEM) and scanning electron microscopy with polarization analysis (SEMPA) to examine labyrinth domains in the supplied samples. LTEM and micromagnetic simulations were used to examine skyrmions in the samples (no skyrmions were found in the samples imaged by SEMPA). Three items partic-ularly relevant to this work from his research[76]: a preference (95%) for a single chirality in a sample which should not be significantly influenced by DMI[49, 86]; a bimodal chirality distribution fairly sharply peaked at $\alpha = \frac{\pi}{2}$ and $\frac{3\pi}{2}$; and micro-magnetic simulations predicting Néel closure caps at the top layer of the skyrmion.

Alice Greenberg[87] used LTEM and scanning transmission electron microscopy holograph (STEMH) to examine a Landau domain in a permalloy square and skyrmions in an Fe/Gd sample. Results of relevance from her work include: micromagnetic simulations suggesting the skyrmions in Fe/Gd might, in fact, be hopfions, a 3 dimensional object with a more complex topology than the 2 dimensional skyrmions typically described; and discussion about the shortcomings of using LTEM to attempt to image these objects.

Nanomagnetic Microscopy Techniques

Skyrmions can be characterized in many ways, including direct imaging. Several magnetic microscopy techniques exist.

Much of the skyrmion characterization work to date has used 2 dimensional imaging technologies to capture magnetization information, such as TEM[78, 88–90] and X-ray scattering[91–94].

TEM produces images by passing electrons (300 keV is typical) through the bulk of a sample; see schematic in Figure 1.7. Operated in Lorentz mode, in which the objective lens is turned off, eliminating any remanent fields at the sample, the electrons in the beam interact with the components of magnetic field perpendicular to the beam's path present in the sample via the Lorentz force, $\boldsymbol{F_L} = -e(\boldsymbol{v} \times \boldsymbol{B})$, acting on the electrons' paths. The resulting deflection is revealed when the TEM is adjusted to image the electron beam in a plane beyond the sample. One significant limitation of this approach is that only the components of the magnetic field perpendicular to the beam cause electron deflection, only revealing Bloch components and effectively rendering Néel components invisible. The net image shows the integrated magnetic field. As such, in cases where there is a mirror symmetry between
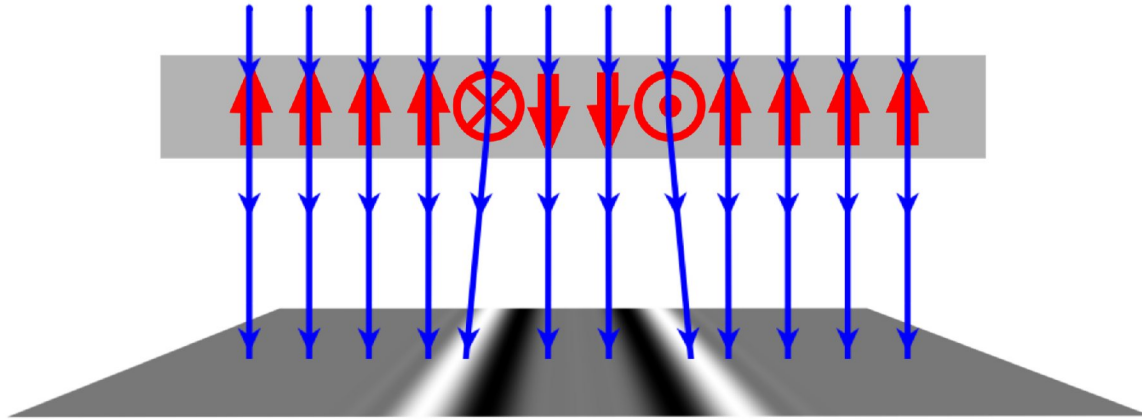
Figure 1.7. Schematic of LTEM contrast formation. Electrons (blue lines) passing through the sample plane (gray rectangle) are deflected by in-plane magnetization (circled X and dot) by the Lorentz force, creating light and dark regions at the bottom. Perpendicular magnetization (red up and down arrows) has no effect on the electron beam path. Figure courtesy of Jordan Chess.

the top and bottom of a sample, any Lorentz force influence on the beam at the top of the sample will be undone by the influence at the bottom.

Lorentz TEM provides 2 dimensional projection images of the magnetic field, but fully understanding the nature of the magnetization, particularly at domain walls, requires a full 3 dimensional analysis. There are a handful of microscopy technologies used for capturing 3 dimensional magnetization data; several are described below.

Magneto-optical Kerr Effect Microscopy (MOKE)[95, 96] exploits the fact that light reflected from a surface with magnetization can undergo polarization and intensity changes. These effects can be reversed in software to determine the surface magnetization. Being a light-based technique, spatial resolution of ~200 nm[97] is not quite sufficient for the features examined in this work.

Similar to MOKE, X-ray Magnetic Circular Dichroism in Photoemission Electron Microscopy (XMCD-PEEM)[98, 99] is another light-based approach. In this case, however, X-rays are used as the source, emitting electrons from the sample

being imaged. The resolution is still limited (~50 nm[100]), again limiting the utility of this instrument.

Spin Polarized Low Energy Electron Microscopy (SPLEEM)[101–103] is a rare method that uses very low energy electrons, ~1 eV, to image magnetic surfaces at fairly high resolution (~10 nm). SPLEEM uses a spin-polarized source and relies on the exchange interaction between the incident polarized electrons S and surface polarized electrons M with a strength proportional to $S \cdot M$[104]. This technique typically involves imaging the sample from opposite angles and subtracting the image pair, and as such is generally limited to imaging crystalline structures with strong crystal orientations.

Based on a technique first described by Koike and Hayakawa in 1984[105], Scanning Electron Microscopy with Spin Polarization (SEMPA, also spin SEM)[105–108] modifies a typical SEM for probing with additional components added to analyze the the polarization of secondary Auger electrons. At the University of Oregon we have a truly unique instrument, which we simply refer to as SEMPA, of this type. The microscope was built at NIST[109] in the early 2000's and donated to the University when the program there was retired.

In this work, skyrmion data from SEMPA and LTEM are analyzed in an effort to answer the question: what is the 3 dimensional structure of these skyrmions? The results strongly suggest the reality is more complicated than a uniform cylindrical domain wall through the bulk.

Dissertation Outline

This dissertation covers the revival of a unique magnetic characterization instrument, the SEMPA, a new software framework for processing SEMPA's outputs, and the application of these tools to the analysis of magnetic textures in Fe/Gd multilayer heterostructures.

Chapter I lays out the motivation for this work, along with the history and theoretical underpinnings of the research. Chapter II gives an overview of the SEMPA, including a brief description of how it functions and the myriad capabilities it offers. Chapter III covers the methodology used for analysis, including a walk through of the main software steps. Chapter IV contains the results of using SEMPA to characterize an Fe/Gd multilayer sample fabricated by our collaborators along with discussion of those results. Finally, Chapter V provides a summary of the outcomes with a look to the future of the material as well as the abilities of the SEMPA.

There are two appendices: Appendix A provides a link to the most recent code base for the pyNISTView software, while Appendix B reproduces SEMPA: The Missing Manual, also available as a stand-alone document for users of the SEMPA.

CHAPTER II

SEMPA

Theory of Operation

Spin polarized secondary electrons were first observed experimentally with an SEM in 1984 by Koike and Hayakawa using a cold field emission source and a high energy (100 keV) Mott detector[110]. The same year, Penn and Apell found that the number of spin polarized secondaries emitted is greatest at low energies[111]. Figure 2.1 shows the number and polarity distributions of secondary electrons for typical ferromagnets from 0 eV to 30 eV.

The SEMPA is a heavily modified JEOL JAMP-7830F Auger microprobe with a thermally assisted field emission source. This base platform was chosen because SEMPA, an inherently inefficient technique, requires ultra high vacuum (UHV) and clean surfaces. Auger analysis (electron energy spectroscopy for characterizing material composition) has the same requirements, and the JEOL is capable of a UHV environment of 1×10^{-8} Pa. Two Mott detectors are attached to a purpose-built column to perform polarization analysis.

The primary electron beam incident on the sample will penetrate to some depth (Figure 2.2(a)), dependent on beam energy, sample material, and angle of incidence (Figure 2.2(b)). The incoming beam has sufficient energy to ionize atoms in the sample, scattering a number of electrons (called secondary electrons) and x-rays from within a tear-drop shaped region called the interaction volume. Lower energy Auger electrons are collected and analyzed.
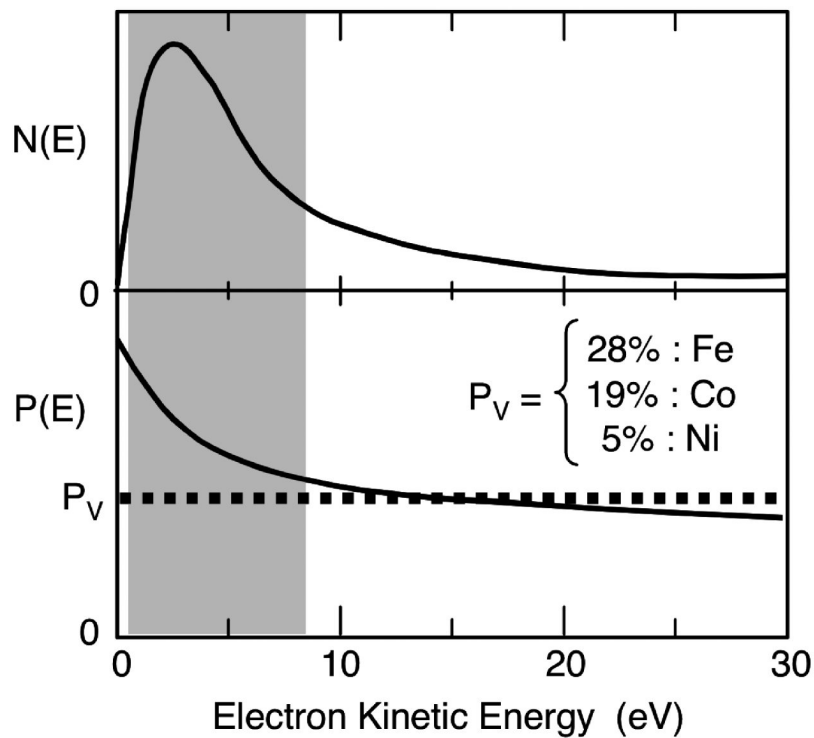
Figure 2.1. Typical energy distributions of the number (N) and polarization
(P) of secondary electrons measured for ferromagnetic materials.
The polarization distribution is enhanced at low energies due to
spin-dependent filtering of low energy secondary electrons[112].
SEMPA uses an extraction lens to capture low energy (~10 eV) Auger
electrons whose polarization is recorded by a Mott detector. Figure
reproduced with permission from "Scanning electron microscopy
with polarization analysis (SEMPA) and its applications" by John
Unguris in Experimental Methods in the Physical Sciences. Vol. 36.
Elsevier, 2001, pp. 167–XVI.
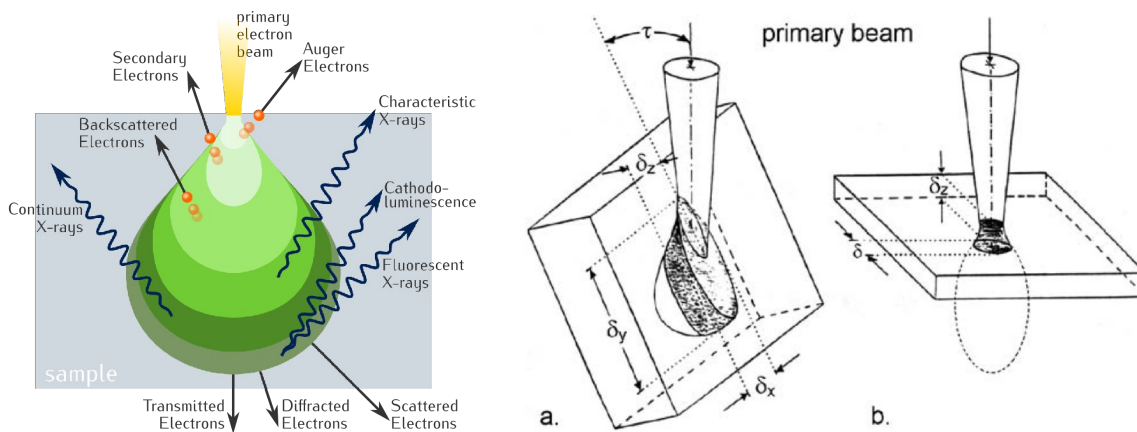
(a) Normal interaction volume. The incoming primary electron beam (yellow, top) penetrates the sample to an energy and material dependent depth, causing a number of reactions. Figure reproduced from "Electron–matter interaction volume and types of signal generated" at Wikimedia Commons (CC BY-SA).

(b) Effect of tilting the sample relative to the electron beam on the interaction volume. Figure reproduced with permission from "Spatial Resolution in ACOM - What Will Come After EBSD" by R. Schwarzer in Microscopy Today 16(1):34-37 (2008).

Figure 2.2. Electron beam interaction volumes

The Auger-Meitner Effect

The Auger-Meitner effect[113] occurs when an incoming electron of sufficient energy scatters an electron from an inner shell of an atom, creating a hole. This hole can be filled by an electron from a higher orbital. If the binding energy of the lower orbit is considerably less than the transition energy of the lowered electron, the excess energy can cause another higher shell electron to be ejected. These energies are relatively low, on the order of 50 eV to 3,000 eV[114], leading to a short mean free path when the process occurs within a material. The electrons that break free from the sample are thus most likely from the top several layers (on the order of 1 nm[109]) of the sample. Tilting the sample (Figure 2.2(b)) puts more of the interaction volume near the surface, which is preferable for Auger analysis, where the goal is to characterize the very top layer of the sample.

Mott Scattering

Similar to Rutherford scattering except using electrons instead of alpha parti-cles, Mott scattering occurs when electrons penetrate the nucleus of a high z atom (typically gold since it does not oxidize and can be sputtered into a thin film as is the case with SEMPA) and inelastically scatter off the Coulomb potential of the nu-cleus. Spin-orbit coupling between the electrons and the nucleus splits the trajecto-ries of the electrons depending on their spin state. The cross-section for scattering takes the form[115]

$$\sigma(\Theta) = I(\Theta)[1 + S(\Theta)\boldsymbol{P} \cdot \boldsymbol{n}], \tag{2.1}$$

where Θ is the angular distribution of the scattering profile, S is the Sherman func-tion, a characteristic of the detector design, $\boldsymbol{P}$ is the beam polarization, and $\boldsymbol{n}$ is normal to the detector plane.

The Microscope

A schematic model of the SEMPA is shown in Figure 2.3. Probe electrons inci-dent on a tilted magnetic sample eject secondary electrons from the top nanometer or so of the surface[116]. These electrons scatter from the sample in all directions.

There are a number of additional features that have been added to the micro-scope, described both below and in Appendix B, making it a robust and diverse tool for analyzing magnetic textures.

Plasma Gun

A tectra GenV plasma source sits atop the sample exchange chamber. Config-ured to use Ar gas (though at NIST it was connected to a manifold allowing other
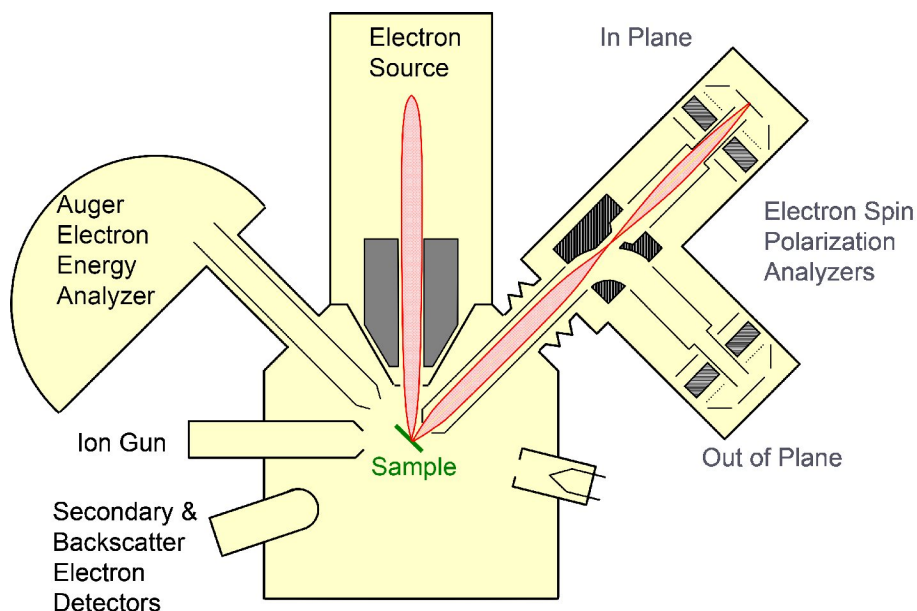
Figure 2.3. Schematic of SEMPA. After milling the Sample surface (tilted green line, bottom center) clean with the Ion Gun (bottom left), spin–polarized secondaries (pink shape traveling up and to the right from the sample) scattered by the incident electron beam (pink shape traveling down from the Electron Source at the top) are guided into the SEMPA column (L-shaped part on the right). These electrons are then Mott scattered by a gold target (top right where the secondary beam ends for In Plane and bottom right in the same area for Out of Plane) before being counted by a cloverleaf–shaped array of sensors (gray blocks above and below Electron Spin Polarization Analyzers). Depending on the configuration, either In Plane ($x - y$, top right) or Out of Plane with redundancy ($x - z$, bottom left) spins are examined. Figure reproduced with permission from "Scanning electron microscopy with polarization analysis (SEMPA) and its applications" by John Unguris in Experimental Methods in the Physical Sciences. Vol. 36. Elsevier, 2001, pp. 167–XVI.

gases to be used), it can gently mill samples with energies in the range 50 eV to 2,000 eV. This can be particularly useful for thin and/or delicate samples.

Electromagnet

A custom twin coil electromagnet has been added to the rear of the instrument, next to the parking chamber. This permits subjecting samples to magnetic flux up to 1 T at normal incidence and a range of tilts. The polarity of the field can be reversed by exchanging current supply leads.

Molecular Beam Epitaxy (MBE)

The main analyzing chamber is equipped with MBE deposition equipment for sputtering Fe, Co, or Ni onto samples. Sputter rates for Fe are $0.19 \, \text{nm} \, \text{min}^{-1}$ to $0.27 \, \text{nm} \, \text{min}^{-1}$. MBE can be used to enhance the magnetic signal of weak samples by applying a thin film of a ferromagnetic material to the surface.

Multi-pin Sample Holder

The stage has been configured with a 7 pin feed-through connector, providing a facility for a number of active experiments. A simple example of this is the Faraday cup sample holder that has an electrically isolated chamber wired to one pin while the top isolated aperture plate is wired to another. This allows precise measurements of beam width and current at the sample plane.

Manipulator Arm

A Kleindiek MM3A micromanipulator arm is positioned to reach the sample holder in the main analyzing chamber. Samples can be moved around *in situ* using a PlayStation® controller on the main console.

A comprehensive manual covering all of the standard aspects of the SEMPA can be found in Appendix B.

SEMPA Column

A schematic of the SEMPA optics is shown in Figure 2.4 and a cutaway of the assembly in Figure 2.5.

The tip of the SEMPA column in the main chamber is the extraction lens, placed about 1 cm from the sample and DC biased to optimize collection of the most spin–polarized Auger electrons at around 10 eV. The input lens placement also helps to capture the electrons before any external fields can significantly affect their spin.

Once through the extraction lens, a series of Einzel lenses, apertures, and deflectors focus, align, and zoom the beam up and right to the dark block (the quarter sphere) in the center of the column. A unique feature of this microscope is the inclusion of a voltage-adjustable quarter sphere electrostatic mirror in the center of the SEMPA column that can deflect the electron beam 90° without affecting spin polarization, thus permitting mapping the $x - y$ and $x - z$ magnetization vector components and enabling capture of all three vector components of surface magnetization. This directs the beam to one of two detectors: it either allows the electrons to pass to the Straight Through (ST) detector (at the top right of Figure 2.4, labelled "In Plane"), which captures M_x and M_y information, or guides electrons via the electrostatic mirror to the right-angle (RA) detector (at the bottom right of Figure 2.4, labelled "Out of Plane"), which captures M_x and M_z information.
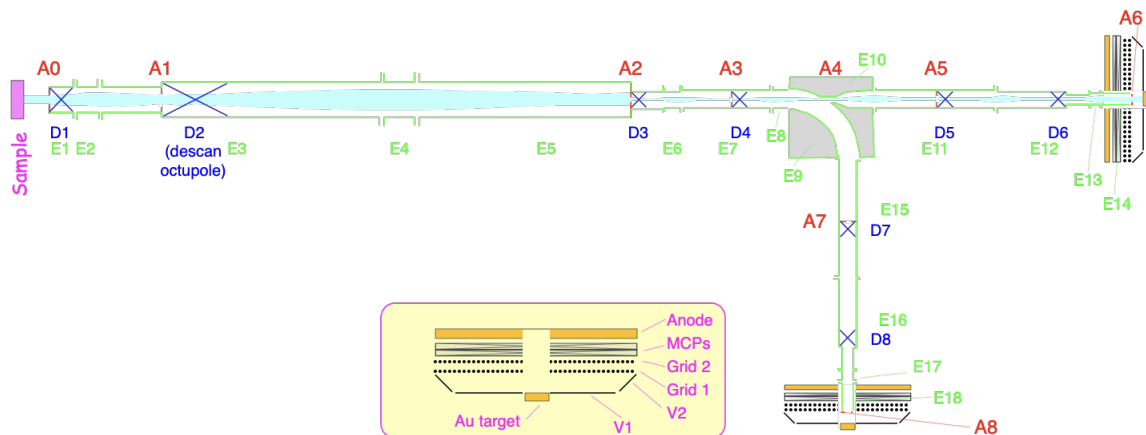
Figure 2.4. Schematic of the SEMPA optics. The electron beam is focused to a minimum waist at aperture A1 by lenses E1, E2, and E3 and centered by deflector D1. Lenses E4, E5, and E6, along with deflector D2, handle similar duty for aperture A2, effectively the beam defining aperture. Lenses E5, E6, and E7 focus the beam at aperture A3, providing the object for the quarter sphere. When E8, E9, and E10 are at the same 1,500 V potential, the beam passes straight through; reducing the voltage at E8 and E9 to 340 V defects the beam 90°. Lenses E11, E12, and E13 (or E15, E16, and E17 for right angle operation) zoom the beam, with deflectors D5 and D6 (D7 and D8 for right angle) control angle and position at the Au foil target, extreme right[106]. After scattering off the target, V1 and V2 are biased to guide the beam into Grid 1 and Grid 2 which accelerate the beam into the multichannel plates, MCPs. Electrons striking the MCPs cause a cascade of secondaries, maximizing the signal into the anodes. Image courtesy of NIST.
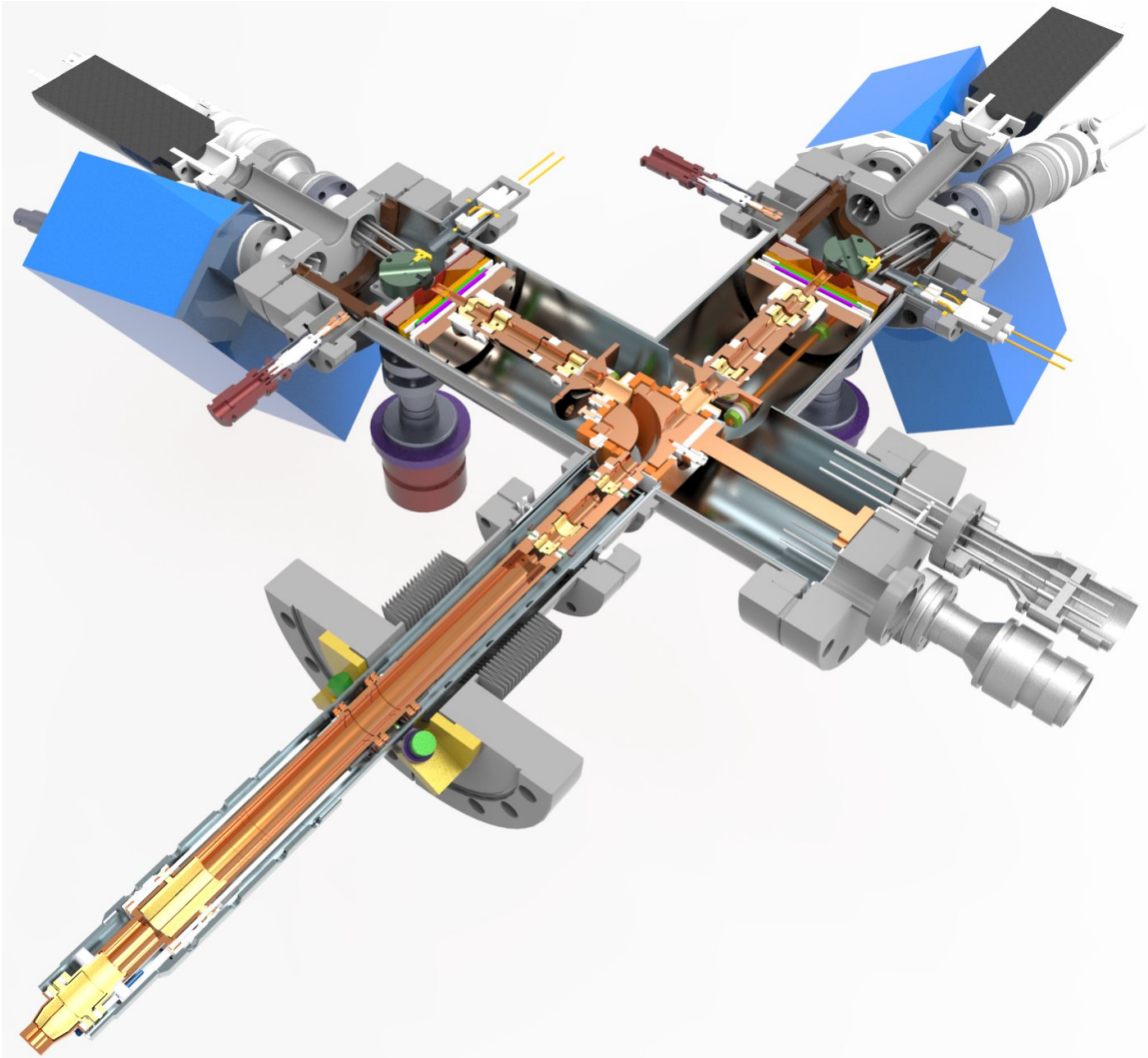
Figure 2.5. Cutaway view of the SEMPA. The input optic is bottom left; the quarter sphere is at the cross; the ST components top right and the RA components top left. The copper parts are predominantly the Einzel lenses. The gray rectangles top left and right are the E-T detectors and the blue boxes are the signal processors for the Mott detectors. The gold target positioning knobs protrude down from the top halves of the column; they are both set to 90°, the position that would be used for cleaning the gold targets. Image courtesy of NIST.

At this point the electrons Mott scatter off the Au foil at the end of the column. They are subsequently decelerated to a landing energy, 150 eV, determined during design that maximizes spin-dependent backscattering.

Each of the 4-channel Mott detectors in the SEMPA (schematic shown in Figure 2.6) resolve up, down, left, and right spin-polarizations, with net polarization

$$P = \frac{1}{S} \frac{N_+ - N_-}{N_+ + N_-}, \tag{2.2}$$

where N is the number of electrons hitting one of the channels (for Figure 2.6, electrons hitting C and D would be N_+ and N_-, respectively, for M_x, while electrons hitting B and A would be N_+ and N_- for M_y) and S is the Sherman function, a system-specific measure of the dependence of the electron scattering to its spin-orbit coupling, calculated for the SEMPA to be 0.5. As magnetization is proportional to spin polarization, data collected from the $x - y$ plane is combined with $x - z$ data in software to reproduce the 3D surface magnetization.

An example of the output for M_x and M_y observed on an Fe whisker is shown in Figure 2.7. A single SEMPA scan provides two of the vector components of surface magnetization as well as a normal SEM image. It is highly surface-sensitive, providing a direct measurement of the spin polarization of the top few layers of the material imaged down to a spatial resolution of ~10 nm. One limitation, due to the low energy Auger electrons that are ultimately analyzed, is that images must be taken at remanence.
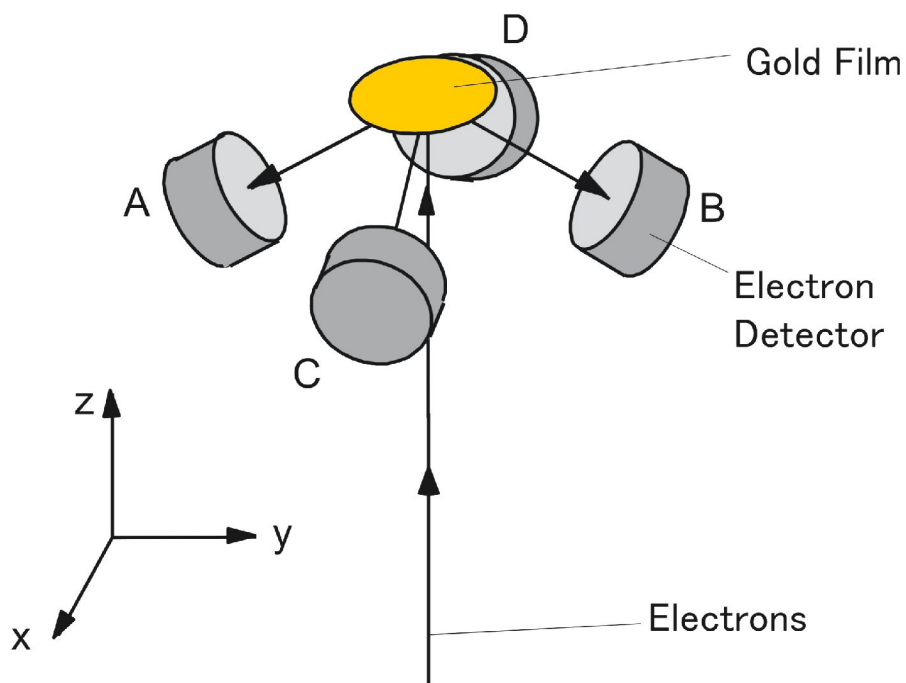
Figure 2.6. Schematic of the Mott detector. As oriented, channeltrons C and D will collect positive and negative x polarizations, while B and A will collect positive and negative y polarizations. There are 2 of these on the instrument: one for straight through operation capturing x and y as shown, the other for right angle operation capturing x and z (with the axes shown rotated 90° about x). Figure reproduced with permission from "Scanning electron microscopy with polarization analysis (SEMPA) and its applications" by John Unguris in Experimental Methods in the Physical Sciences. Vol. 36. Elsevier, 2001, pp. 167–XVI.
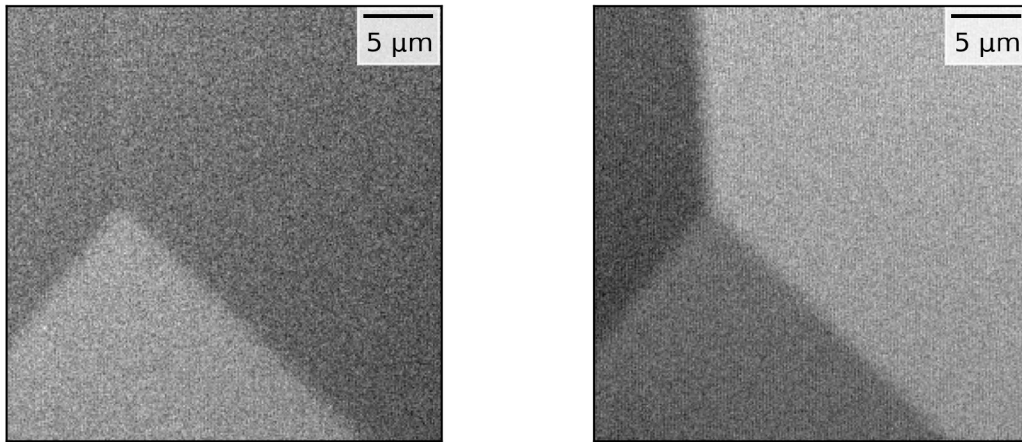
(a) M_x **(b)** M_y

Figure 2.7. Magnetization of an Fe whisker. (a) Magnetization in the x direction: white is right, black is left. (b) Magnetization in the y direction: white is up, black is down. Anti-clockwise from the top left, this shows 3 domains: down, right, up.

CHAPTER III

METHODOLOGY

Image capture on the SEMPA involves 4 steps: sample preparation, SEMPA alignment, SEMPA capture, and data processing.

Sample Preparation

Several $Fe_{0.34}/Gd_{0.40}$ x 120 layers samples (subscripts representing approximate thickness in nm) were created by our collaborators at CMRR; see Figure 3.1. Each sample consists of multiple thin layers deposited on a silicon substrate capped by a thin, nonmagnetic metal layer to prevent oxidation of the structure. The films support a large variety of magnetic domain configurations[85, 87]. To view skyrmions, the films are magnetically prepared using the following recipe.

Sample preparation after receipt begins by nucleating skyrmions. This is done by first tilting a sample to 45° and subjecting it to a 400 mT magnetic flux density, saturating the sample's magnetism. This can be done *in situ* in either the TEM or the SEMPA, using the objective lens of the TEM in Lorentz mode when possible or with the SEMPA electromagnet for general samples. The field is then brought down to 0 and the sample tilted to 90° relative to the applied field. The field is then increased to 185 mT, creating the skyrmionic domains. The field is again decreased to 0. An interesting and somewhat unusual feature of this sample is that the skyrmions remain at remanence (zero applied magnetic field).

The skyrmion nucleation process above takes the sample from a state of saturation (one large domain covering the sample, all in the direction of the external field) to a stripe state as seen in Figure 3.2. Raising the field back up to ~185 mT
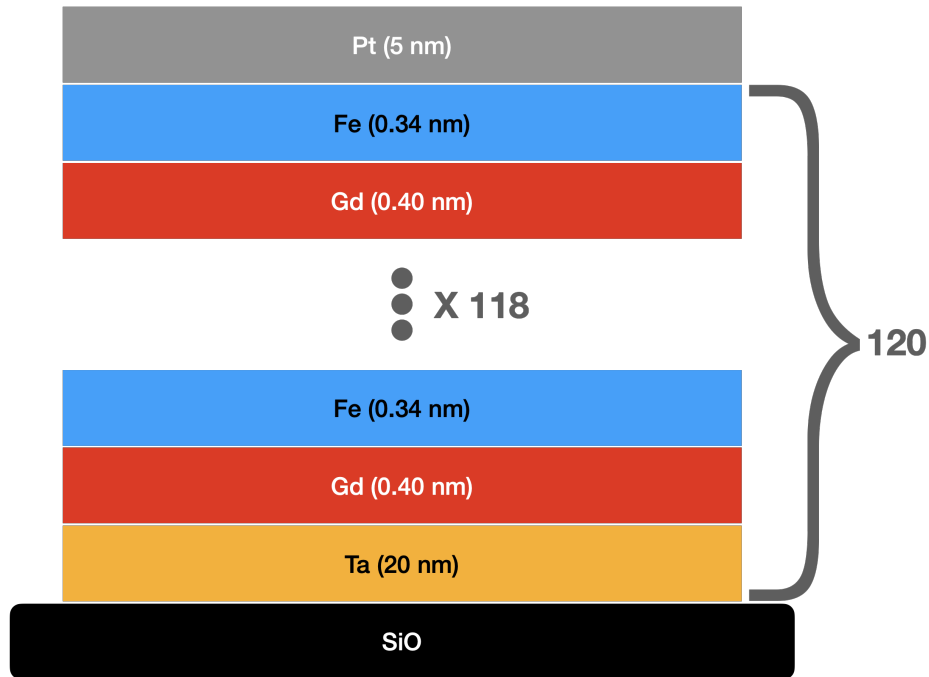
Figure 3.1. Fe/Gd sample layout. A Ta base layer was deposited on a SiO substrate. 120 layers of Fe alternating with Gd were sputtered on top of the base layer and capped off with Pt.

(this value is sensitive and varies somewhat from sample to sample) "pinches off" sections of the stripes, initially into worms, then further into scattered circular domains, then a fairly ordered hexagonal circular domain lattice.

The sample is next loaded into the SEMPA sample exchange chamber and shuttled through the vacuum system into the main analyzing chamber. Standard SEM imaging at 25 kV accelerating voltage is used to find a location of interest on the sample and initial surface composition using Auger analysis.

The Auger scan is run across a defined range of energies selected for the elements in the sample. Each element produces a set of characteristic peaks in the energy spectrum. If the scan result indicates the presence of a contaminant (often O or C) or a capping layer (Pt or Ta for the Fe/Gd samples examined), Ar ion milling is performed to clean the sample surface. To minimize damage to the magnetic
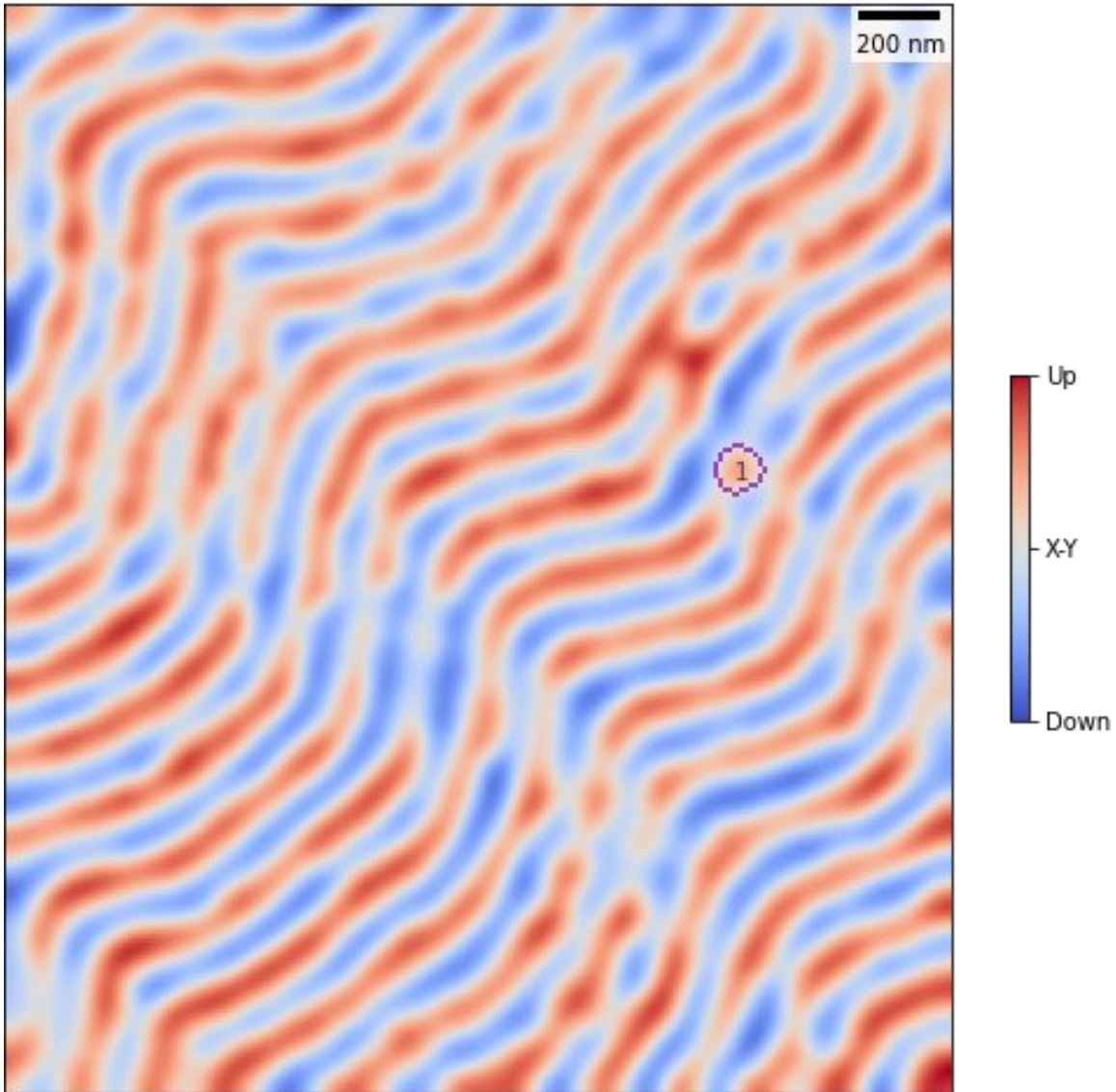
Figure 3.2. SEMPA image of surface magnetization showing stripe domains created by saturating the sample and then reducing the external field to 0. The circled 1 is a round texture identified by the feature finding algorithm described at the end of this chapter.

structures in the Fe/Gd samples, Ar ions are used at a relatively low milling energy of 500 eV. The scan/mill process is repeated until the sample was sufficiently cleaned. Figure 3.3 shows before and after milling one of the Pt capped Fe/Gd samples. Milling through the Pt took ~5 minutes.

The sample is then tilted to 52° in anticipation of SEMPA analysis and eucentric height validated. SEMPA imaging is performed when the main chamber pressure has fallen into the 1×10^{-7} Pa or (preferably) lower range.

SEMPA Alignment

For each sample to be imaged, the next step in the process is aligning the SEMPA optics, depicted schematically in Figure 2.4; a cutaway view of the entire instrument is shown in Figure 2.5.

The input optics (labeled E1 on the schematic) are brought up to 1,500 V to extract and collect secondary electrons while the base voltage for the rest of the electrostatic lenses are increased to 1,700 V (each lens/deflector sits at a value somewhat above or below this base voltage, depending on its purpose). The gold target used for Mott scattering is first removed from the electron path by turning the positioning knob on the SEMPA column to 45°, allowing the electron beam in the column to bypass the target and hit the Everhart-Thornley (E-T) detector at the end of the column. The high voltage power supply in the SEMPA rack is turned on and the output increased to 2,500 V. The E-T selector switch responsible for choosing the detector used for imaging is turned to the Straight Through (ST) setting.

At this point the SEMPA optics are ready for calibration. The SEM image is zoomed out to 50x and contrast increased until the screen begins to show an image. The first three deflectors (D1–D3 on the schematic) are adjusted until the image brightened in the center while zooming in to 10,000x magnification and de-
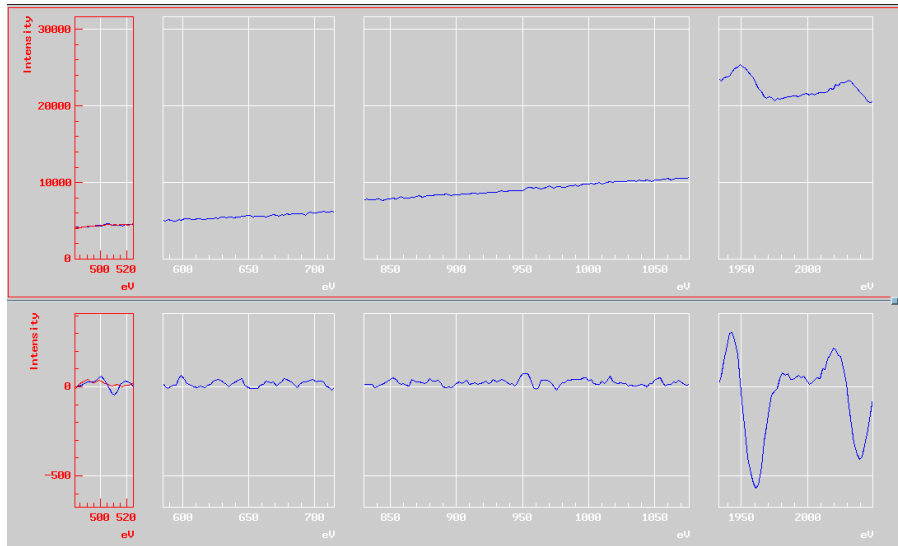
(a) Auger plot of Pt.
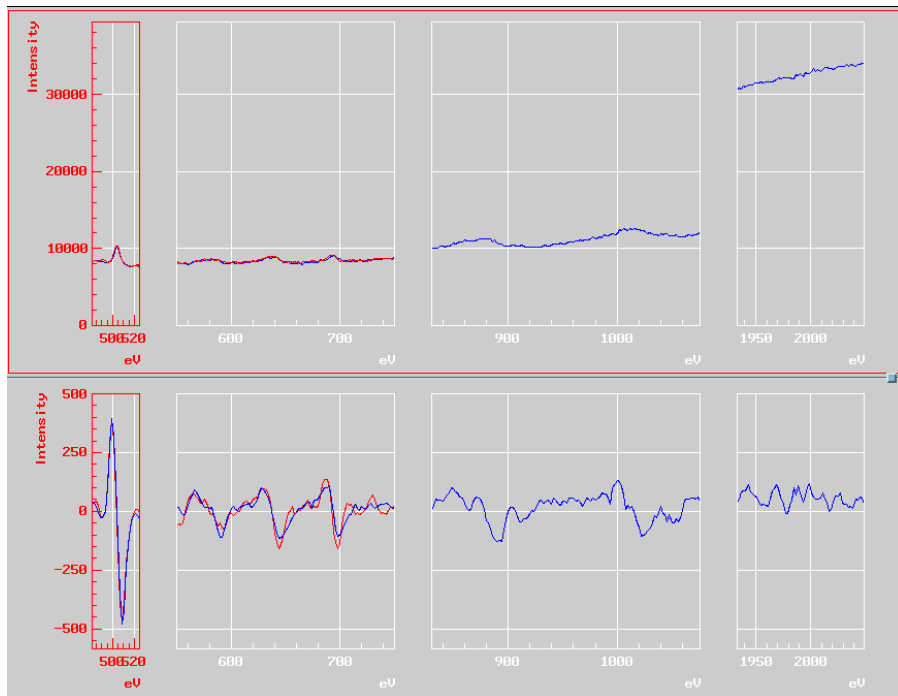
(b) Auger plot of Fe.

Figure 3.3. Auger analysis of a Pt-capped Fe/Gd thin film showing energy ranges for O, Fe, Gd, and Pt from left to right. The top plots are counts at given energies (N(E)); the bottom plots are dN(E). (a) Initially a several nm capping layer was present, evident by the 2 peaks at energies around 1,950 eV and 2,020 eV. The leftmost plot shows no signal for O, while the center two show no signal for Fe or Gd, respectively. (b) After several minutes, the Pt was milled through, evident in the flat rightmost plot, and both Fe and Gd started to show. Interestingly, apparently some O was embedded into the sample during the original deposition.

47

creasing contrast to avoid image saturation. This scans the area from which electrons are extracted. When the SEMPA E-T detector is used to view the image signal, the beam looks like a spotlight that can be moved around. The lenses are adjusted until the brightest area is centered.

With the optics aligned, the ST target positioning knob is turned to 0°, inserting the gold target in line with the electron beam. The preceding steps are repeated for the Right Angle (RA) section.

The high voltage power supply for the E-T is switched off to eliminate interference with the Mott detector.

The power supplies for the blue boxes are turned on, and the multi-channel plate and anode voltages turned on and increased to 1,500 V and 1,600 V, respectively.
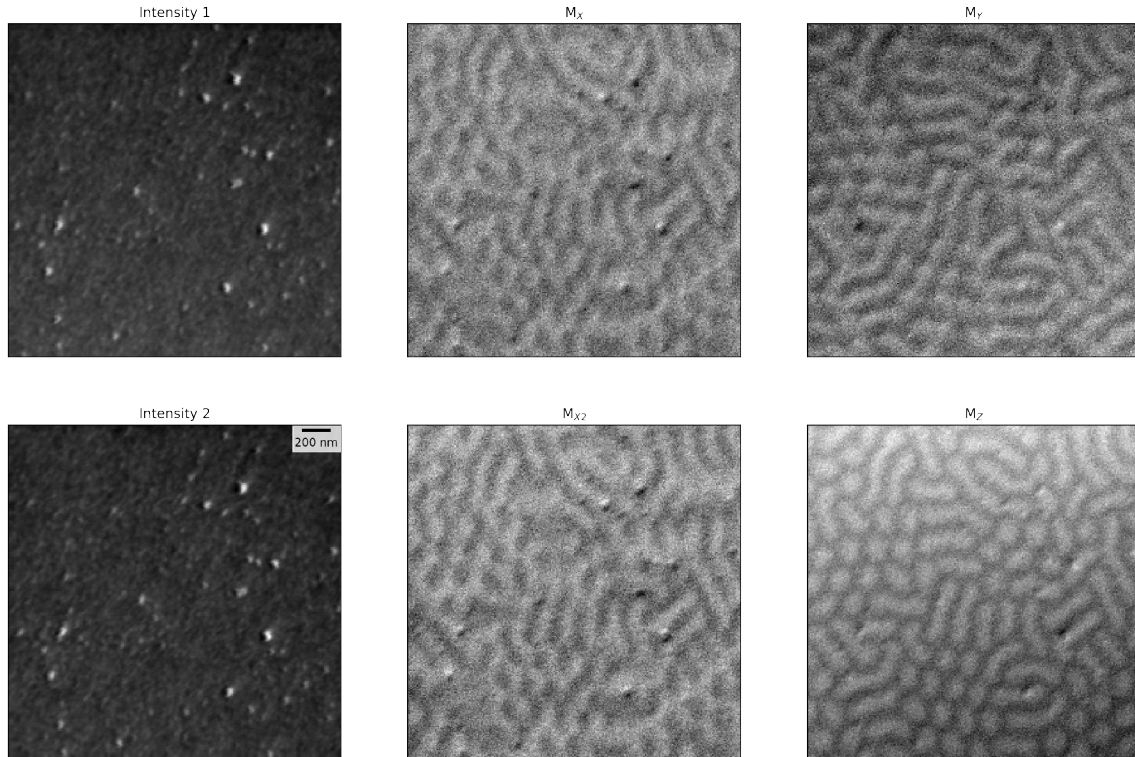
SEMPA Capture

Data collection with the SEMPA begins with configuring the capture software, specifying, among other things, resolution and dwell time. Dwell time, the length of time that the electron beam illuminates a single spot before rastering to the next, can be adjusted depending on the strength of the sample's signal: imaging pure Fe for relatively large (several μm) domains can be accomplished with dwell times on the order of 4 ms, while the much fainter skyrmion signal from Fe/Gd requires 20 ms or more. As such, a single capture can take some time (just under 22 minutes in this case for 256 x 256 images).

The electron beam is blanked and SEMPA zeros measured, during which dark counts are recorded for the Mott detectors. The imaging parameters are set as described above and images captured.

The SEMPA software outputs several NetCDF4 format files for each imaging run. For the ST detector, those include redundant contrast files (with suffixes _–

Figure 3.4. Output of SEMPA image capture. The leftmost images are typical SEM scans. The four images on the right show magnetization, with magnetization strength in that axis from none (black) to maximum (white).

ix.sempa and _iy.sempa and one file each for magnetic contrast in x and Y, namely _mx.sempa and _my.sempa. Imaging parameters and image data are recorded in each file.

The above steps were repeated for the RA detector with outputs _ix2.sempa, _iz.sempa, _mx2.sempa, and _mz.sempa.

A representative output is shown in Figure 3.4.

Data Processing

The software originally written to process the output of SEMPA, written in IDL, did not come with the microscope to the University. The decision was made to develop new software for reading, displaying, and analyzing the data in a more modern, open language. The code described herein was written in python using Jupyter to facilitate easier maintenance and enhancements over time. It was also designed to automate as much of preparing and analyzing the images as possible, minimizing user input.

The `.sempa` file extension output by the SEMPA software is not a standard extension. The string "CDF" was found when examining the binary files from the command line. This led to finding the Network Common Data Form (NetCDF), a format typically used for Geographic Information System (GIS) applications, but appropriate (if not terribly common) for general array-based scientific data. This project took advantage of netCDF software developed by UCAR/Unidata (`http://doi.org/10.5065/D6H70CW6`).

With that determined, preparing the collected data for analysis includes the 5 steps described below.

Importing

For 3D reconstruction, files from both M_x, M_y and M_x, M_z runs are imported. Using the netCDF libraries, image scale and magnification parameters are extracted from the files, along with the image data. The images are stored in 2D arrays.

Registration and scaling

Imperfect alignment and sample drift cause the field of view for consecutively collected ST and RA image captures to be slightly different. As a result, when col-
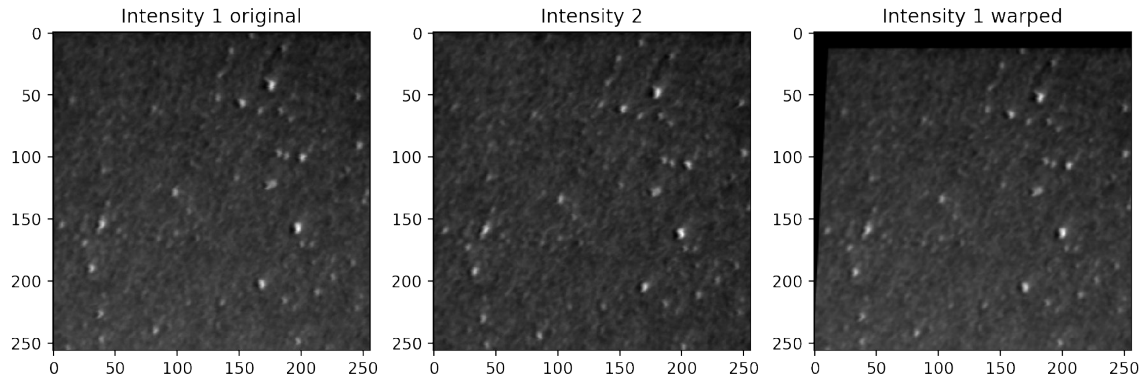
Figure 3.5. Image registration homography applied. Several points from Intensity 1 and Intensity 2 are identified, then the homography to rotate, skew, and scale Intensity 1 is applied to all images. The images are then cropped to remove empty data (shown in the image on the right in black along the left and top sides).

lecting x, y, and z data, requiring two scans, the images must be properly registered so that the vector components at each pixel are correctly aligned. An oriented BRIEF (ORB) keypoint detector[117] in OpenCV is used to attempt to identify key points in the x intensity images from both the ST and RA detectors (_ix and _ix2). The most likely candidate points between the two files are selected.

A homography between the two files is calculated, then used to warp the perspective of the first intensity file. The perspectives for the x and y magnetization images (_mx and _my) are also warped. This operation creates some black pixels around the edges where rotation has occurred, as seen top left in Figure 3.5.

Using a binarized version of the warped image, the extreme outer contours are found in each quadrant. The most distant points in each quadrant (the 4 new corners) are found and used to crop all images.

A light Gaussian filter ($\sigma = 2$) is applied to each image to smooth out some of the noise.

Finally, any data points in the images greater than 3σ from the mean are limited to $\pm 3\sigma$ from the mean to help reduce shot noise and surface defect artifacts. This is an effective value determined by evaluating a number of images.

Removing offsets and rescaling

Though it would seem reasonable that the data in the magnetization images would be in the range -1 to 1 (based on Equation 2.2), the values are typically somewhere between -4 and 6 with a range of around 0.2. The three files do not have the same center point. The differing offsets need to be removed and the data normalized.

All the magnetization image arrays are first individually centered around 0 to provide a seed for fitting. A least squares fit is then applied to square root of all three added in quadrature as magnetization magnitude,

$$|\boldsymbol{M}| = \sqrt{M_x^2 + M_y^2 + M_z^2},$$ (3.1)

is constant in a given material. The values in each array are then normalized with respect to each other, such that at all points $\boldsymbol{M}^2 = 1$.
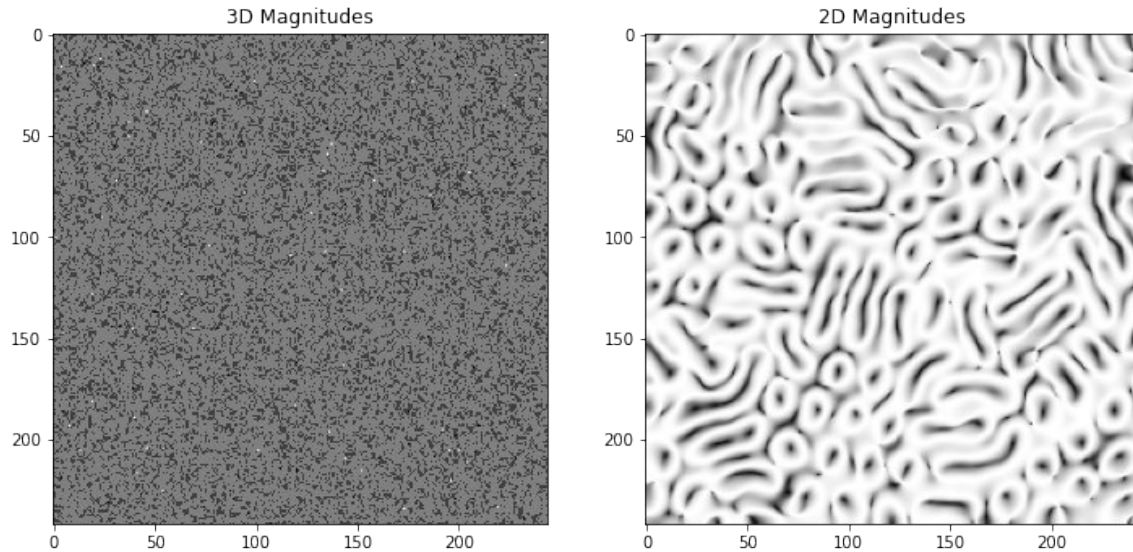
Calculating angles

With the image data normalized, the azimuthal angles of the magnetization vector in the $x - y$ plane are calculated for each pixel as

$$\phi = \tan^{-1} \frac{M_y}{M_x},$$ (3.2)

and the polar z angles are calculated as

$$\boldsymbol{\theta} = \tan^{-1} \frac{M_{xy}}{M_z},$$ (3.3)

Figure 3.6. Magnitudes of the 3D magnetization vector ($|\boldsymbol{M}(x,y)|$, uniform, left) compared to 2D magnitude of the in-plane components of the magnetization vector ($|\boldsymbol{M_{xy}}(x,y)|$, showing deviations in z, right). The black and white speckles on the 3D image are rounding errors introduced by the normalization algorithm: all values are exactly (or very close to) 1. The black areas in the plot on the left indicate no magnetization in the $x - y$ plane (only in z), while white areas indicate magnetization only in the $x - y$ plane; gray regions have a mix.

where M_{xy} is the magnitude of the $x - y$ component of magnetization.

The resultant array values are thereafter verified by comparing 3D vs. 2D magnitudes of the magnetization, an example shown in Figure 3.6. Individual magnetization components are shown in Figure 3.7, providing additional verification that the data is not systematically flawed in one dimension.
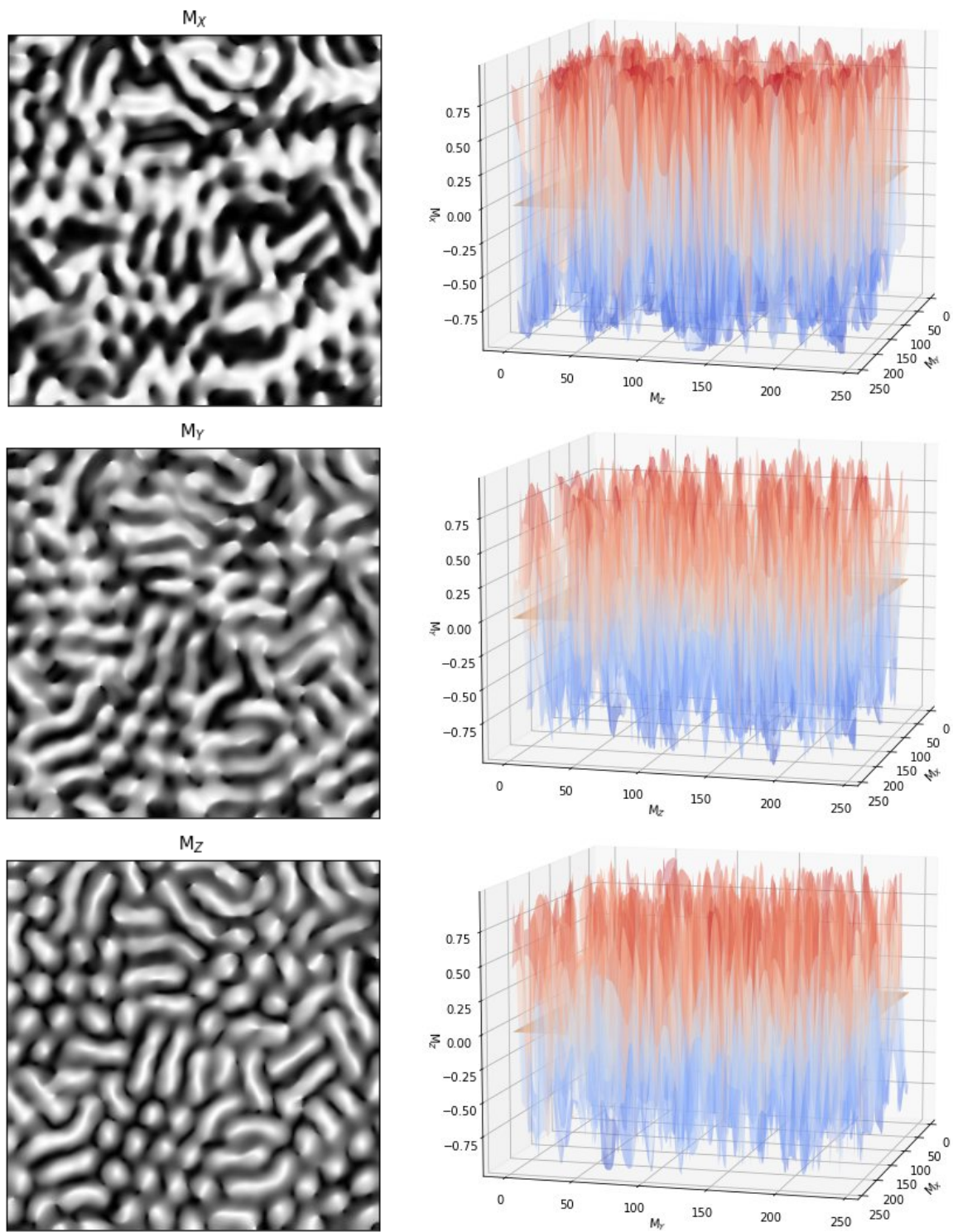
**Figure 3.7.** Normalized magnetization magnitudes in each plane

The next step is selecting features of interest. For the purposes of this work, skyrmions are the primary feature being sought, with the goal of determining their chirality and characterizing their shape at the surface of the material. The achieve this, the feature identification techniques described below are applied.

A binarized version of the θ array is morphologically closed using a 3 pixel wide circular kernel with OpenCV. All closed contours are then found in the image. Any features that reach the edges are discarded in case relevant texture data is out of frame.

The contours are next fit to an ellipse to get width and height. The difference between width and height is compared to a threshold factor multiplied by the maximum of the two, effectively eliminating overly long ovals. The area within the contour is compared to the expected area of a circle with a radius half of the average of the width and height summed, eliminating, for example, concave contours with similar widths and heights. An example of features located is shown in Figure 3.8.

For this work, circular features were the target, and the above methods were executed. The selection process could be modified for other shapes of interest.
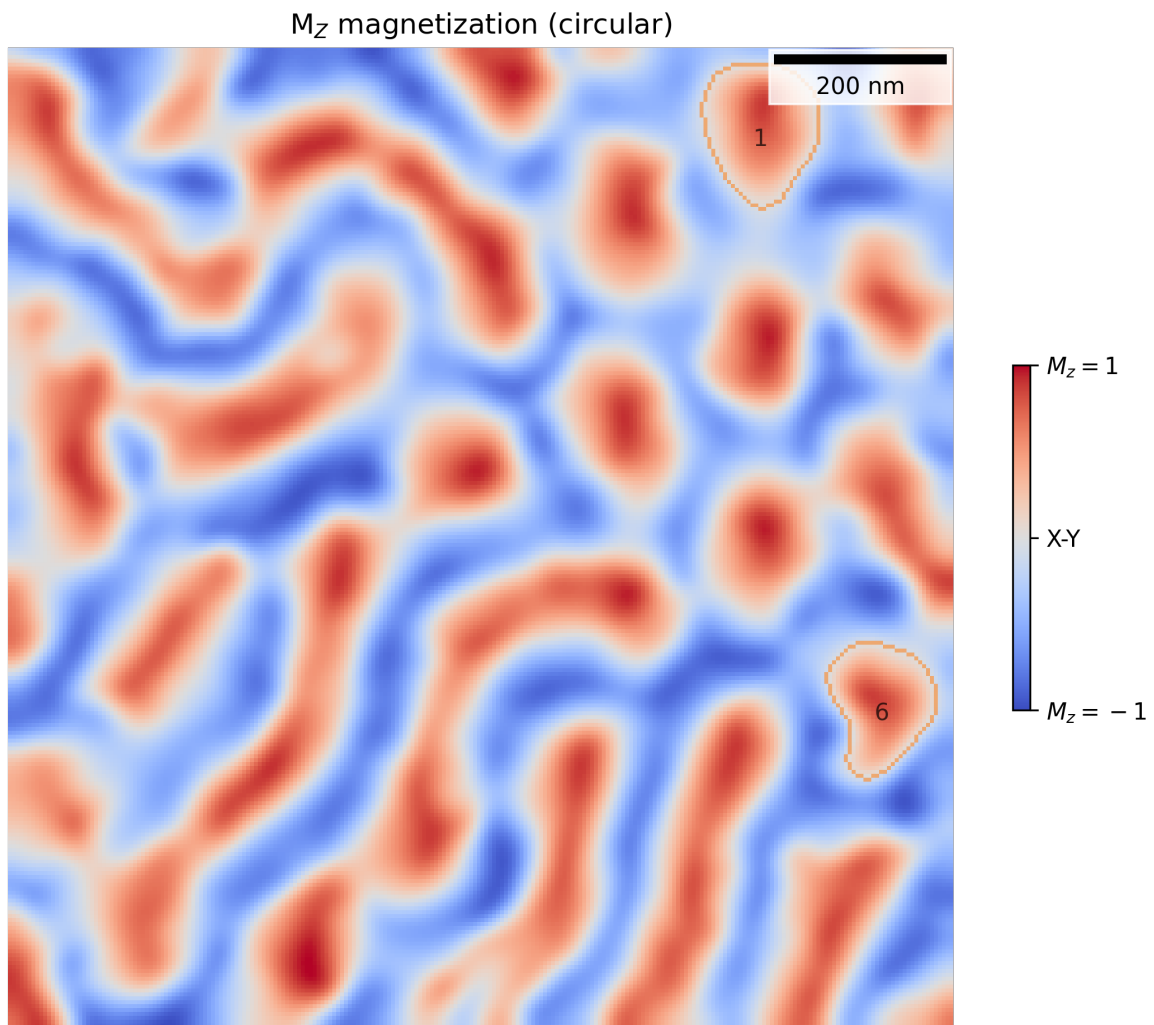
Figure 3.8. In this less than ideal sample, only two roughly circular features were identified by the algorithm, both on the right side of the image.

CHAPTER IV

## ZOOLOGY OF TEXTURES IN FE/GD

The raw SEMPA data used for the analysis presented in this chapter were collected by John Unguris and BenMcMorran at NIST in the last quarter of 2017. The raw LTEM data used for α and size analysis were captured by Will Parker using an FEI Titan in 2022. They have not previously been published.

Results

Figure 4.1 shows an overview of the ~2.3 µm^2 region of $Fe_{0.34}/Gd_{0.40}$ x 120 layers that was analyzed. The background colors show M_z, with blue regions indicating magnetization into the page ($\theta = \pi$) and red regions out of the page ($\theta = 0$); white areas have no z component of magnetization ($\theta = \frac{\pi}{2}$). All contours found are identified and indexed numerically. The outline of each feature indicates average chirality: orange features are clockwise while purple features are anti-clockwise.

Figure 4.2 shows an overview of the same region, this time with background colors indicating $\boldsymbol{M_{xy}}$, the in-plane components of magnetization. The inset top right shows the direction of $\boldsymbol{M_{xy}}$ at each point. Darker areas have a larger z component to the magnetization.

For the investigation of bubble features, each of the contours from Figure 4.1 was evaluated for shape to exclude those that clearly were not skyrmion candidates. The remaining candidate group of features is shown in Figure 4.3.
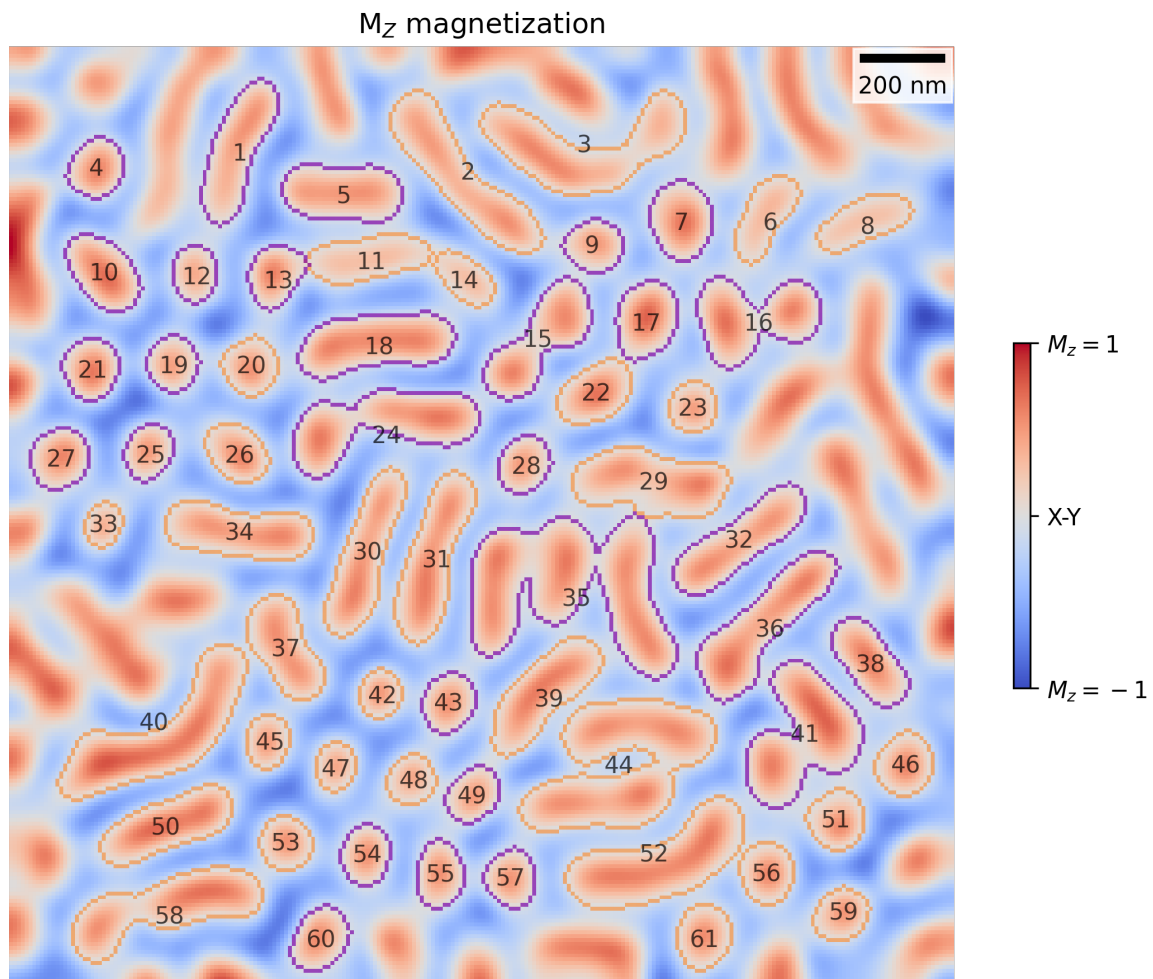
Figure 4.1. Overview of features detected in $Fe_{0.34}/Gd_{0.40}$ x 120 layers . The image colors represent magnetization in z, while the numbered feature outlines indicate chirality: orange is clockwise, purple is anti-clockwise.
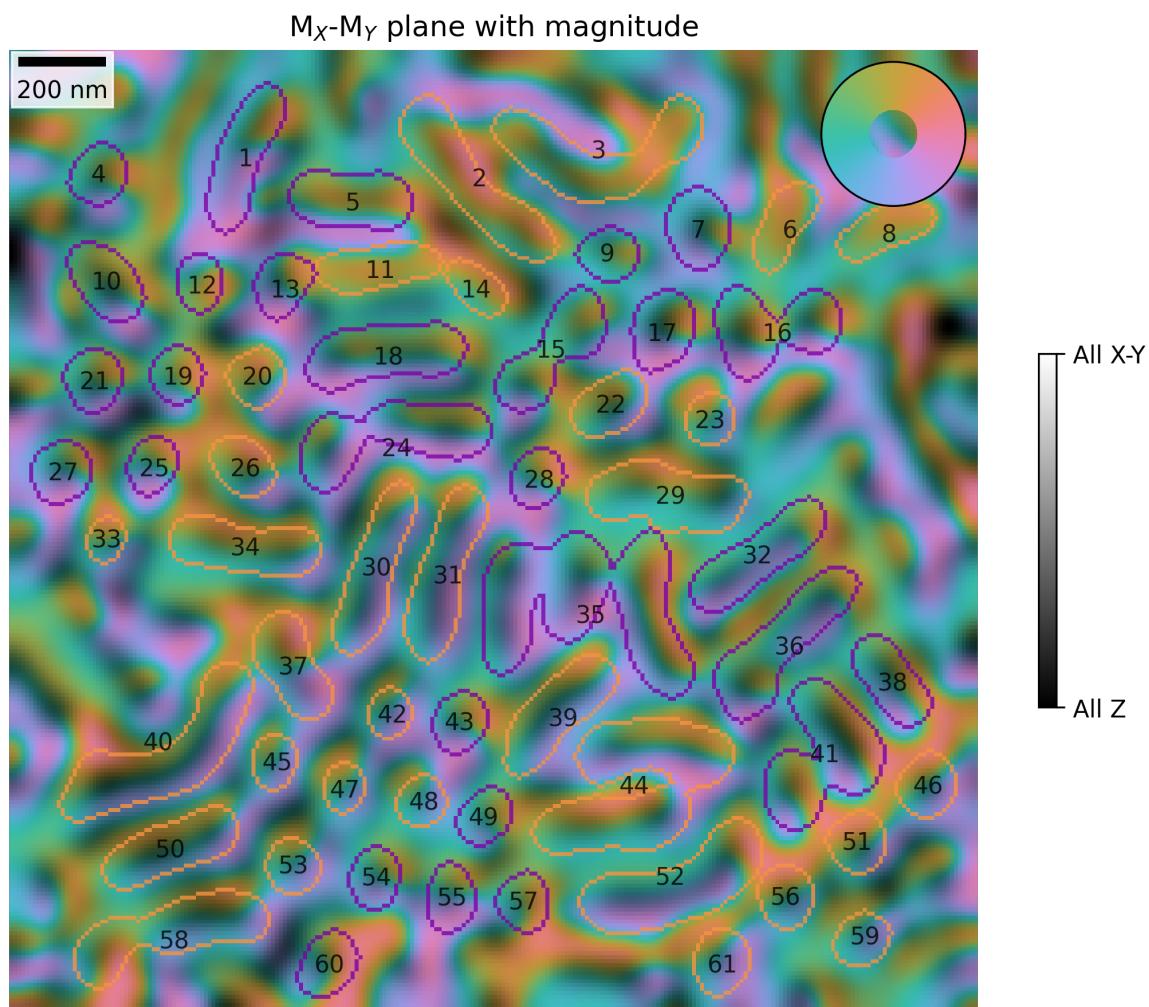
Figure 4.2. Overview of features detected in $Fe_{0.34}/Gd_{0.40}$ x 120 layers . The image colors represent magnetization in the $x - y$ plane. Darker areas are regions where the majority of the magnetization vector is in z.
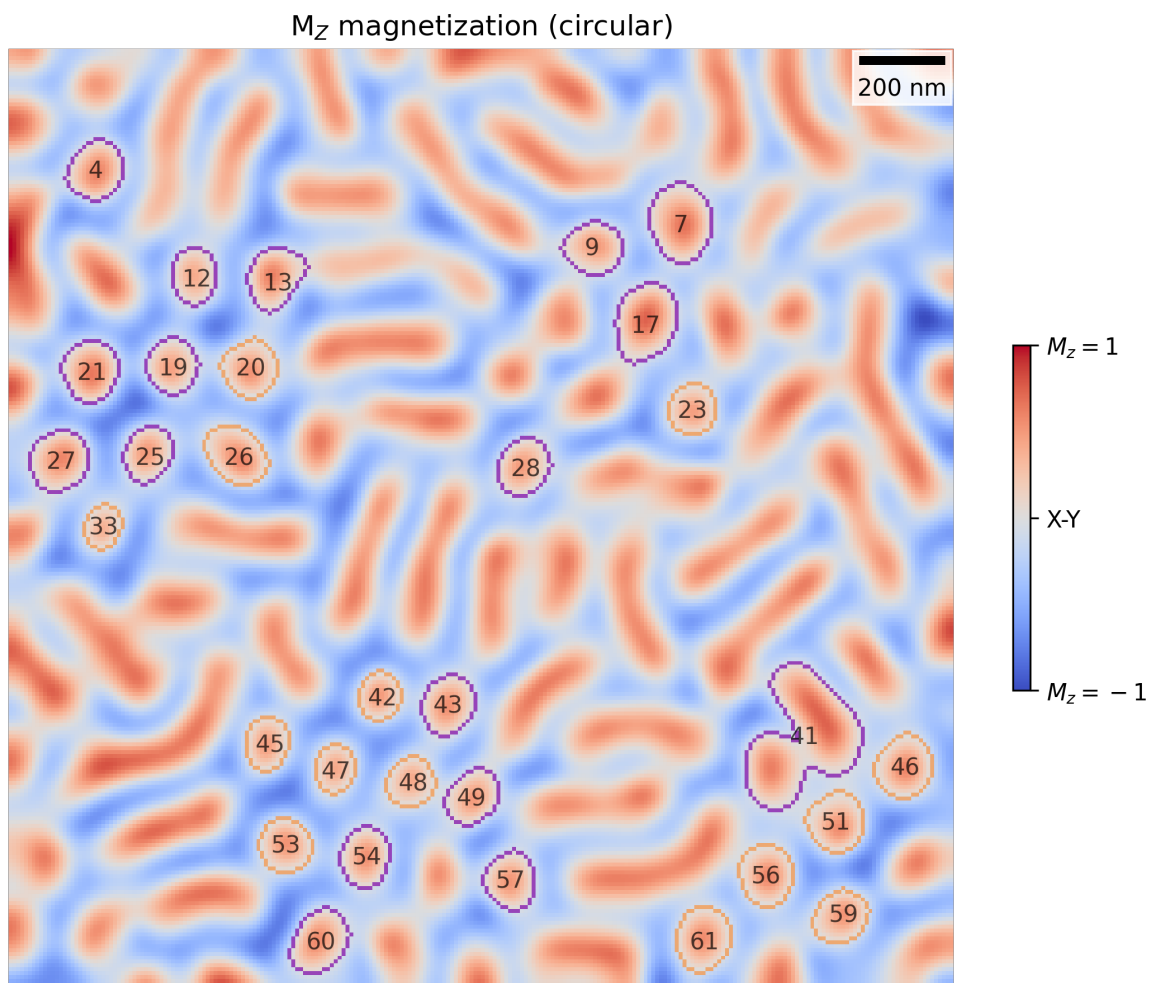
Figure 4.3. Overview of the circular features detected in $Fe_{0.34}/Gd_{0.40}$ x 120 layers . Excluding feature 41, these were used for the following analysis.

Skyrmions

Select skyrmions are shown in Figures 4.4 to 4.7. These met the identification criteria of having $N_{\mathrm{sk}} \approx 1$ with a standard deviation $\sigma < \frac{\pi}{6}$, ensuring they generally followed a consistently-oriented path around the feature. 26 features were identified as skyrmions in this dataset.

The leftmost image for each figure shows the skyrmion and its immediate surrounding. Background colors indicate M_z, with blue into the page, red out of the page, and white indicating $M_z = 0$. The arrows show the in-plane direction of magnetization, M_{xy}. Each image includes an index that can be cross-referenced to the overview in Figure 4.3.

The outermost contours indicate the domain wall at the surface of the sample. For all four images, $p = 1$ as the magnetization points out of the page in the center. Orange contours are clockwise domains with $\frac{\pi}{2} < \alpha < \pi$; purple contours are anti-clockwise with $\pi < \alpha < \frac{3\pi}{2}$.

Plotted to the right of each image is α measured at each point along 3 separate paths: the outermost (orange or purple) as well as $\frac{1}{3}$ of the radial distance out from the maximum enclosed M_z, represented by the black dot, and $\frac{2}{3}$ of the radial distance out to the outermost. These paths are represented by the yellow and green dotted rings, respectively. In all cases, α is calculated by walking clockwise around the contour (starting on the outer contour at the red dot, proceeding around to yellow, green, blue, and back to red). The averages at each radial distance are plotted with dashed lines. Errors for the contour are within the light blue shaded areas.

The image locations in the overall scan are displayed, along with feature dimensions. Additional statistics are presented, including average α along all 3 paths, average path angles ϕ, and winding number n.

(167, 83) to (186, 103), 117x126 nm
α: 2.31, σ_α: 0.30 ϕ_{dev}: 2.66, σ_{dev}: 2.90 n: 0.89

α: 1.62 to 2.81, 2.31 (2.37, 2.41) average
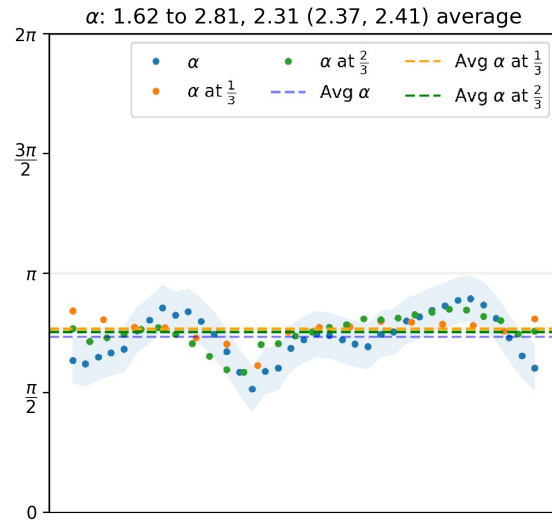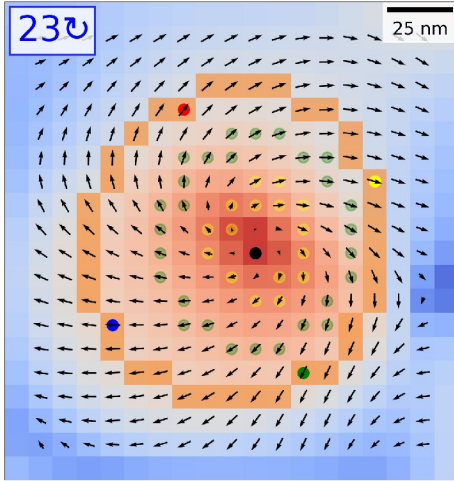
Figure 4.4. Clockwise skyrmion. The values for α plotted on the right show the values and averages $\frac{1}{3}$ and $\frac{2}{3}$ of the radial distance from the point of maximum M_z (measured at the yellow and green dotted locations in the image on the right), as well as at the contour. The values of α for the contour are plotted along the x axis starting from the red dot, proceeding clockwise through yellow, green, and blue.

(1, 94) to (25, 119), 144x153 nm
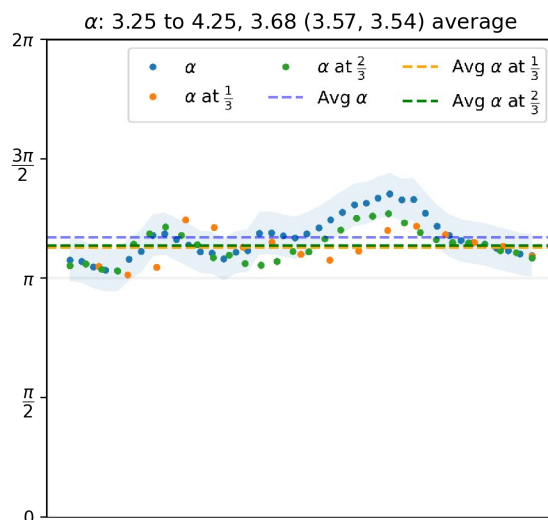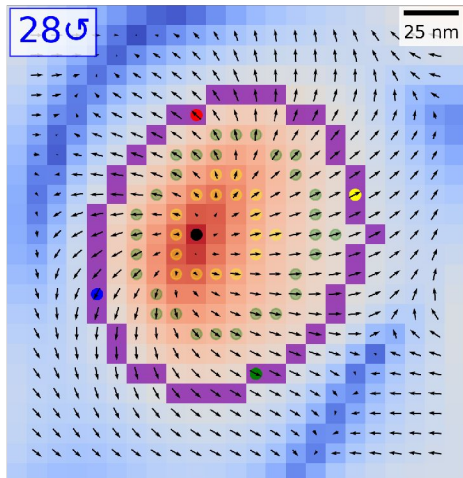α: 3.86, σ_α: 0.26 ϕ_{dev}: 3.23, σ_{dev}: 2.09 n: 1.06

α: 3.51 to 4.55, 3.86 (3.68, 3.62) average
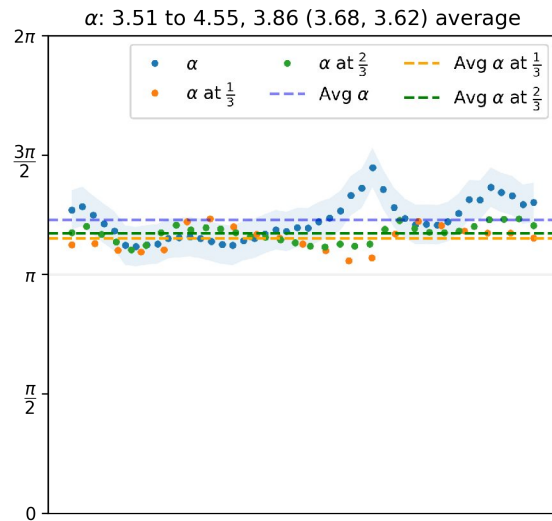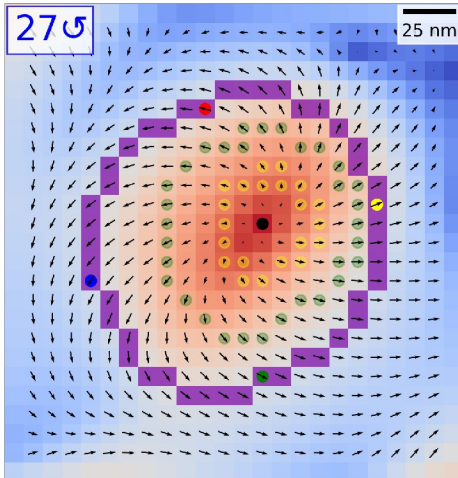
Figure 4.5. Anti-clockwise skyrmion.
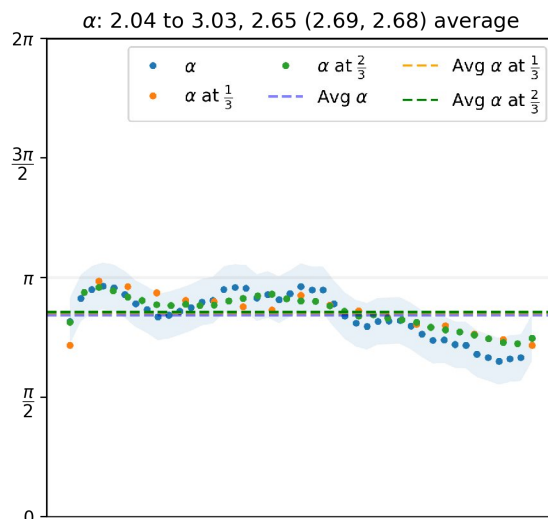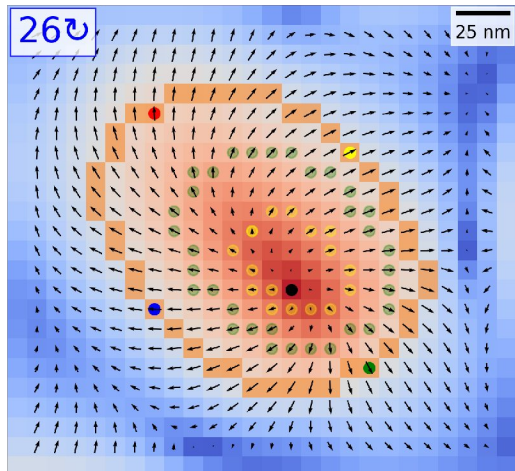
Figure 4.6. Clockwise skyrmion.

Figure 4.7. Anti-clockwise skyrmion.

Antiskyrmions

The two antiskyrmions that were identified are shown in Figures 4.8 and 4.9. These met the identification criteria of having $N_{\mathrm{sk}} \approx -1$ and a generally circular shape (enclosed area within $\pm 30\%$ of the area of a circle with $r = \frac{\mathrm{width} \times \mathrm{height}}{2}$).

Image color schemes follow the same pattern as above, though the contour color only represents the numeric average for α.

Trivial Bubbles

The two topologically trivial bubbles that were found are shown in Figures 4.10 and 4.11. These met the identification criteria of having $N_{\mathrm{sk}} \approx 0$ and a generally circular shape (enclosed area within $\pm 30\%$ of the area of a circle with $r = \frac{\mathrm{width} \times \mathrm{height}}{2}$).

As for antiskyrmions, image color schemes follow the same pattern as for skyrmions, with the contour color again only representing the numeric average for α.

Worms

Two worm domains that were identified are shown in Figures 4.12 and 4.13. Worm domains are longer in one dimension than the other, generally created when labyrinth domains (much longer) get pinched off during skyrmion nucleation.
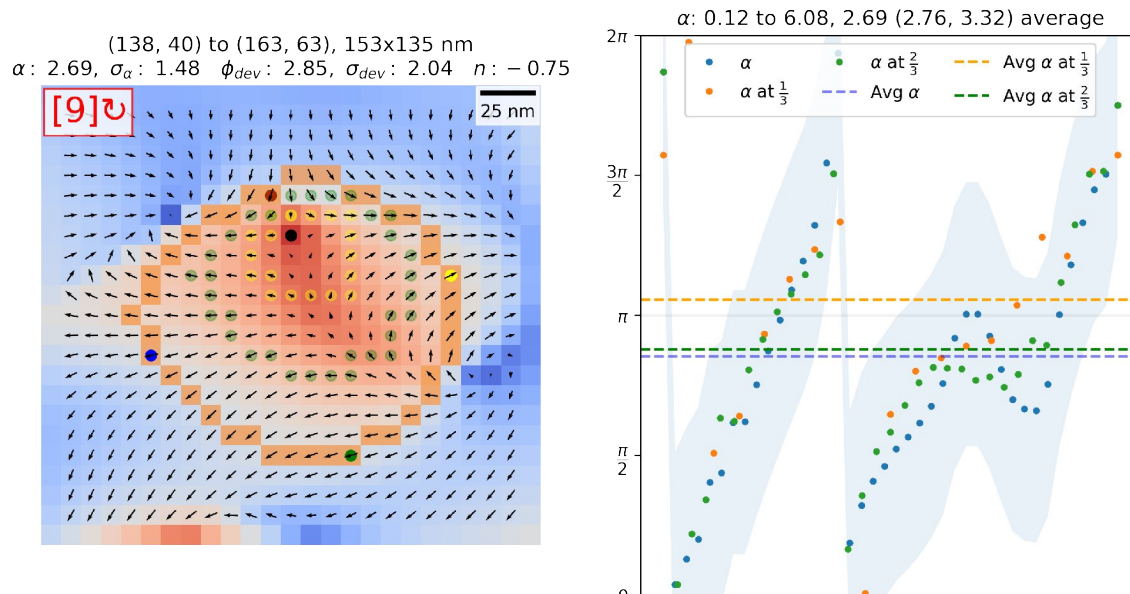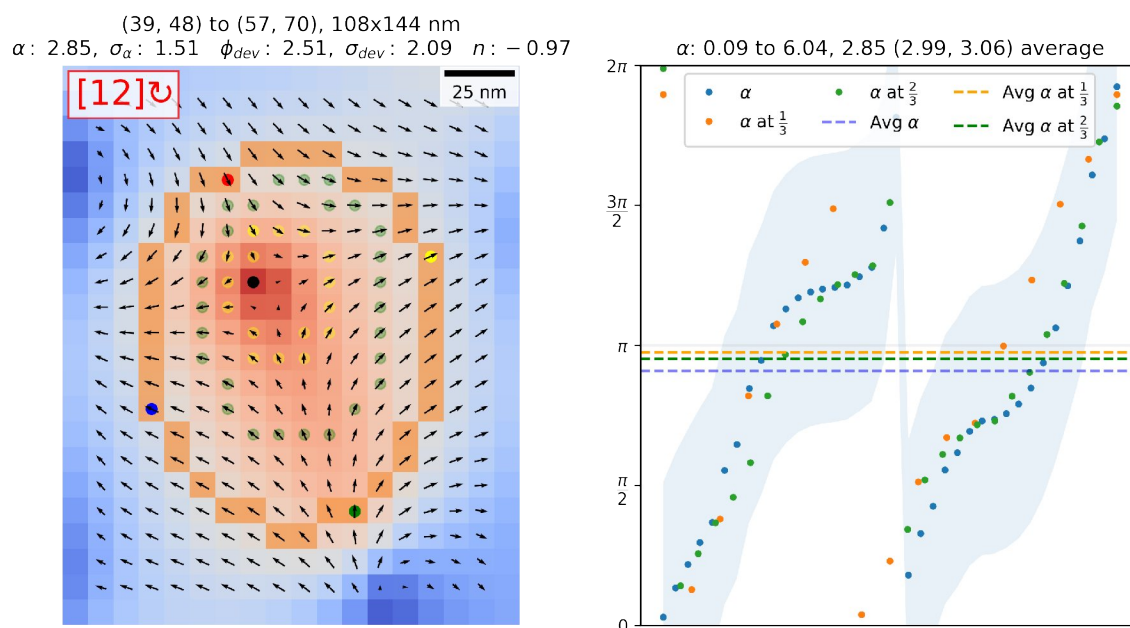
As above, image color schemes follow the same pattern as for skyrmions, with the contour color again only representing the numeric average for α.

(138, 40) to (163, 63), 153x135 nm
α: 2.69, σ_α: 1.48 ϕ_{dev}: 2.85, σ_{dev}: 2.04 n: −0.75

α: 0.12 to 6.08, 2.69 (2.76, 3.32) average

Figure 4.8. Antiskyrmion with magnetization lines flowing in at 12 and 4 o'clock, out at 2 and 9 o'clock.

(39, 48) to (57, 70), 108x144 nm
α: 2.85, σ_α: 1.51 ϕ_{dev}: 2.51, σ_{dev}: 2.09 n: −0.97

α: 0.09 to 6.04, 2.85 (2.99, 3.06) average
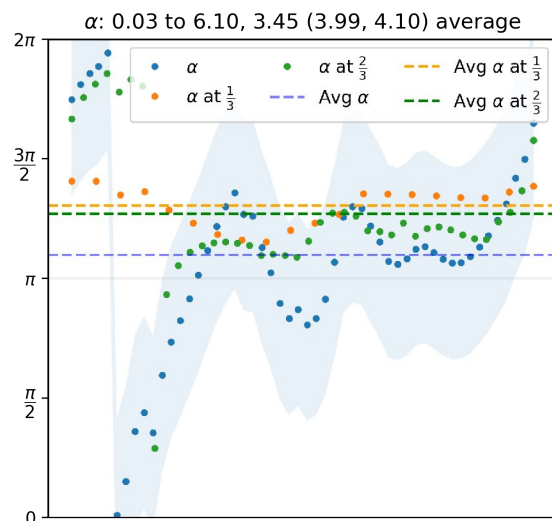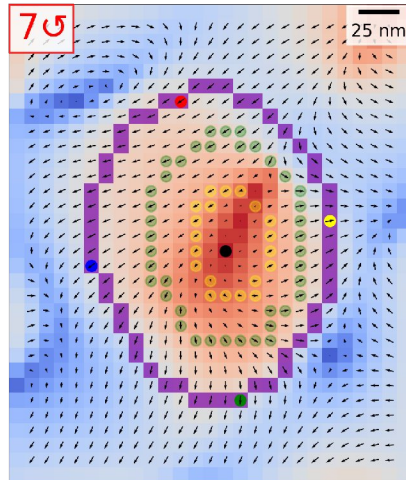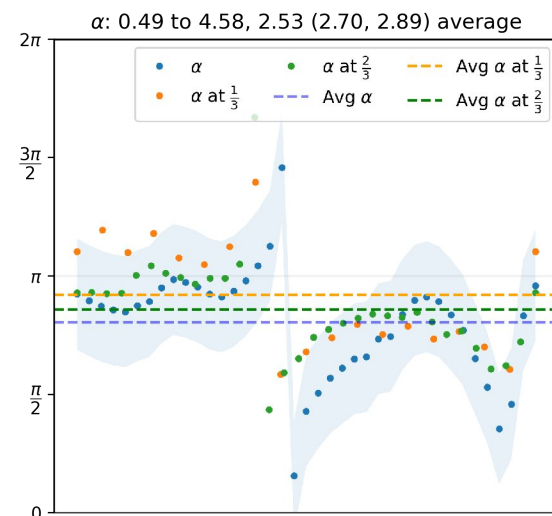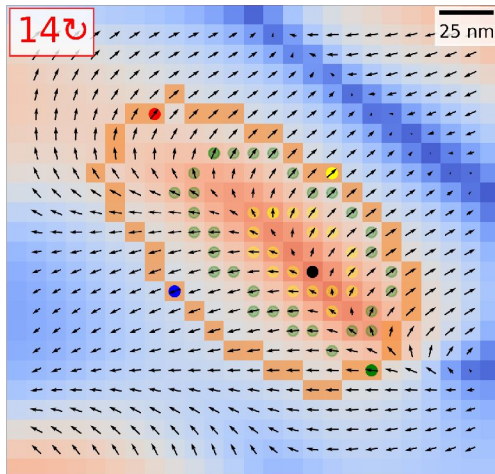
Figure 4.9. Antiskyrmion with magnetization lines flowing in at 11 and 5 o'clock, out at 2 and 8 o'clock.

65

Figure 4.10. Trivial bubble with lines flowing from 1 to 7 o'clock.

Figure 4.11. Trivial bubble with lines flowing from 4 to 9 o'clock and 1 o'clock.
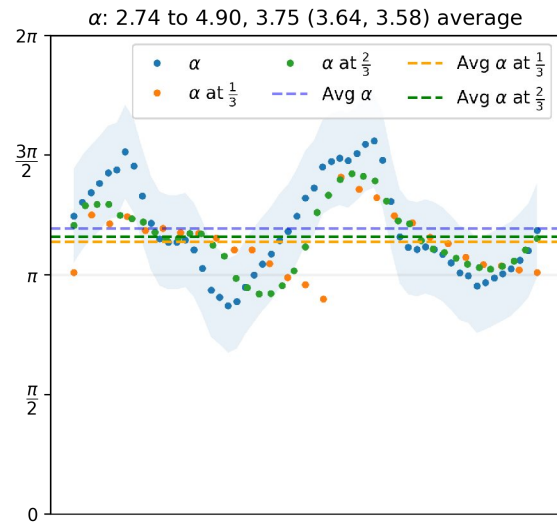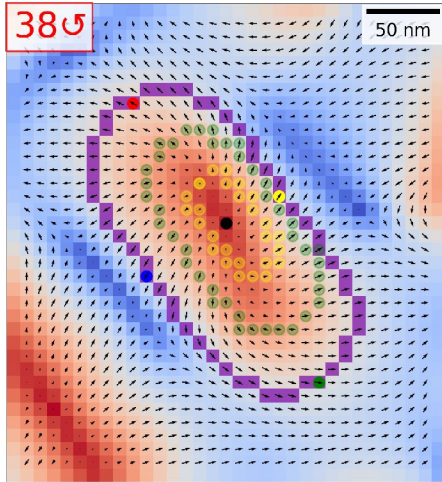
Figure 4.12. Worm domain roughly 290 nm long.
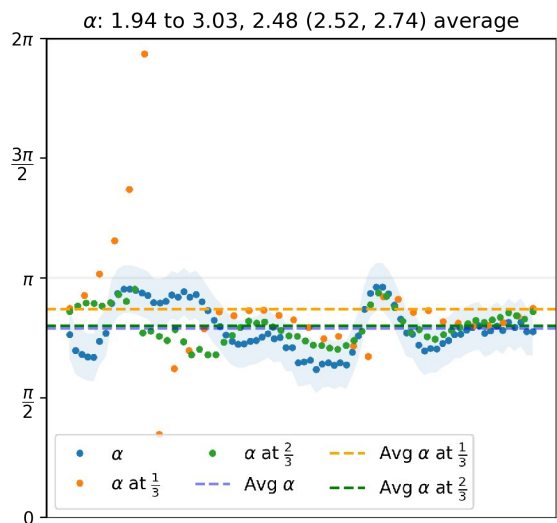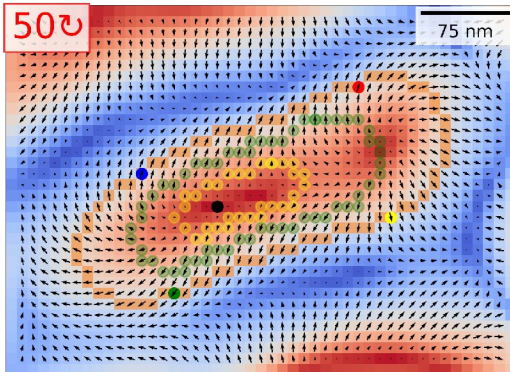
Figure 4.13. Worm domain roughly 375 nm long.

Two regions of skyrmion groups are shown in Figures 4.14 and 4.15.

While the color scheme follows the above images, the numbering here is based on the indices of circular contours only.

Figure 4.14 maps to features in the top left of Figure 4.3 (namely, 12, 13, 19, 20, 21, 25, 26, 27, and 33).

Figure 4.15 maps to features just left of bottom center of Figure 4.3 (namely, 42, 43, 45, 47, 48, 49, 53, 54, 57, and 60).

Distribution of Magnetization Angles Across Features

Figure 4.16 shows the distribution of average α values calculated from both SEMPA and LTEM data. As defined in Background, α is a measure of deviation of the magnetization vector along a path (the domain wall in this case) from the direction of increasing M_z.

The blue bars represent α for the skyrmions identified in the sample analyzed by SEMPA. The averages along with error for this bimodal distribution are shown at the top, outlined in blue. The orange bars represent α for the skyrmions identified in a similar sample analyzed on the TEM. The averages along with error for this bimodal distribution are overlaid, outlined in orange. The green outlines represent α for the all features identified in the sample analyzed by SEMPA. The averages along with error for this bimodal distribution are included, outlined in green.
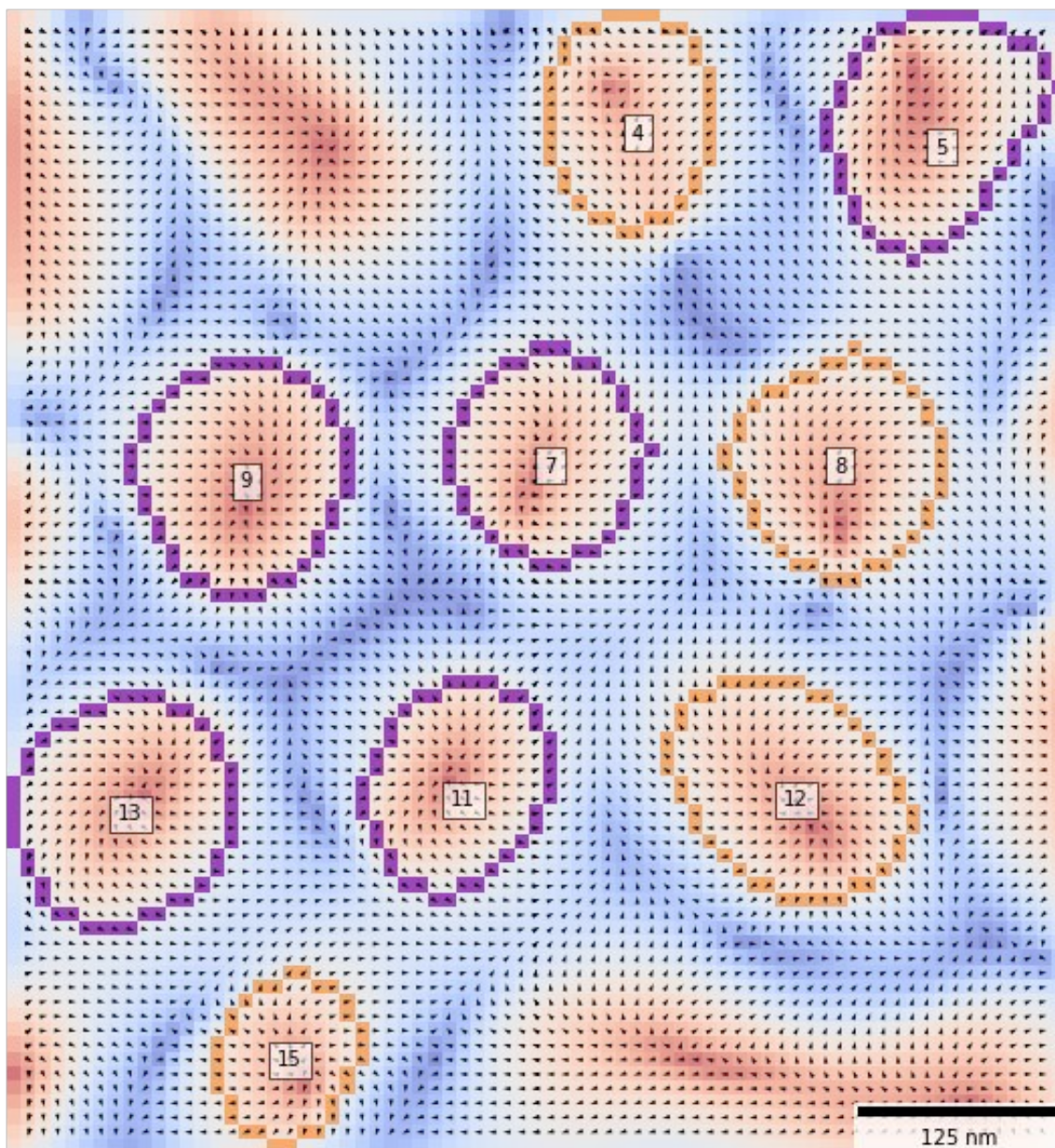
Figure 4.14. A cluster of skyrmions adjacent to each other.
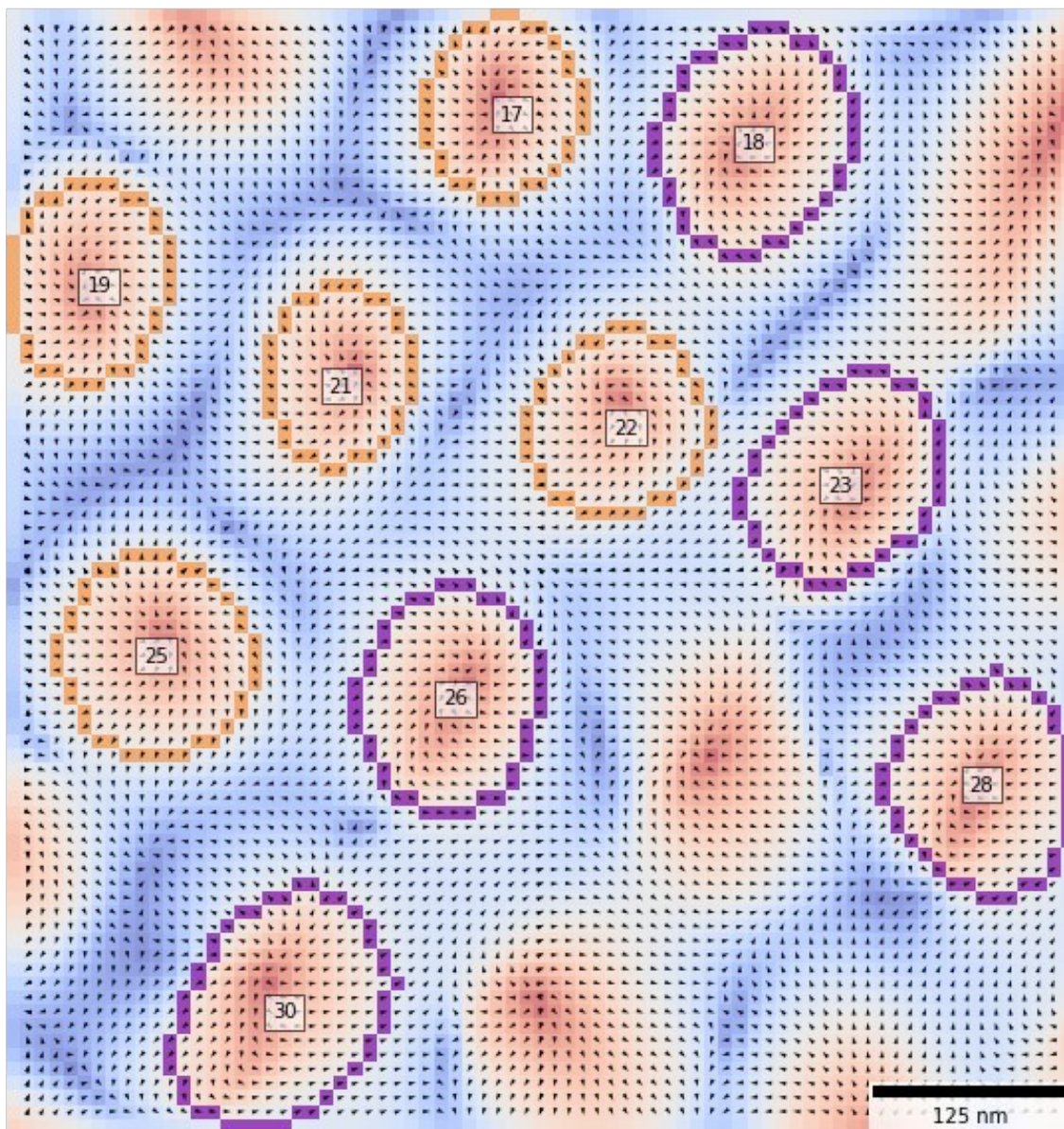
Figure 4.15. Another cluster of skyrmions adjacent to each other.
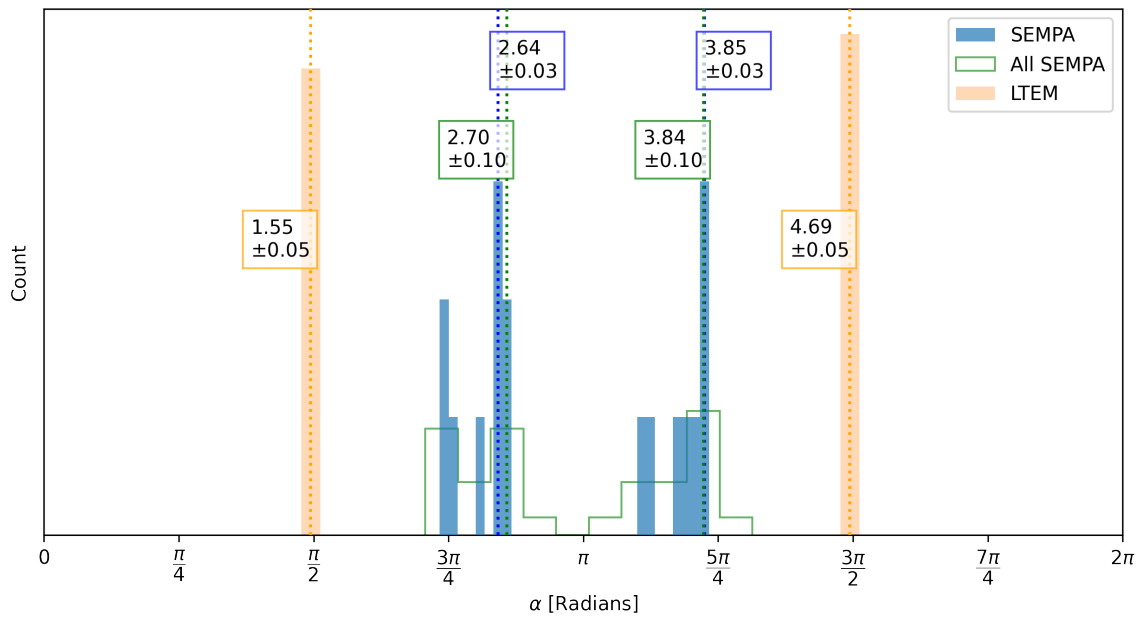
Figure 4.16. Distribution of α calculated from SEMPA data (blue bars for circular features, green outline for all detected features) and LTEM data (orange bars).
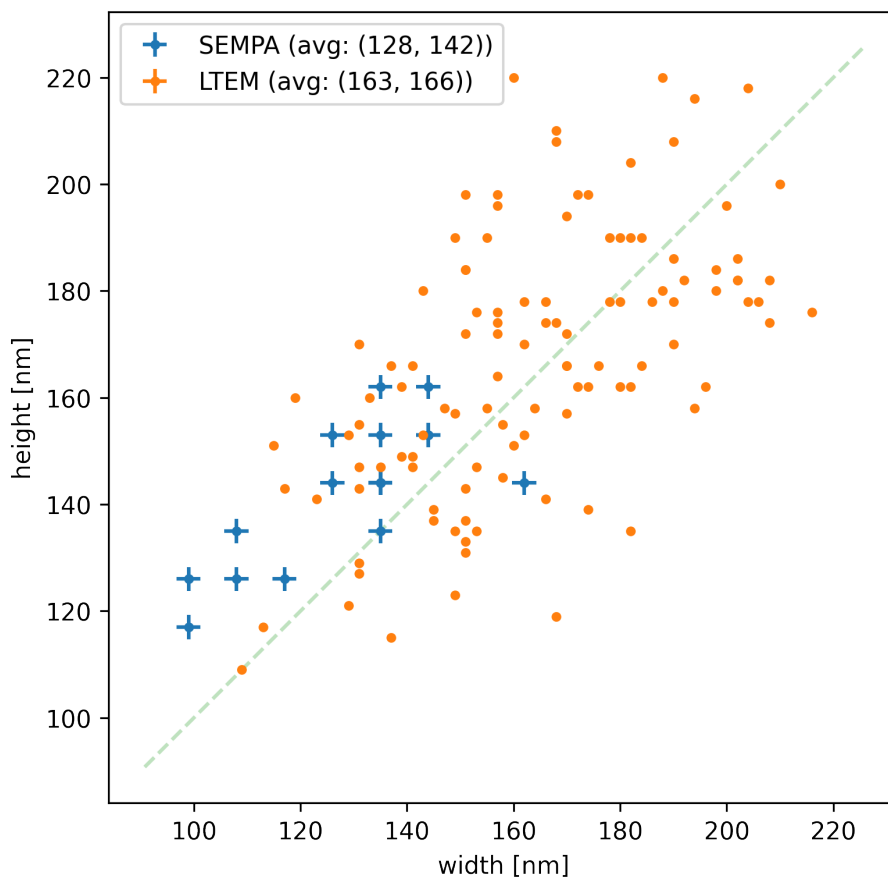
Figure 4.17. Comparison of circular feature sizes from SEMPA data (blue) and LTEM data (orange). The uniform spacing in both cases is due to the square grid of pixels used to calculate these values.

Comparison of Skyrmion Sizes from SEMPA and LTEM

Figure 4.17 shows the distribution of average feature dimensions measured from both SEMPA and LTEM data.

SEMPA measurements are shown in blue with error bars; TEM measurements are shown in orange with errors. The resolution of the TEM is roughly 10x that of the SEMPA, made apparent by the significantly smaller errors for the TEM data.

Figure 4.18 shows an overview of the ~3.9 µm^2 region of Fe$_{0.34}$/Gd$_{0.40}$ x 120 layers that was analyzed with the TEM.
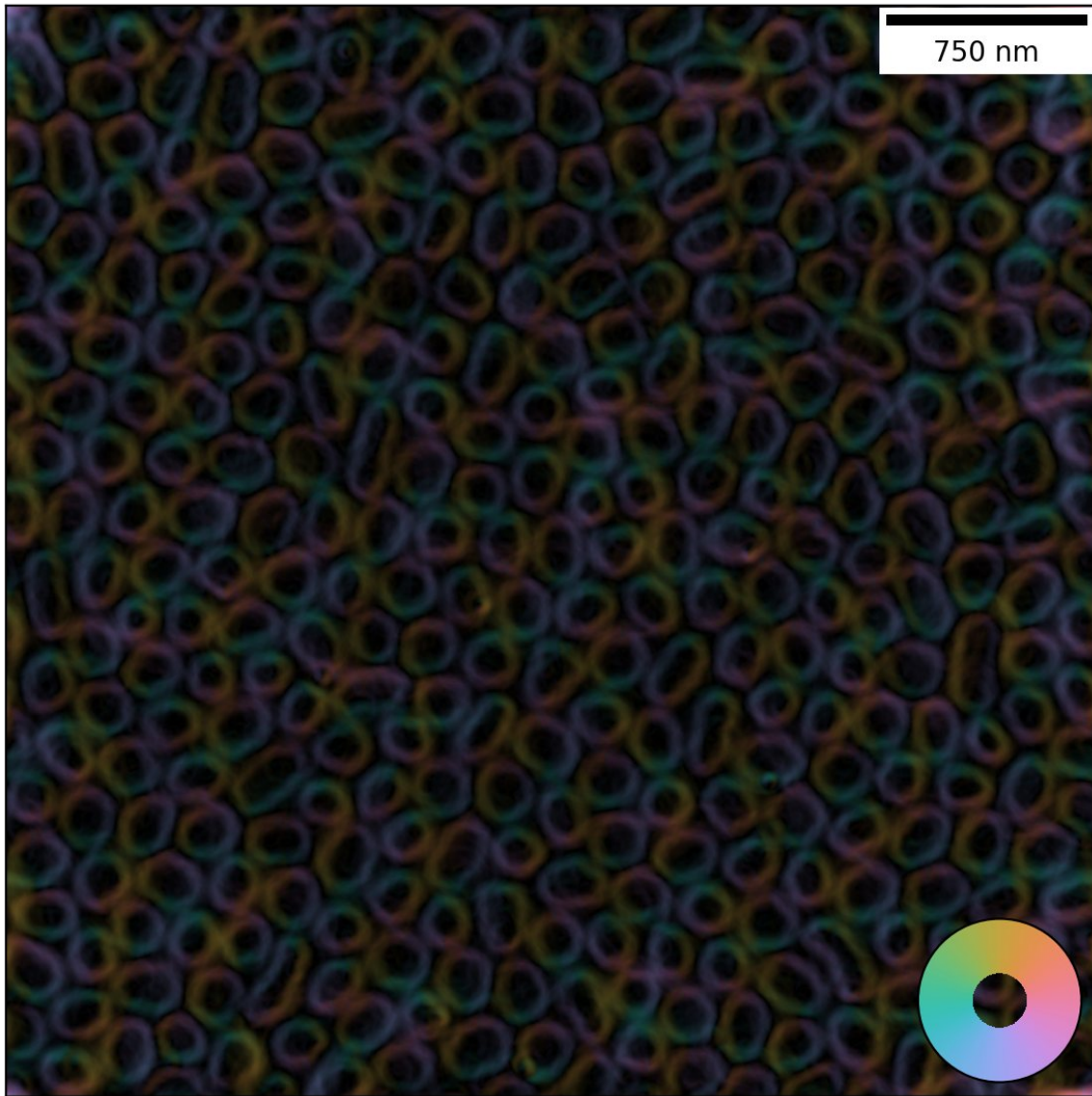
Figure 4.18. Overview of the circular features detected in $Fe_{0.34}/Gd_{0.40}$ x 120 layers imaged with LTEM. Inset color wheel shows the direction of magnetization in the domain walls. The numbering is suppressed to avoid obscuring the features.

Discussion

Shapes Observed

As shown in Figures 4.1 to 4.3, a wide variety of textures were found in the sample, including skyrmions, antiskyrmions, trivial bubbles, and worm domains.

A feature (indeed, the most significant feature for this research) of $Fe_{0.34}/Gd_{0.40}$ x 120 layers is that the magnetic textures created after the second exposure to an external field (400 mT, 0 mT, 185 mT) remain at remanence, stabilized by the behavior described in the section Long range dipolar interaction. This feature, appealing for many spintronic applications, is not the case in many materials.

Skyrmions

Of 61 total features detected, 31 were circular, with 20 of those likely candidates for skyrmions. Several are shown above in Figures 4.4 to 4.7. α between $\frac{\pi}{2}$ and π rotate clockwise in an increasingly outward radial direction as α increases; α between $\frac{3\pi}{2}$ and π rotate anti-clockwise with an increasingly outward radial direction as α decreases.

Figure 4.16 shows that LTEM data is effectively evenly split between clockwise and anti-clockwise Bloch walls, as expected, with any other magnetization apparently purely perpendicular to the plane of the sample.

SEMPA data, however, shows a different story. At the surface, magnetization is only purely in the z direction somewhere near the center of the domains. The magnetization develops x and y components, creating hybrid Néel/Bloch walls. The value of α generally decreased/increased for anti-clockwise/clockwise skyrmions as the radial distance from maximum M_z increased as shown for several skyrmions in Figure 4.19, with a specific example shown in Figure 4.20.

This is particularly interesting when combined with the dimensions of skyrmions measured with LTEM versus SEMPA, shown above in Figure 4.17. The skyrmion diameters, defined where $M_z = 0$, measured at the surface with SEMPA are, on average, 135 nm $\pm$ 4.5 nm, whereas the diameter of the projected image with LTEM are, on average, 165 nm $\pm$ 1.0 nm.

A simulation of this shape at several z heights using Jordan Chess's skyrmion plotting model is shown in Figure 4.21. The domain wall edges move outward radially as the plot moves closer to the center of the bulk.

This suggests that the magnetization continues to rotate in plane while moving out radially and down into the bulk until the domain wall is purely Bloch-like at $\alpha = \pm\frac{\pi}{2}$, creating more of a barrel shape than the cylinder normally suggested. This corroborates Alice Greenberg's simulations and observations[87].

Continuing to analyze the 3D shape of the magnetization, the angle α (that is, relative to a line pointing radially to the center of the toroid as would be the case if magnetization were pointing up in the center of the toroid) at the topmost surface of a toroid with W from 1 to 10 were measured. An example of this setup including 2 lines with $W = 5$ is shown in Figure 4.22.

A plot of the extrema of measured α from SEMPA along with a cubic spline fit of the toroid wrapping angles is shown in Figure 4.23. From this it would appear that the lines of magnetization wrap around the barrel shape between 2 and 8 times. Depending on how mathematically rigorous one is, some researchers would argue this is taking a form at least superficially like a hopfion[118, 119], shown schematically in Figure 4.24.
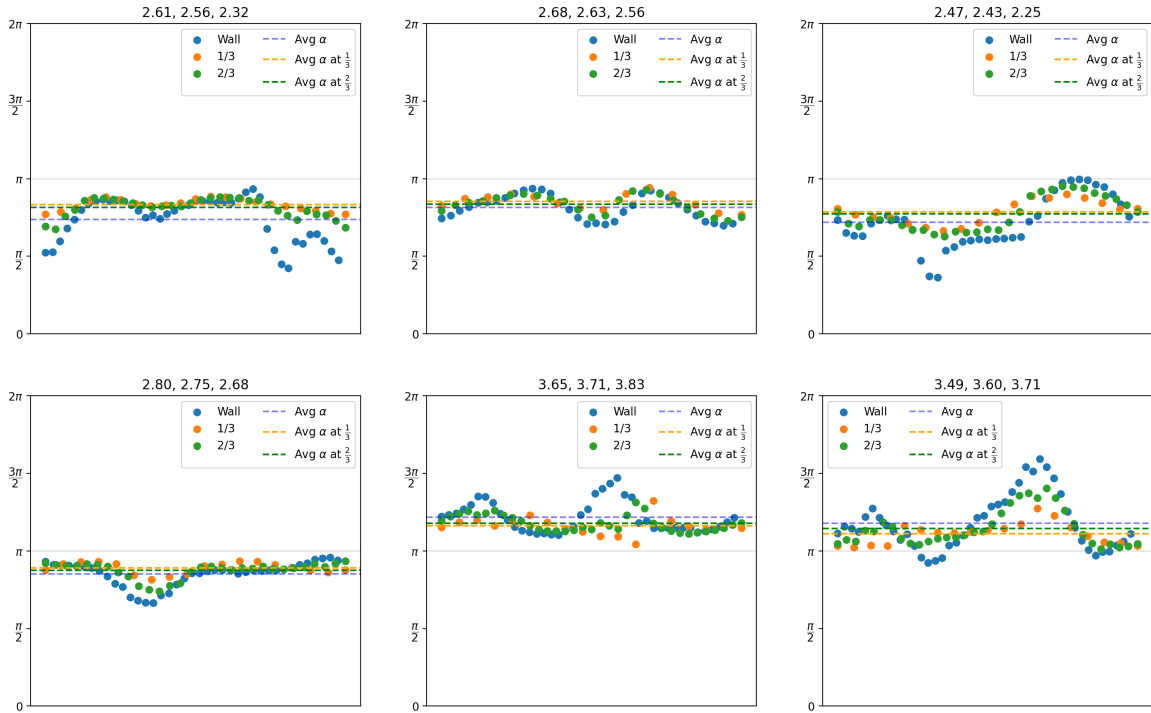
Figure 4.19. α values for several skyrmions at the film surface. The first four plots are clockwise skyrmions. In each case, the value of α decreases toward $\frac{\pi}{2}$ as the radial distance increases, indicating that the direction of magnetization is transitioning from more Néel-like to more Bloch-like. The bottom 2 plots are anti-clockwise skyrmions, where the value of α increases toward $\frac{3\pi}{2}$, also becoming more Bloch-like as the radius increases.
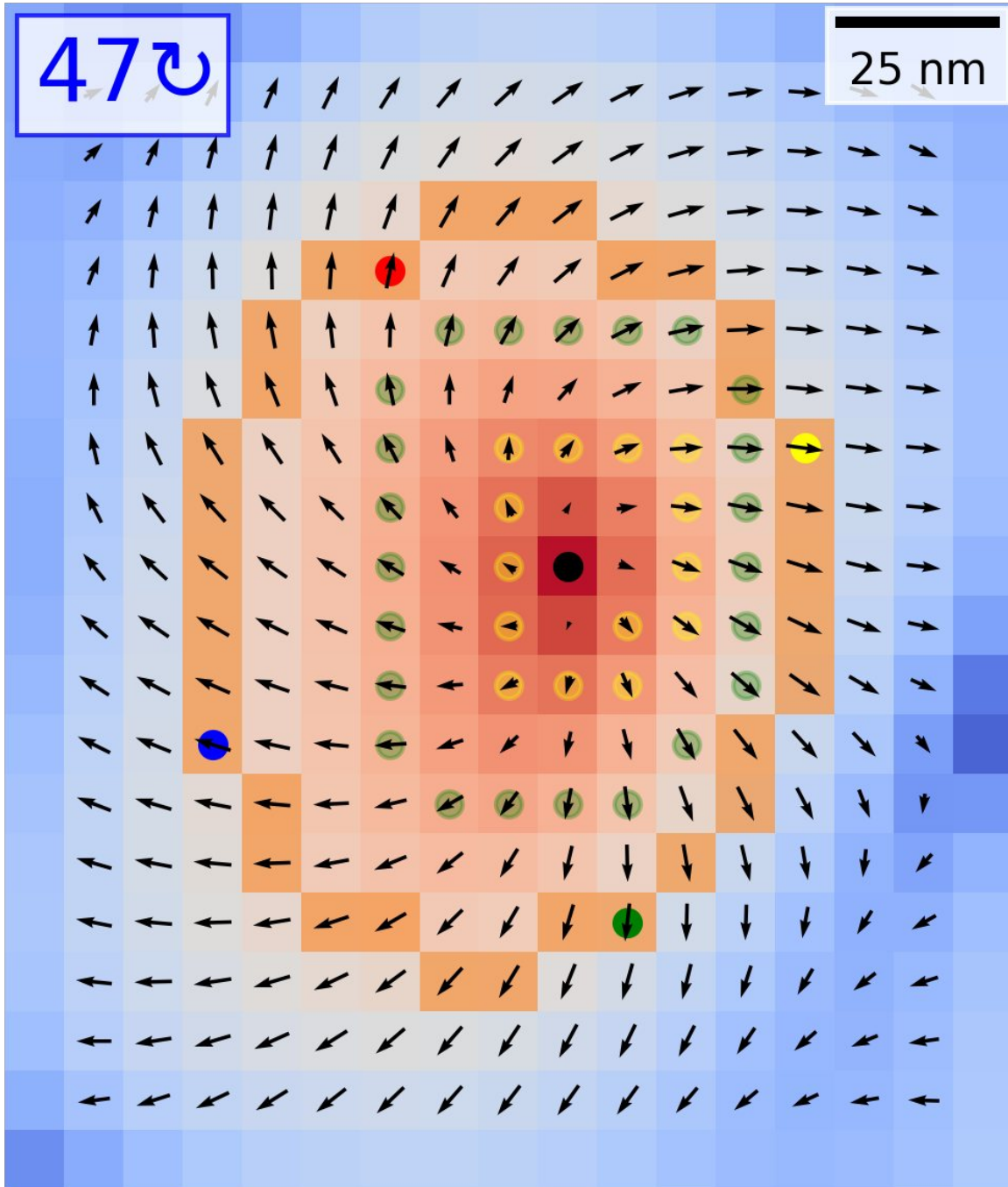
Figure 4.20. Average α for this skyrmion decreases from 2.68 along the path of the yellow dots $\frac{1}{3}$ of the distance from maximum M_z at the black dot to the orange domain wall to 2.63 along the path of green dots at $\frac{2}{3}$ of the distance to the wall to 2.56 along the domain wall.
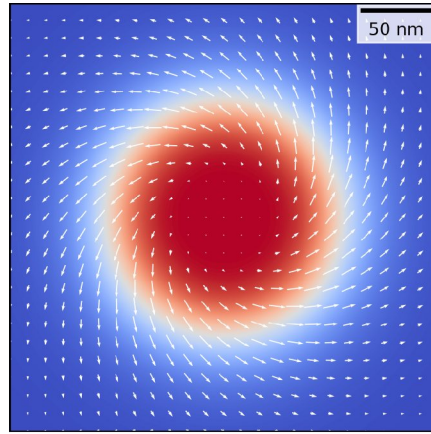
(a)
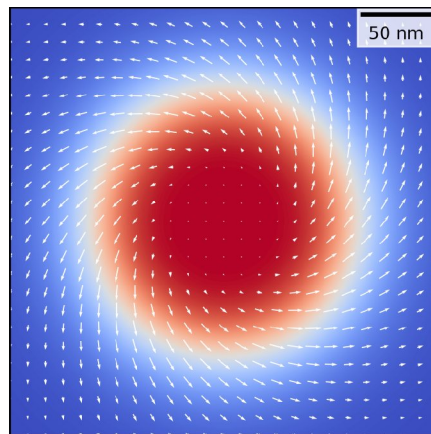
(b)
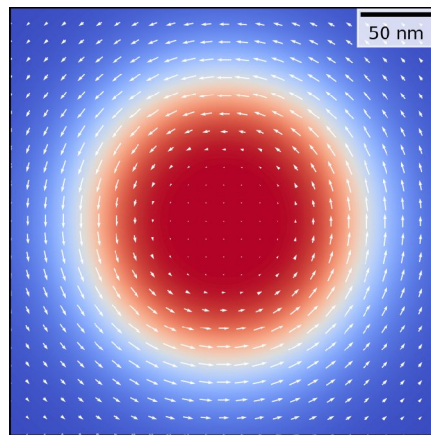
(c)

Figure 4.21. Simulated barrel-shaped domain wall: (a) hybrid Néel/Bloch walls at the surface; (b) more Bloch-like walls partway into the bulk; (c) and purely Bloch walls at the center of the bulk. Red is out of the page, blue into the page, with white indicating $M_z = 0$. White arrows show M_{xy}.
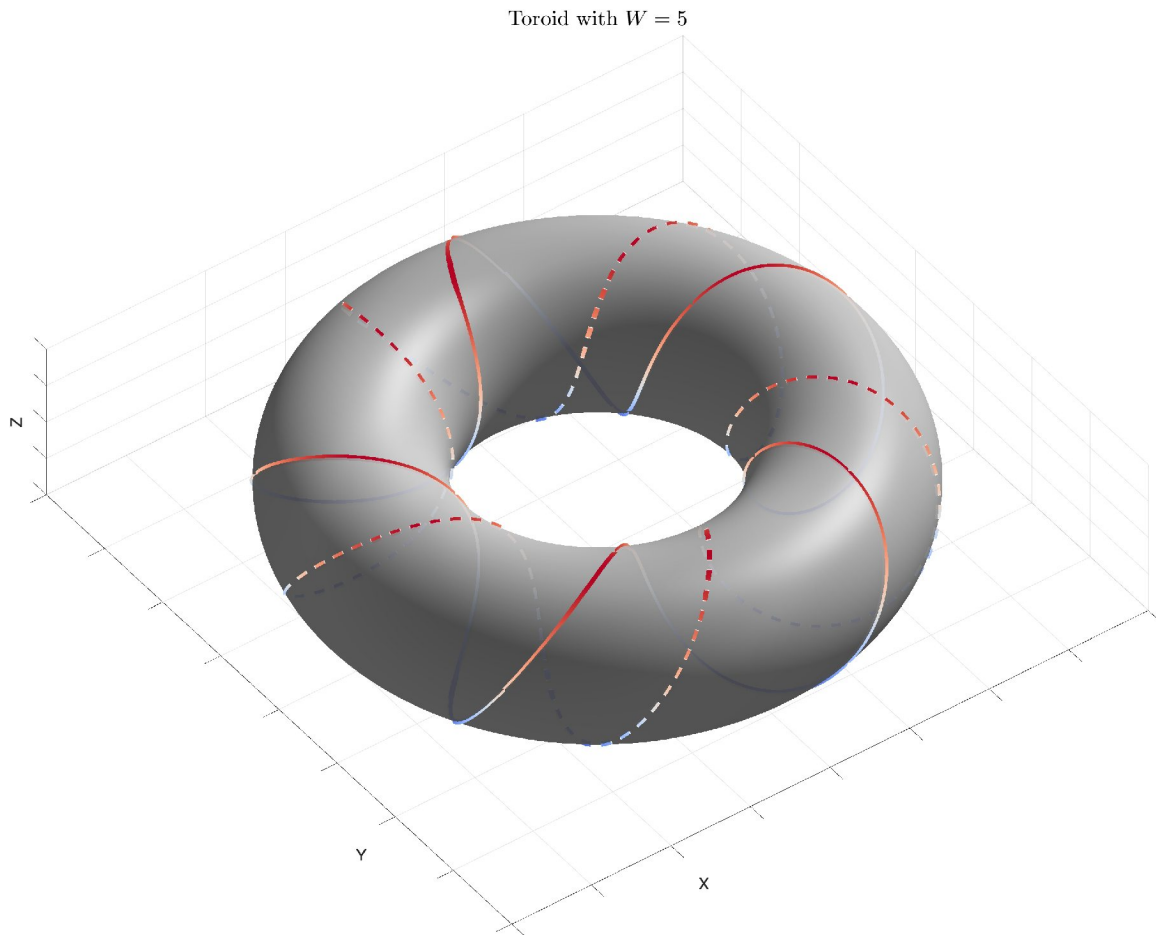
Figure 4.22. Toroid wrapped with 2 lines with $W = 5$. Red regions on the wrapping contour are on top of the toroid, while blue regions are on the bottom. $\alpha \approx 2.675$ at each point of maximum z.
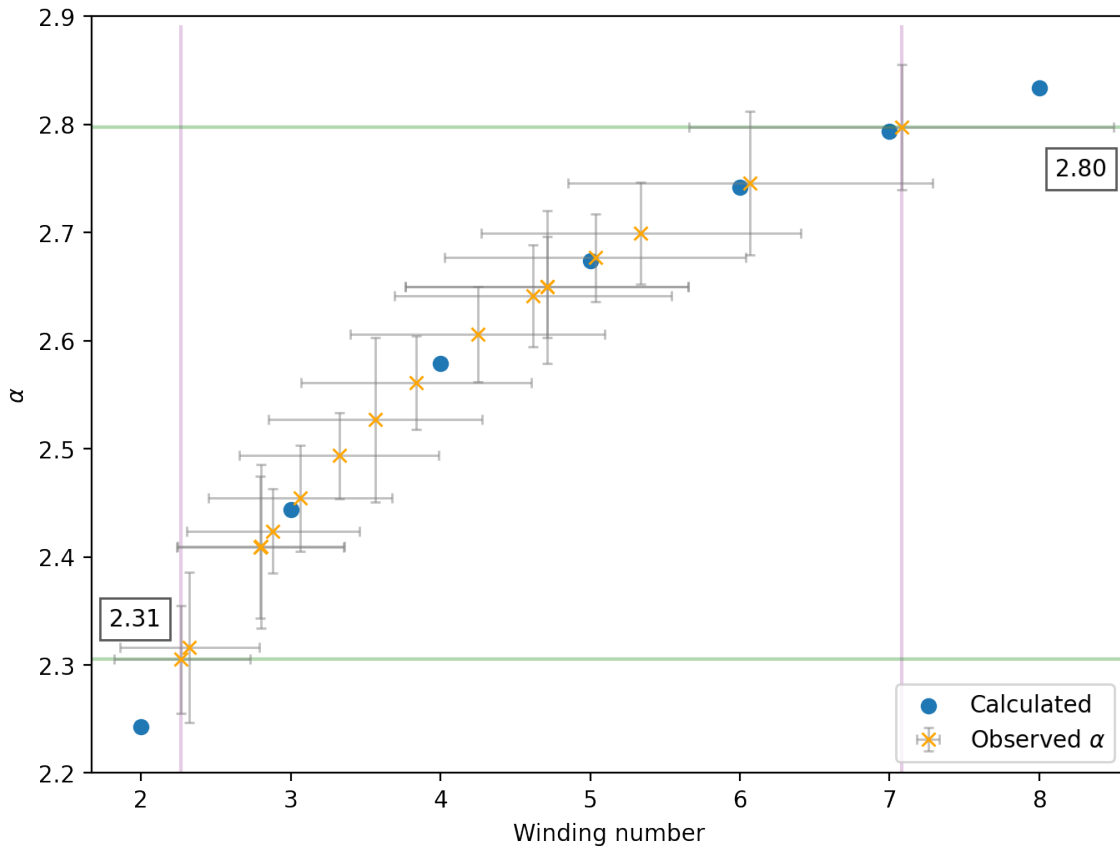
Figure 4.23. Measured α for several winding numbers around a toroid. Orange X's indicate observed α values fitted to a simulated toroid with similar dimensions; the horizontal green lines show the extrema of α observed in the sample. The vertical purple lines show the range of observed winding numbers. The blue dots are integer winding values calculated from the simulated toroid.
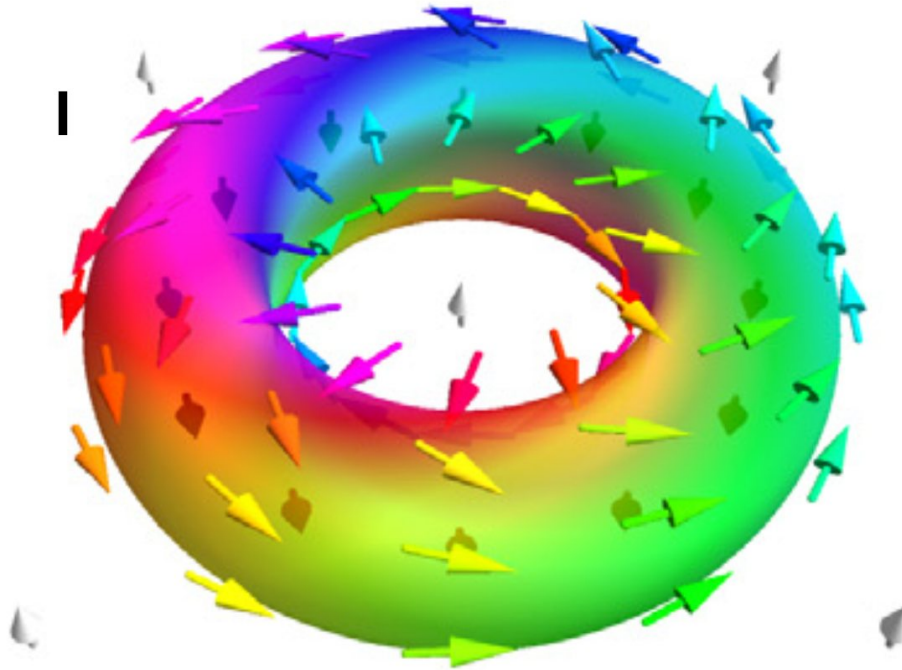
Figure 4.24. Schematic of a hopfion, an object with closed lines wrapping around both θ and ϕ before meeting back up where they started. Figure reproduced with permission from "Beyond skyrmions: Review and perspectives of alternative magnetic quasiparticles" by Börge Göbel, Ingrid Mertig, and Oleg A Tretiakov in Physics Reports 895 (2021), p. 4.

Antiskyrmions

Of the 31 circular features found, 2 were antiskyrmions, shown above in Figures 4.8 and 4.9.

The α plots confirm the expected double rotation of the magnetization vectors while traversing around the domain wall.

Two unexpected observations were made with these textures: an asymmetry in the width of radial flow in versus out, and the point of maximum M_z is not centered within the area circumscribed by the domain wall.

Figure 4.25 shows a histogram of α values along the contour paths of each of the antiskyrmions. Regions where $\frac{\pi}{2} < \alpha < \frac{3\pi}{2}$, shaded blue, indicate an outward direction of magnetization relative to the contour center. Regions where $0 < \alpha < \frac{\pi}{2}$ and $\frac{3\pi}{2} < \alpha < 2\pi$, shaded red, indicate an inward direction of magnetization.

In both cases the majority of radially outward magnetization were found pointing just outside of the Bloch sections of the domain walls. Roughly twice as much of the circumference of the antiskyrmions had magnetization pointing outward as inward.

In Figure 4.8, the point of maximum M_z was found to be ~60% of the distance from the centroid to the domain wall; for Figure 4.9, the point of maximum M_z was around ~50% of the distance fro the centroid to the domain wall. In both cases the slope of decreasing M_z was shallowest toward the center, dropping more rapidly out toward the closest wall.

Both of these observations were of interest to our fabrication collaborators. While not yet examined in detail, the working theory is that some asymmetry within the bulk stabilizes the off-center maximum M_z. The same mechanism might also be responsible for the uneven flow directions, as the largest outflow regions are opposite the high M_z locations.
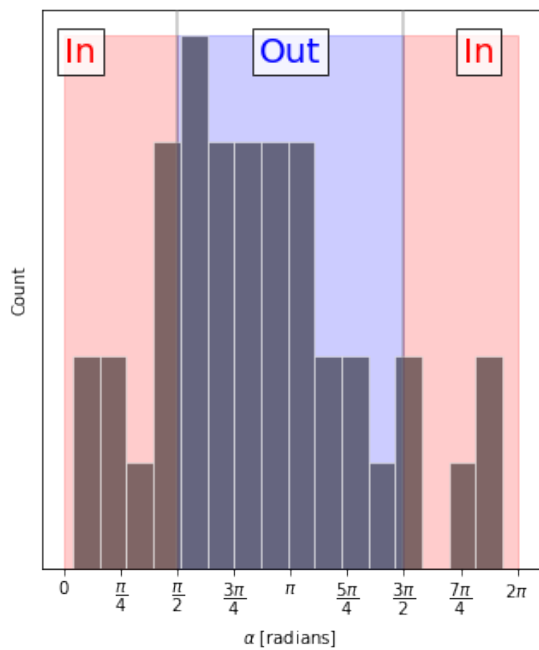
(a) Magnetization orientations for Antiskyrmion 9.
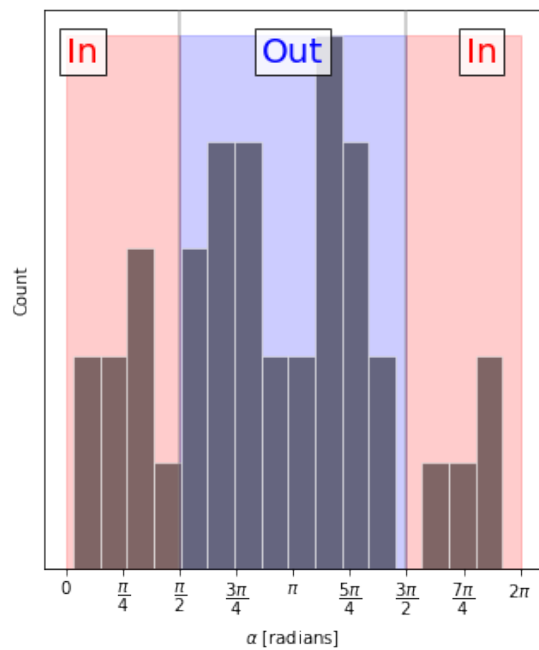
(b) Magnetization orientations for Antiskyrmion 12.

Figure 4.25. Comparison of antiskyrmion magnetization orientations.

Of the 31 circular features found, 2 were topologically trivial bubbles, shown above in Figures 4.10 and 4.11. The remaining 30 features were worms, 2 of which are shown above in Figures 4.12 and 4.13.

Figure 4.11 differs from the standard theoretical model of bubbles shown in Figure 1.6 in that the walls to either side of the inward pointing magnetization are predominantly Néel in character, flowing significantly outward for the majority of the circumference of the feature. Figure 4.10 is closer to the model but also shows considerable outward pointing magnetization along the sides adjacent the inward pointing magnetization.

The worm domains predominantly appear to be precursors to two or more skyrmions (had a slightly higher external field been applied to the sample: this has been observed real-time while nucleating skyrmions using LTEM). This is particularly evident in Figure 4.13, where a second local maximum in M_z is visible to the top right of the texture. Several of the other worm domains visible in Figure 4.1 have narrower waists than ends, indicating where they would separate into skyrmions, antiskyrmions, or trivial bubbles in a higher external field.

Interestingly, many of the worm domains showed α measurements very similar to skyrmions. When imaged using a TEM, worms, like skyrmions, generally show Bloch walls with no contrast in the center. In Figures 4.26 and 4.27 the domain walls are again a hybrid Néel/Bloch structure. As above, the lines of magnetization apparently wrap around the domain wall in a more complex shape than the TEM would indicate.

Skyrmions are, ultimately, shrunken worm domains. Their sizes, though somewhat variable, place a lower limit on the size of a worm domain.
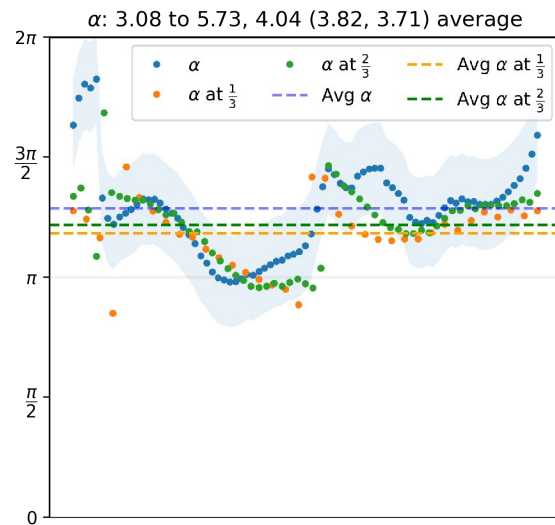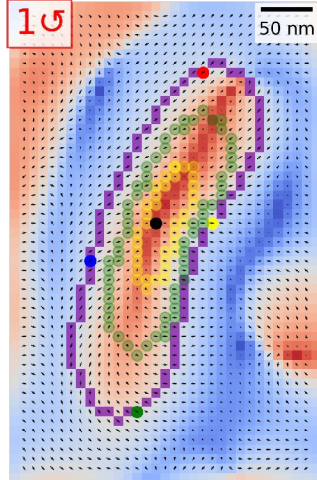
Figure 4.26. A worm with a hybrid Néel/Bloch domain wall configuration.
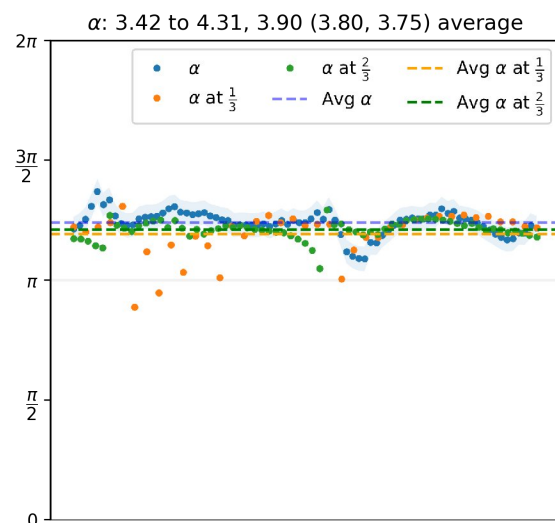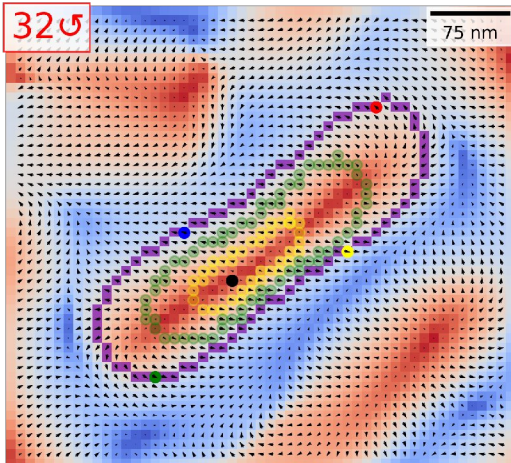
Figure 4.27. Another hybrid Néel/Bloch worm.

As expected[25, 78], the groups of skyrmions (including the 2 antiskyrmions in the first figure) shown in Figures 4.14 and 4.15 are fairly evenly spaced.

In the overview shown in Figure 4.1, it is apparent on a larger scale that several worm domains near circular features were on the verge of pinching off and forming more hexagonal arrays: features 15 and 16, as well as 18 and 24 are good examples.

The chirality of the textures tend to group, suggesting these smaller features originated from larger stripe or labyrinth domains. In the case of Fe/Gd, there is no preference for chirality expected. Recent research by another member of the group has shown via TEM that the inclusion of Pt and/or Ir layers can force a preferred chirality on the film as a whole.

CHAPTER V

CONCLUSION

Dissertation Results

This dissertation has detailed the background and observation of a variety of magnetic structures found in Fe/Gd multilayer thin films through a combination of technologies, particularly SEMPA and Lorentz TEM. This analysis required the development of new software tools to process the data output by the SEMPA, as well as detect and characterize textures found in the films.

The results of this analysis revealed a zoology of chiral spin textures found in $Fe_{0.34}/Gd_{0.40}$ x 120 layers including skyrmions, antiskyrmions, trivial bubbles, and worms. When coupled with 2D projection images from LTEM, the ability of the SEMPA to capture spin polarization (and, by extension, magnetization) information enabled the discovery of a morphology with greater complexity than previously expected for skyrmions and worms, providing a more complete answer to the question: what is the 3 dimensional structure of these objects?

For Skyrmions and Bubbles and Worms, this analysis found that the Bloch walls observed in Lorentz TEM do not extend to the surface, where instead Néel walls were observed. The gradual transition from Néel to Bloch indicates a non-trivial topology in three dimensions, not two; something closer to a twisted vortex state (perhaps hopfion, depending on definition) for the magnetization, wrapping around barrel-shaped walls not in circles but helices, much like a Slinky coiled back on itself. The description of skyrmions as "cylindrical Bloch wall domains" is demonstrably overly simplistic: hybrid Néel/Bloch domains that appear to extend some distance into the bulk are a more accurate description.

For Antiskyrmions, this research found two asymmetries, in location of maximum M_z in the texture as well as the portion of the texture pointing in versus out.

Implications and the Future

Much remains to be learned about the characteristics of skyrmions and related textures. A complicating factor is that several of these characteristics are tunable; *e.g.*, while $Fe_{0.34}/Gd_{0.40}$ x 120 layers stabilizes skyrmions at room temperature, $Fe_{0.34}/Gd_{0.40}$ x 80 layers does not. Similarly, Fe/Gd has no preferred chirality, but Fe/Gd/Pt/Ir does.

A fundamental part of spintronics is creating and moving skyrmions. Both of these activities are influenced by the shape of the skyrmions being manipulated.

The SEMPA holds the potential to answer these questions and provide insight about different magnetic structures in materials of varied sizes and textures. Through this work the instrument was made operational and its capabilities exercised to analyze Fe/Gd, increasing our knowledge of the nature of skyrmions.

APPENDICES

APPENDIX A

PYNISTVIEW

The code developed by the author for this work is available on Github.

APPENDIX B

SEMPA MANUAL

SEMPA: The Missing Manual

Rich Moraski

January 5, 2023

Contents

List of Figures

List of Tables

Chapter 1

Introduction

This document is meant to be a guide for anyone using the Scanning Electron Microscopy with Polarization Analysis (SEMPA), whether for standard scanning electron microscope (SEM) imaging or more complex surface magnetization imaging.

The SEMPA instrument is based on a modified JEOL JAMP-7830F Field Emission Auger Microprobe. The base instrument, which includes a standard SEM, specializes in capturing Auger spectra of materials. The nature of Auger analysis requires relatively high vacuum levels. Being able to determine surface composition in ultra high vacuum provides a good starting platform for surface magnetization analysis.

Some JAMP-7830F specs:

- Accelerating voltage from 500 eV to 25 keV

- Probe current from 10 pA to 100 nA

- Main chamber pressure down to 3×10^{-8} Pa

- Sample sizes up to 12 mm wide by 5 mm thick

- Stage movement of ±10 mm in X and Y, 6 mm in Z

The instrument was built at NIST in Germantown, MD, in the early 2000's. It was the third iteration of such a device.

In 2017, John Unguris, one of the original builders of the system, retired. The SEMPA project was retired with him. Instead of putting the disassembled instrument into storage, on January 24, 2018, the SEMPA was donated to the University of Oregon. It has been located in the Micro Analytical Facility, Room 87, CAM-COR, since.

Chapter 2

Concept of Operation

SEMPA is a heavily modified JEOL JAMP-7830F Auger microprobe. This base platform was chosen as Auger analysis (electron energy spectroscopy for characterizing material composition) is both necessary for ensuring a clean surface and dependent on an ultra high vacuum system (1×10^{-8} Pa), both requirements of SEMPA, an inherently inefficient technique.

A unique feature of this microscope is the inclusion of quarter sphere in the center of the SEMPA column that permits viewing in X-Y and X-Z, thus allowing a 3 dimensional reconstruction of the surface magnetization. A cartoon model of the instrument is shown in Figure 2.1.

Probe electrons incident on a tilted magnetic sample eject spin–polarized secondary electrons from the top nanometer or so of the surface. These electrons scatter from the sample up and right through the column to one of two detectors: the dark block (the quarter sphere) in the center of the column either allows the electrons to pass to the straight through detector at the top right (labelled "In Plane"), which captures X-Y information, or guides electrons via a voltage difference to the right-angle detector at the bottom right (labelled "Out of Plane"), which captures X-Z information. Each of the 4-channel Mott detectors, shown in Figure 2.2, resolve up, down, left, and right spin-polarizations, with net polarization

$$P = \frac{1}{S}\frac{N_+ - N_-}{N_+ + N_-},\tag{2.1}$$

where N is the number of electrons hitting one of the detectors and S is the Sherman function, a characteristic of the detector design. As magnetization is proportional to spin polarization, data collected from the X-Y plane is combined with X-Z data in software to reproduce the 3D surface magnetization.
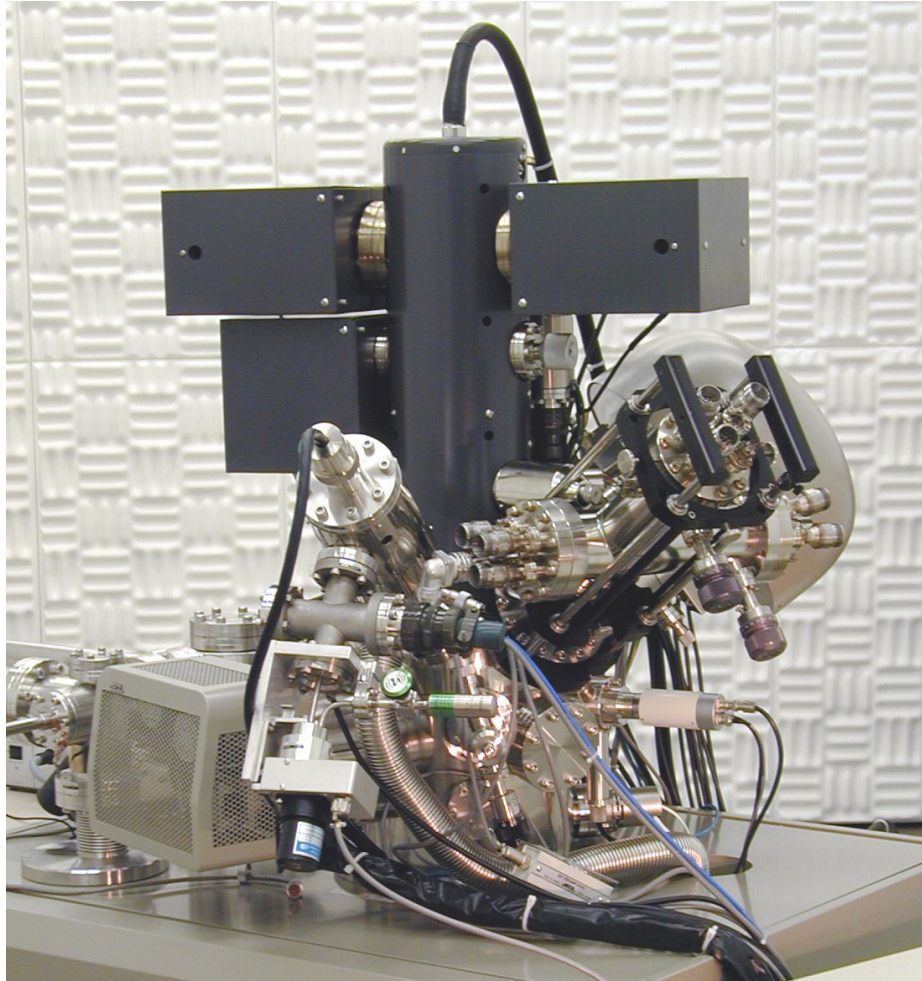
Figure 2.1. Schematic of SEMPA. After milling the sample surface clean with the ion gun, spin–polarized secondaries scattered by the incident electron beam are guided into the SEMPA column. These electrons are then Mott scattered by a gold target before being counted by a cloverleaf–shaped array of sensors. Depending on the configuration, either in-plane (X-Y) or out of plane with redundancy (X-Z) spins are examined. Figure reproduced with permission from "Scanning electron microscopy with polarization analysis (SEMPA) and its applications" by John Unguris in Experimental Methods in the Physical Sciences. Vol. 36. Elsevier, 2001, pp. 167–XVI.
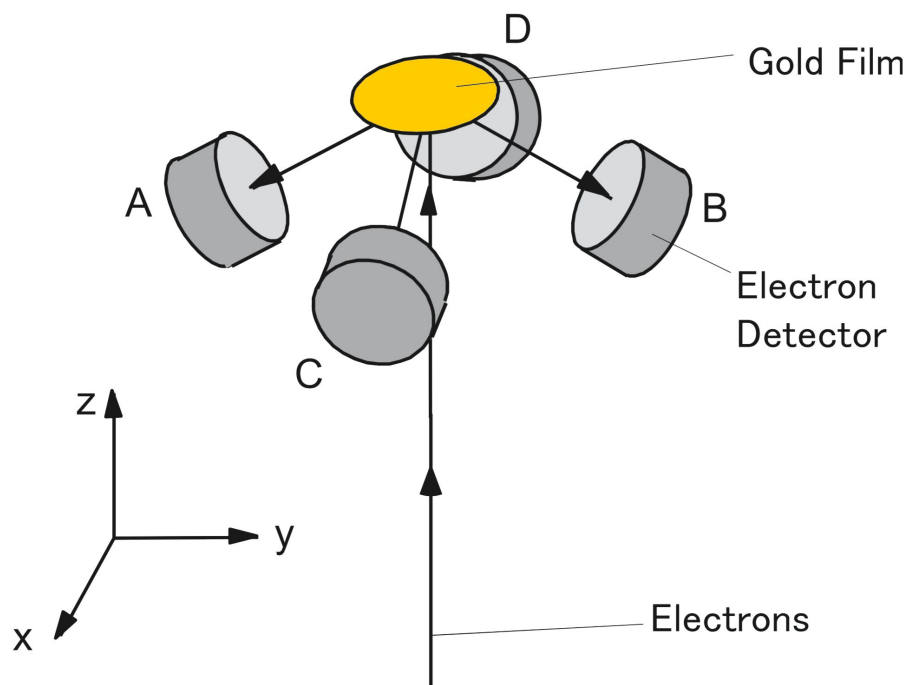
Figure 2.2. Cartoon of the Mott detector. There are 2 of these on the instrument: one for straight through operation capturing X and Y as shown, the other for right angle operation capturing X and Z. Figure reproduced with permission from "Scanning electron microscopy with polarization analysis (SEMPA) and its applications" by John Unguris in Experimental Methods in the Physical Sciences. Vol. 36. Elsevier, 2001, pp. 167–XVI.

Chapter 3

Components of the Instrument

There are many parts that make up the SEMPA, several factory parts from JEOL, several custom designed at National Institute of Standards and Technology (NIST).

3.1 Sample Exchange Chamber

Also called the 1st Airlock chamber, this is the starting point for observing samples in the instrument where samples are moved in and out of the vacuum. Pressing the EXCH VENT button during normal operation will vent the chamber to atmosphere, allowing the door to be opened and a sample holder inserted/removed: turn the black knob with the MDC logo counterclockwise until it is loose, leaving it in place until the pressure has been increased to 1 ATM: this ensures the door will not fly open, which is generally not a real concern.

There are 2 arms in this chamber: one that moves the sample from the entry point to laterally to the second, which moves the sample back to the parking chamber.

The pressure for this chamber is monitored on the Pfieffer Vacuum SIngleGauge in the rack farthest left. Normal values are in the 1×10^{-5} Pa range.
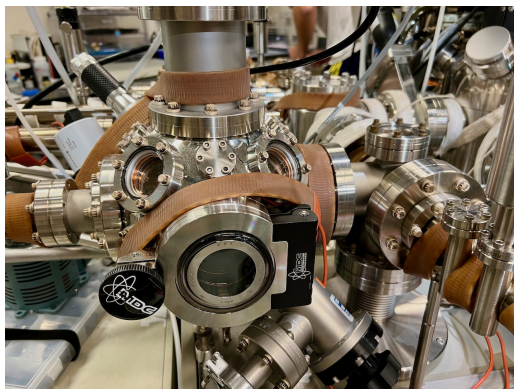
Figure 3.1. The exchange chamber

3.2 Parking Chamber

The parking chamber, located just left of the electron column, allows up to 4 sample holders to be maintained in vacuum.

There are 3 arms in this chamber: one that moves samples from the 2nd arm from the sample chamber to either the parking holder or the main chamber; one for the parking holder; and one that moves samples from the parking holder to the electromagnet.

The pressure for this chamber is monitored on the GP 307 Vacuum Gauge Controller in the rack farthest left. Normal values are in the 1×10^{-5} Pa range.
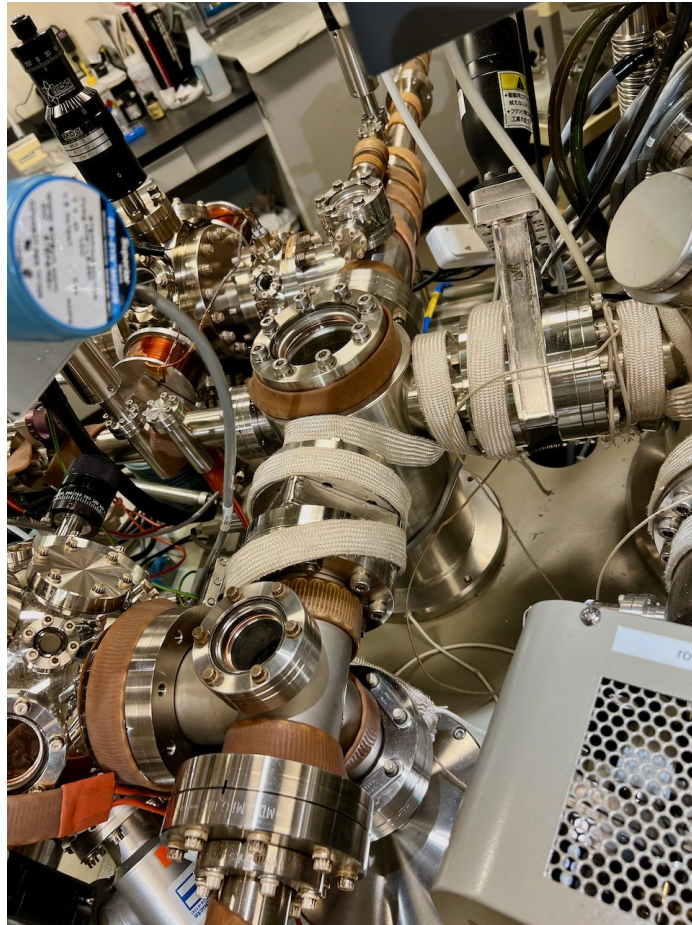
Figure 3.2. The parking chamber

3.3 Electron Column

This is where the electrons are extracted and accelerated. It is covered in mu-metal to help shield against stray magnetic fields that might otherwise disrupt Auger or SEMPA imaging. The gun is at the top, lenses and apertures in the middle, and the sample stage at the bottom.

The pressure for this chamber is monitored on the Ionivac IM520 in the 2nd rack from the left. Normal values are in the 1×10^{-7} Pa range.
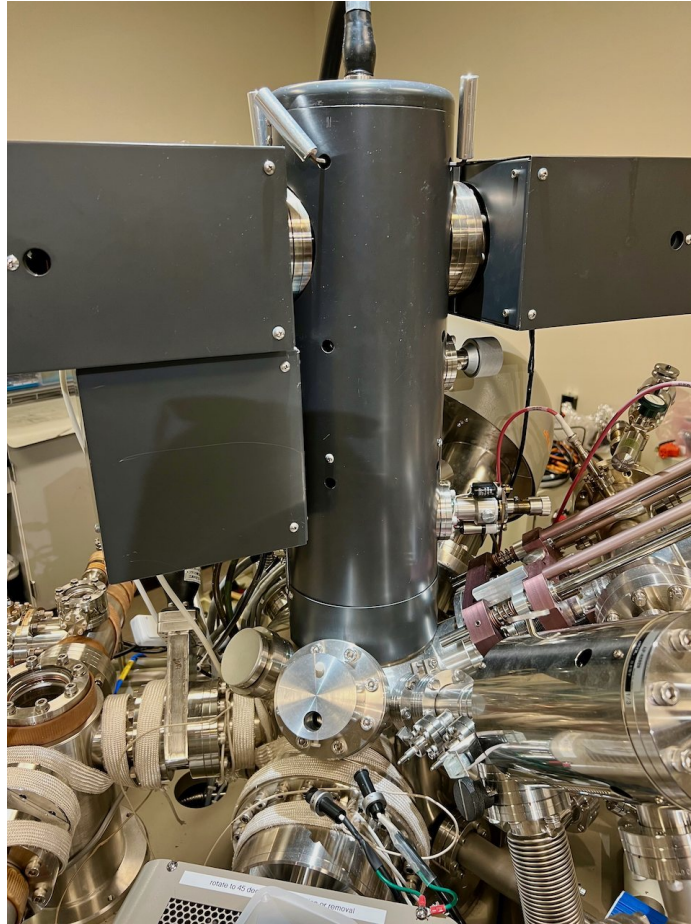
Figure 3.3. The electron column is the dark cylinder in the center of the instrument

This is a schematic view of the column.
From top to bottom, the significant components are

- Field emission gun (FEG)

- Suppressor

- Extractor

- Gun alignment coils

- C1 stigmator coils

- C1 condenser lens

- C2 stigmator coils

- C2 condenser lens

- Probe current detector (PCD)

- Scan coils

- OL stigmator coils

- Gun shift coils

- OL objective lens

- OL alignment coils

- Stage
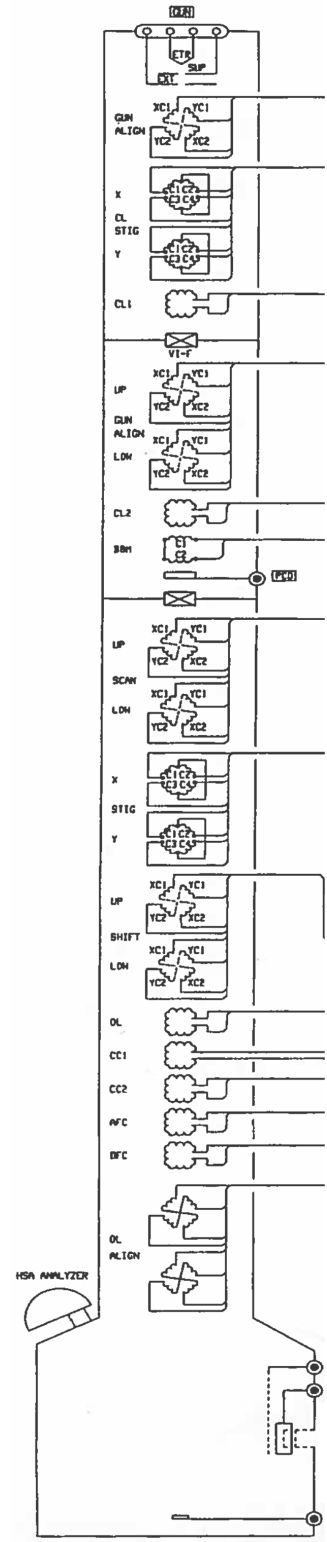
Figure 3.4. Schematic of the electron column

106

3.3.1 Field emission gun (FEG)

The FEG sits at the top of the column. It is a thermally-assisted Schottky field emitter that provides the electrons that are accelerated down toward the sample. A small tip is heated to ~1,800 K while in a 3,000 V extraction field. The emitted electrons are funneled down to the chamber aperture by the 300 V suppressor field.

The pressure for this chamber is monitored on the FEG Ionization Gauge at the top of the 2nd rack from the left. Normal values are in the 1×10^{-7} Pa range.

(a) The FEG holder
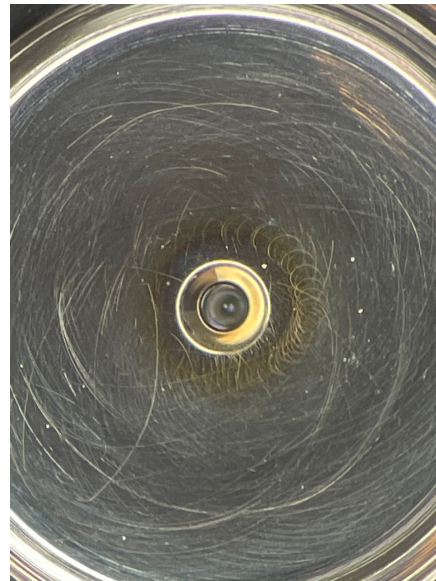
(b) The FEG viewed from above

Figure 3.5. field emission gun

Figure 3.6. The pressure in the FEG is shown on the top gauge; units are Pa

Replacement tips are available from Ted Pella. The part number is TFE174C SE4; as of 2021, the price per tip was $5,550.
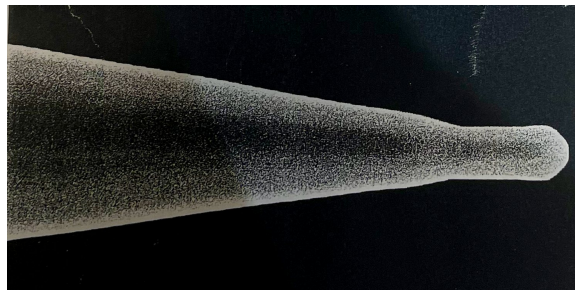
Figure 3.7. Magnified image of the FEG from the side

3.3.2 Sputter ion pumps (SIPs)

The sputter ion pumps (SIPs) are ion pumps meant to operate in high vacuum (1×10^{-5} Pa or lower). There are 5 total: one for the specimen analyzing chamber (SIP 1), one for the lenses (SIP 2), one for the parking chamber (SIP 3, underneath the main instrument), and a pair for the FEG chamber (SIP 4).

These are consumable items.

Figure 3.8. 3 of the 5 SIPs are visible as grey boxes on the sides of the electron column

Figure 3.9. The currents for SIP 1 and 4 are shown on the fourth and second gauges, respectively

3.3.3 Condenser and objective lenses

These are located in the main column. They are responsible for shaping (condenser) and focusing (objective) the electron beam ultimately into a probe at the sample. There are 2 condenser lenses and one objective lens in the SEMPA.

3.3.4 Aperture

The aperture is a small strip with 4 same-sized relatively large holes in it that holds a thin film with 4 different-sized smaller holes. The aperture assists with beam shaping and blocks electrons that stray too far from the desired beam path.

The aperture is controlled from `Auger Master > Observation > Probe Condition > OL > Aperture`. 5 removes the strip from the beam path (no aperture); 4–1 are successively smaller apertures. A larger aperture permits more current at the cost of reduced resolution; a smaller aperture allows a sharper image at a reduced current. For regular SEM imaging, ~1 nA provides a very sharp image. This might be too low a current for the rather inefficient SEMPA imaging, however.
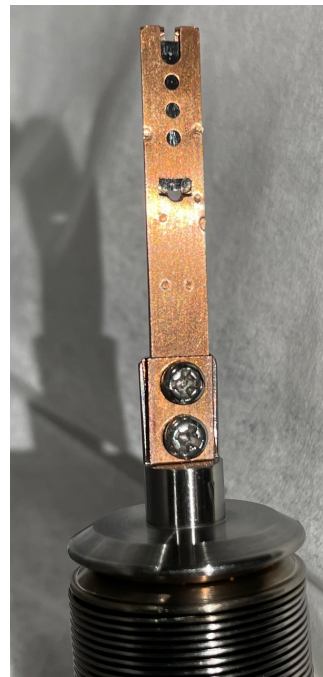
(a) The aperture removed from the instrument

(b) Close-up of the aperture holder; the aperture strip is the dark insert at the top behind the holes

Figure 3.10. Aperture

3.3.5 Specimen Analyzing Chamber

Located at the bottom of the electron column, this is where the sample resides during imaging.

Figure 3.11. A view into the main chamber. The objective lens is the triangle at the top; the SEMPA input optics are the copper colored bit right center; and the Micro Ion Etching Device (MIED) is darker silver cylinder to the right.

Figure 3.12. The pressure gauge for the main chamber; units are Pa
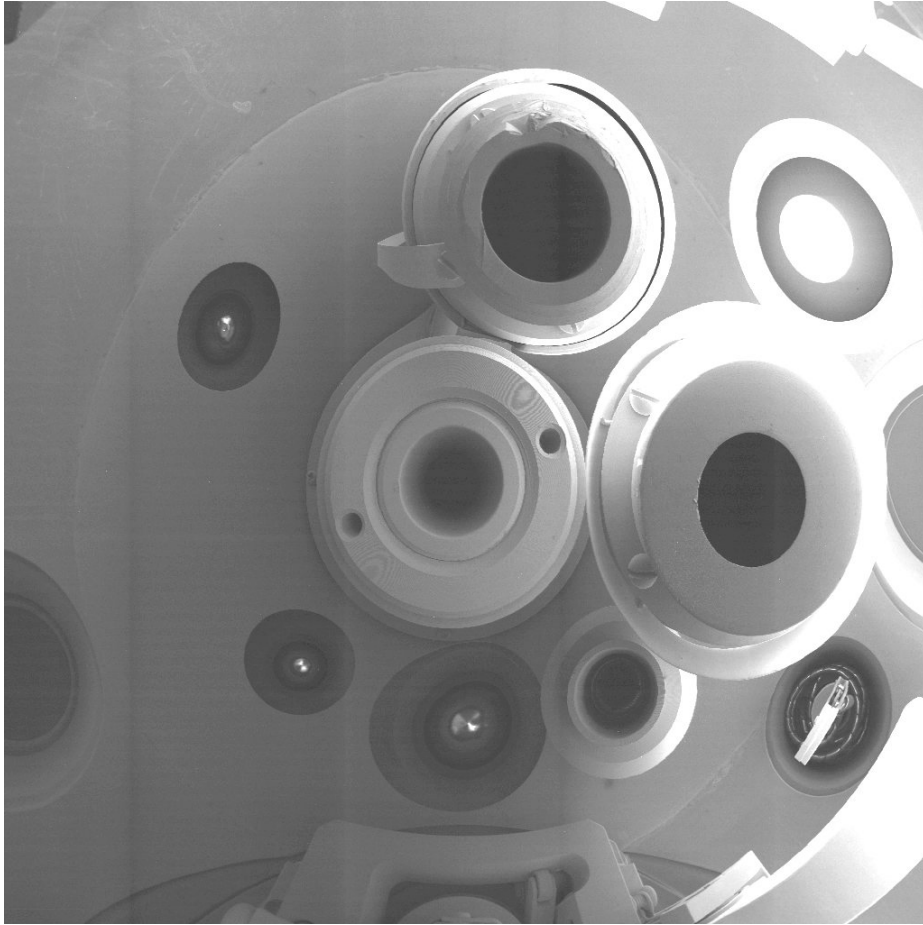
Figure 3.13. A view looking up from inside the main chamber up at the instrument

3.3.6 Stage

The stage holds the sample holder and allows for it to be translated, raised, lowered, tilted, and rotated. The stage is grounded to the chassis. There are special sample holders that allow for up to 7 electrical connections via a feed-through on the left side of the stage housing. There is also a BNC connector on the side that allows measuring the current exiting through the stage.

The smallest units in `Auger Master` are μm; *e.g.,* x = 1.234 is 1.234 mm.
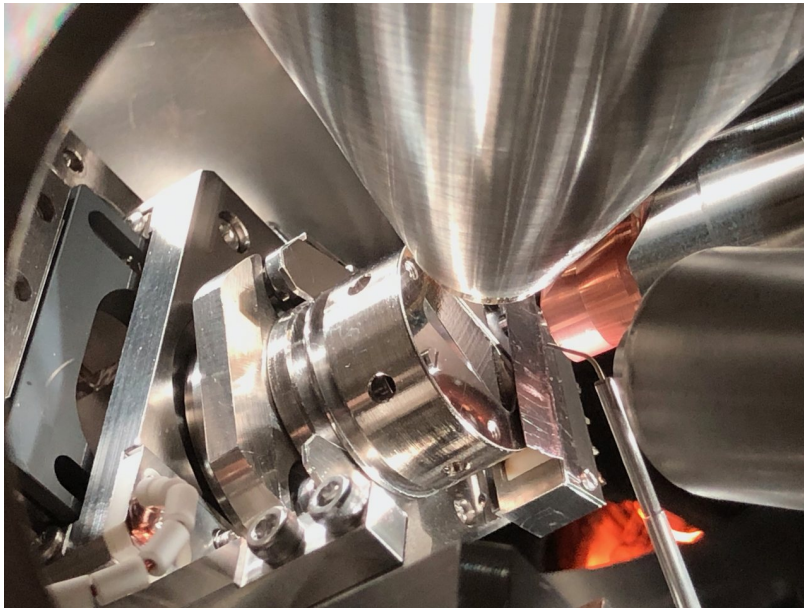
Figure 3.14. The stage is visible 45° down and to the left of the sample holder

3.4   Auger electron spectrometer (AES)

The Auger detector is the original reason for this instrument. It uses low energy secondary electrons, namely Auger electrons, that are scattered from very near the surface of the sample (within the top 1 nm or so) to determine the composition of the surface.
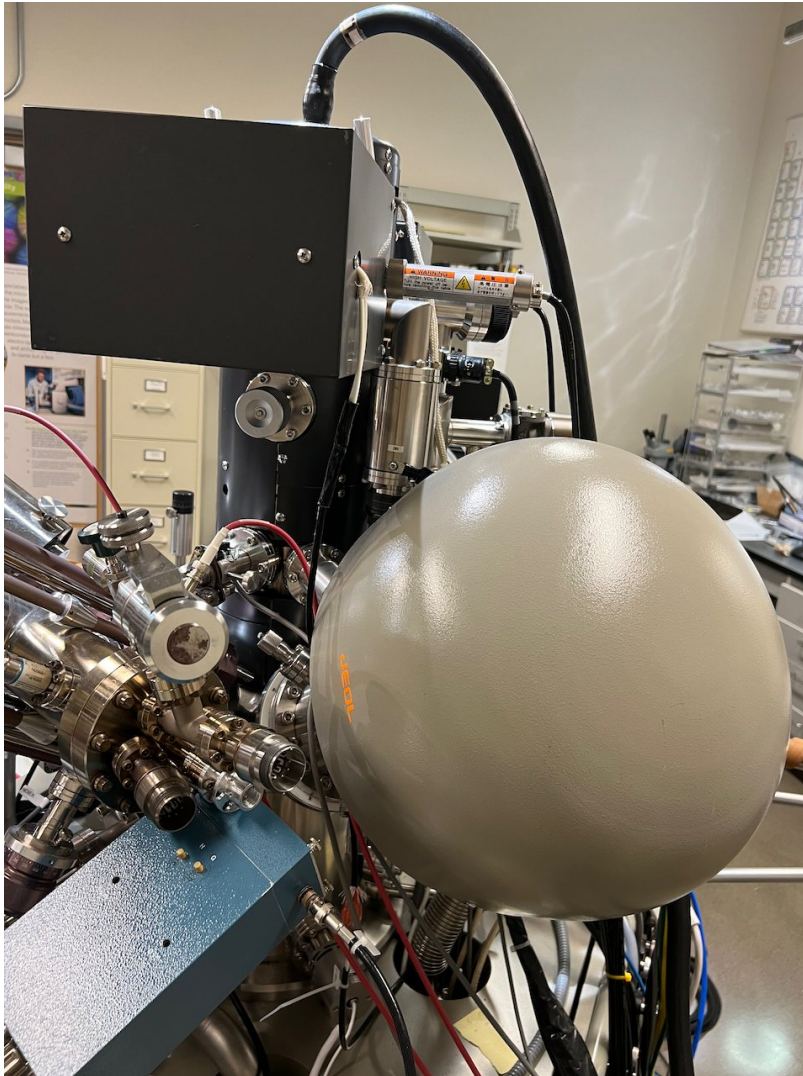
Figure 3.15. The AES is the hemispherical dome to the right, behind the main column in the lab

3.5   Micro Ion Etching Device (MIED)

The MIED, or simply ion gun, uses ionized Ar gas to abrade the surface of the sample, like a (much) gentler version of sandblasting. This is useful for removing oxidation, capping layers, and other contaminants.
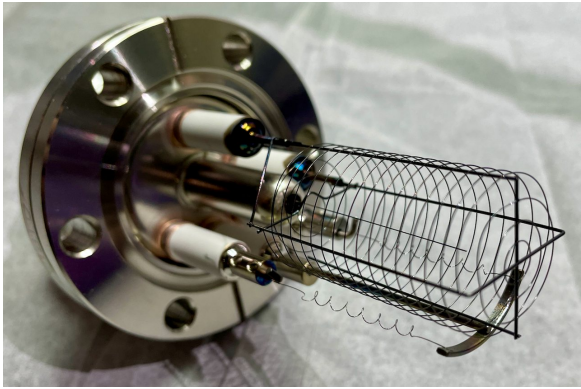
(a) The MIED removed from the instrument

(b) The control panels for the MIED

Figure 3.16. Micro Ion Etching Device (MIED)

The two green fuses just right of center in Figure 3.17 tend to blow.
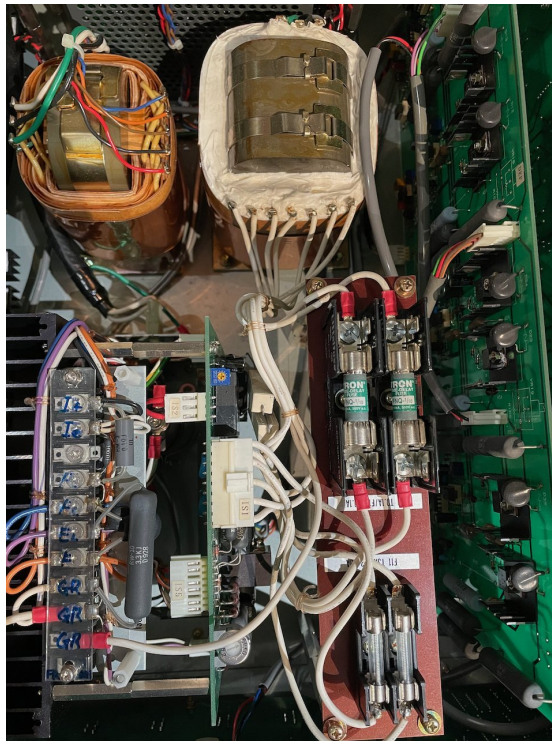
Figure 3.17. The circuitry for the MIED

3.6   Everhart-Thornley detector (E-T detector)

Everhart-Thornley detectors (E-T detectors) are the parts responsible for constructing the SEM contrast. As the SEM beam rasters across the sample, secondary electrons are pulled toward the +10,000 V biased cap around the front of the E-T detector. There they collide with a layer of phosphorus, where the photoelectric effect causes photons to be released. These photons travel down a clear glass light pipe where they hit a photomultiplier that amplifies the signal. The imaging circuitry descans the signal and builds the image shown on the screen.

These are consumable (though renewable) items: over time the phosphor coating will get blasted away by the incoming electrons.
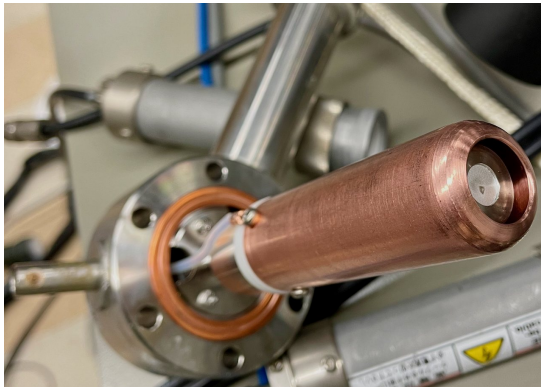
(a) Light pipe removed from the instrument   **(b)** Light pipe with the copper shield removed
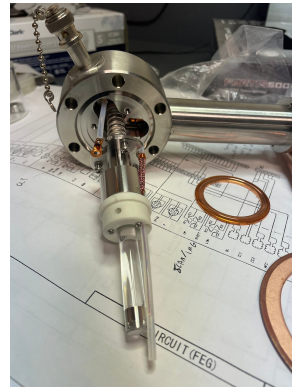
Figure 3.18. Light pipes

The E-T detector switch, shown in Figure 3.19, selects between the "normal" detector (for standard imaging) and the 2 detectors attached to the SEMPA column.
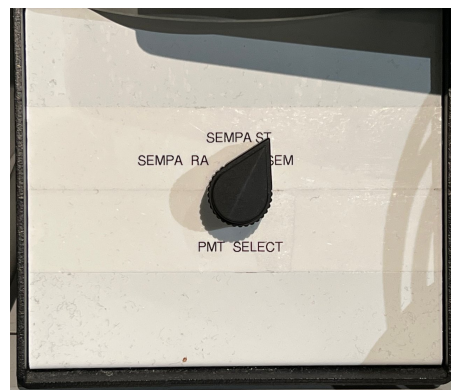
Figure 3.19. E-T detector selector switch

3.7 Electromagnet

The electromagnet allows for in-vacuum application of magnetic fields. It relies on a separate current supply to generate a field. Table 10.1 shows the fields measured between the yoke and one of the coils at specified currents (the field increases linearly with current); Table 10.2 extrapolates this to specific field strengths.
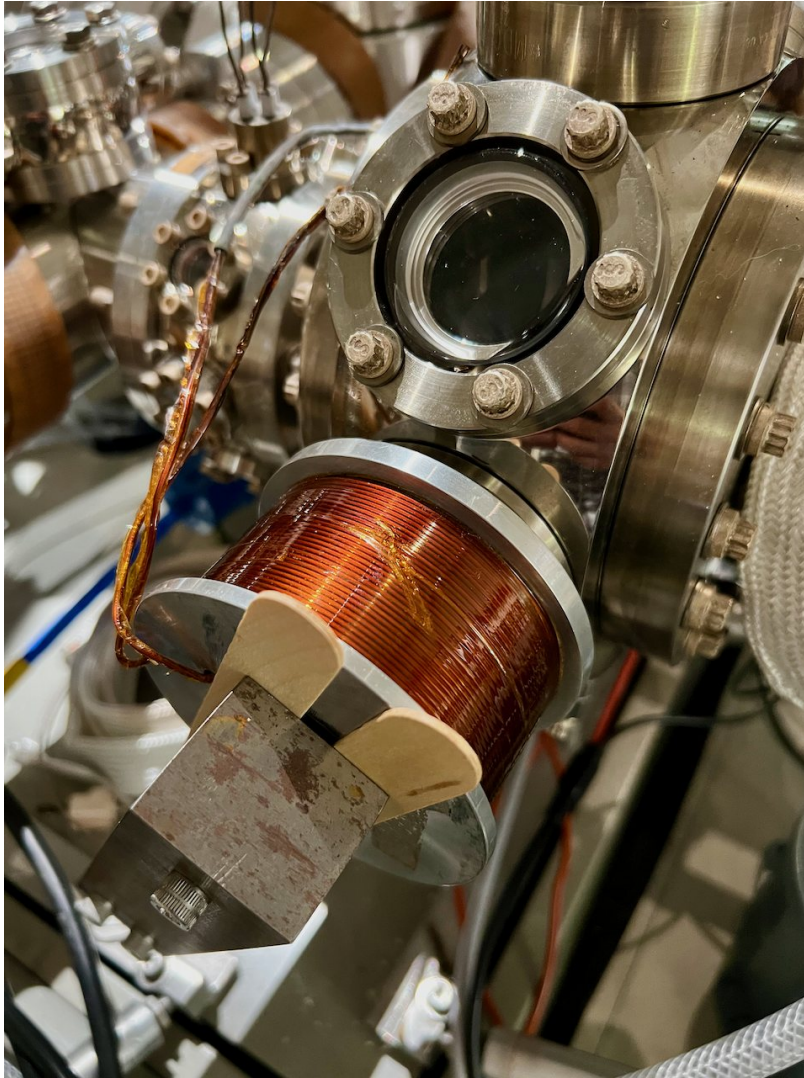
Figure 3.20. The electromagnet, shown here with 2 wooden sticks providing space between the yoke and coil to measure the field strength

3.8 Plasma Gun

The plasma gun, located atop the sample exchange chamber, can be used to clean samples with a low energy Ar plasma. It is currently configured to operate on Ar but has been used in the past with other gases.

There is a pump and water container in the service chaise that must provide cooling for the gun when in use. The pump must be started and stopped manually. The water lines to the gun need to be removed during bakeouts.
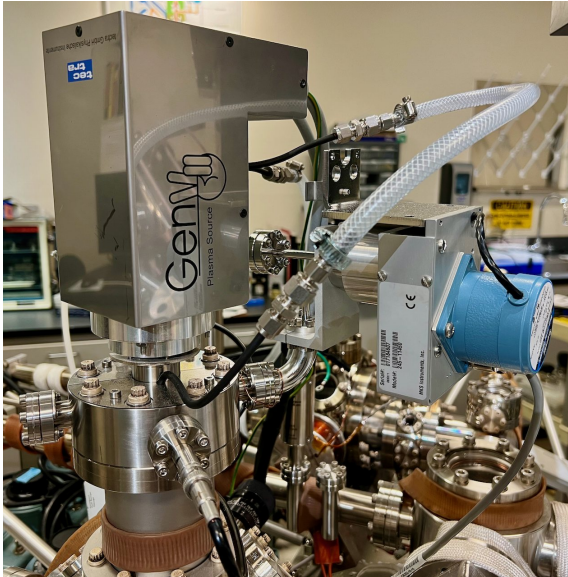
(a) The plasma gun for gentle milling of the entire sample

(b) The plasma cage

Figure 3.21. Plasma gun

3.9   Console

This is the main work area. There is one keyboard and mouse shared across 3 computers. There are 6 monitors; starting top left and proceeding clockwise: camera image, doorbell, bracket, 2 monitors for whisk, and the SEM image. The stage and optics controls are also here, along with sample chamber light power supply, Kleindiek arm controls, HT wobbler, E-T detector switch, printer, and external scan controller.

The 4 main power switches and MIED controls are underneath on the left. The bigger area underneath on the right holds

Figure 3.22. The console

3.10   Printer

The printer produces small (roughly 4 inches square) printouts of the SEM image.

Figure 3.23. The printer for SEM images

3.11   Auxiliary pump

The Pfieffer pump in front of the sample exchange chamber is used to supplement the turbo molecular pump (TMP) initially when pumping down. It displays units in mbar.

Figure 3.24. The auxiliary pump

3.12   Turbo pump

The turbo pump is most effective at higher pressures (down to $\sim 1 \times 10^{-5}$ Pa) than the SIPs. The pump itself is under the microscope; the controls for it are behind the instrument.

Figure 3.25. The turbo pump controls at the back of the room

3.13   High tension tank

The HT tank provides 30 kV to the FEG. The tank contains, among other things, a Cockroft-Walton voltage multiplier bathed in SF_6 to help minimize the risk of arcing. There is a gauge on the side of the tank with a marking indicating the correct pressure for the gas. Care must be taken when working with SF_6 as it can be toxic.
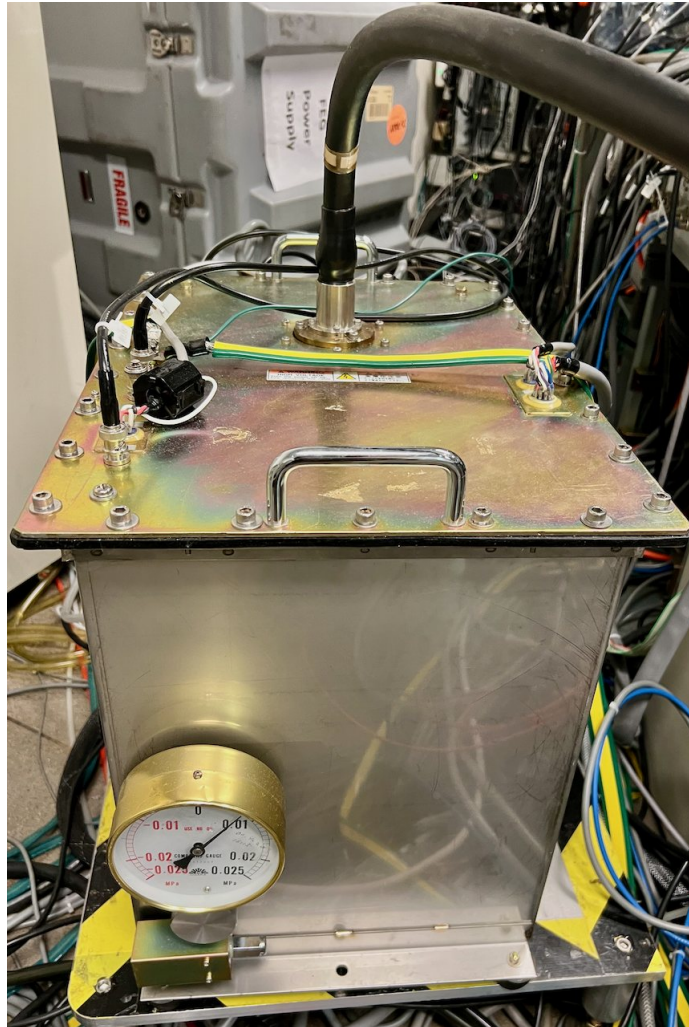
Figure 3.26. The high tension tank that provides up to 30,000 V

3.14   Vacuum system

Below is a schematic view from the JEOL manual of the vacuum system showing chamber, valves, and pumps.
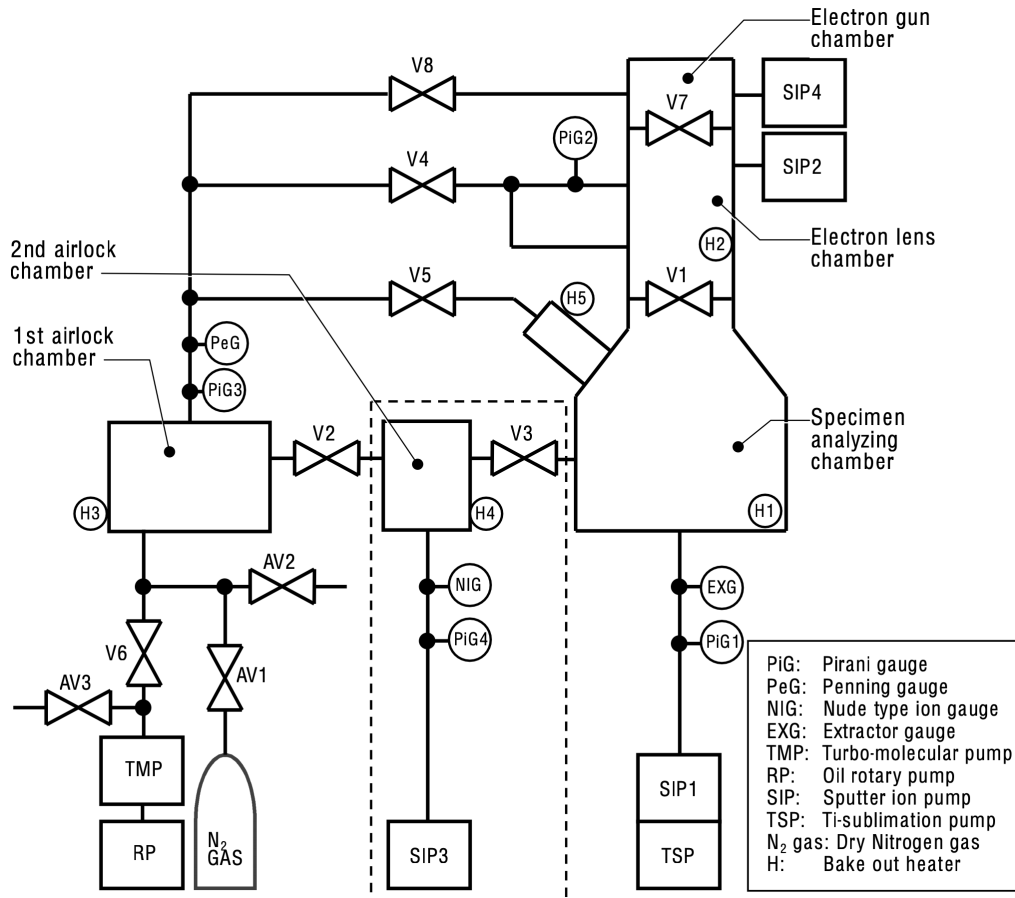
Figure 3.27. Schematic of the vacuum system

3.15 SEMPA Column

This is the reason we're here. The SEMPA column juts up at an angle from the specimen analyzing chamber. It is designed to move in and out slightly (the input optics need to be about 1 cm from the sample, but they need to be protected from being hit while moving the sample); 2 aluminum spacers are used to hold it in place.

The biggest thing that makes the SEMPA unique is its ability to measure all 3 components of magnetization, thus allowing for reconstructing the 3D magnetization at the surface of the sample. This is accomplished by having 2 detectors: one straight through (ST) and one right angle (RA). In both cases gold targets at the ends of the columns are used to Mott scatter the incoming polarized electrons to a 4 quadrant detector that measures either X and Y (ST) or X and Z (RA).
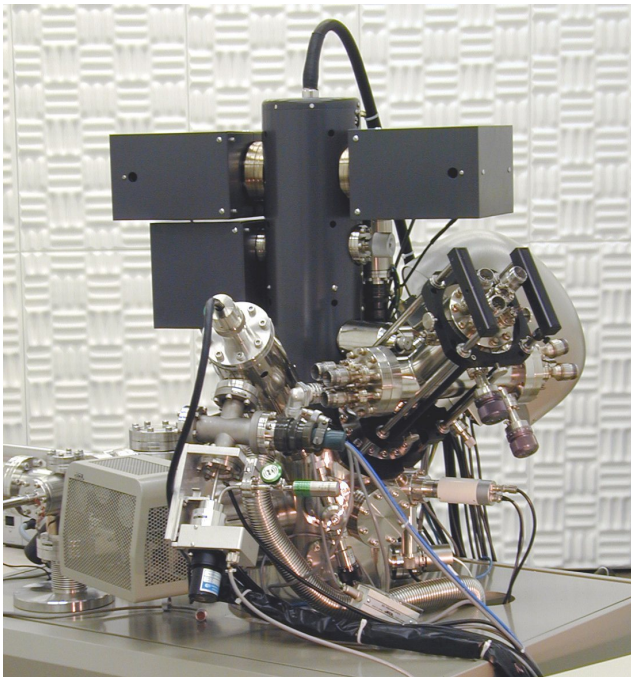
(a) The SEMPA column is the silver part diagonally up on the right

(b) The SEMPA rack on the right

Figure 3.28. SEMPA

Inside the vacuum chambers are a number of electostatic lenses (the copper tubes in Figure 3.29 are several) leading to the detectors at the ends. These are held at different voltages controlled by the knob box (Figure 3.35a).
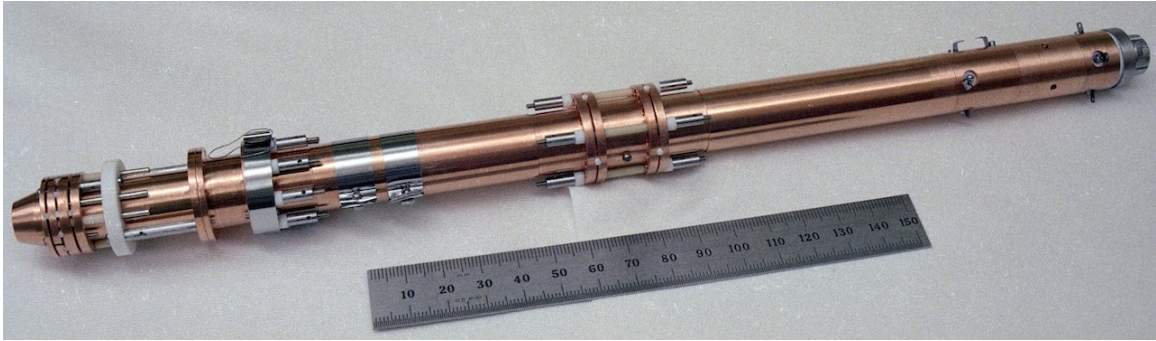
Figure 3.29. The first sections of the SEMPA column (E1–E7, see Figure 3.32 below)

In the center of the column is the switchyard which houses a quarter sphere configured to either have the same voltage on all parts (for ST) or different voltages on the inside versus outside (for RA). In the RA case, the electric part of the Lorentz force redirects the electrons to the RA detector at the back of the instrument.
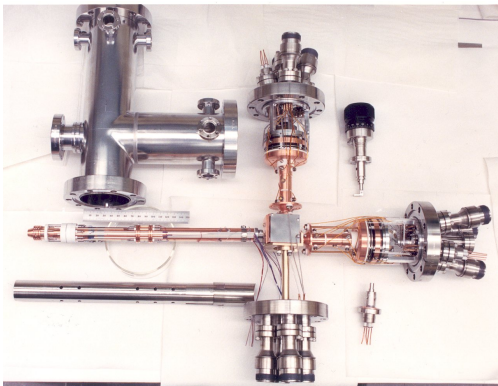
(a) An exploded view with ST to the right, RA on top, the input optic on the left, and the switchyard on the bottom
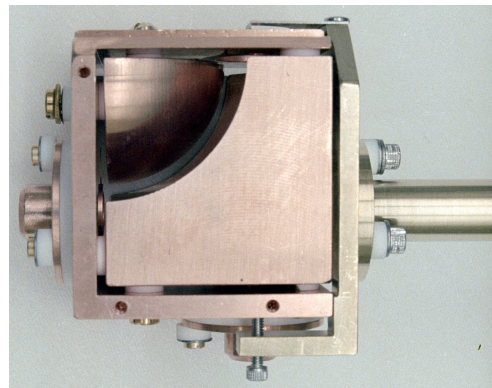
(b) The quarter sphere used to redirect the beam to the RA detector (toward the top in this image)

Figure 3.30. More SEMPA
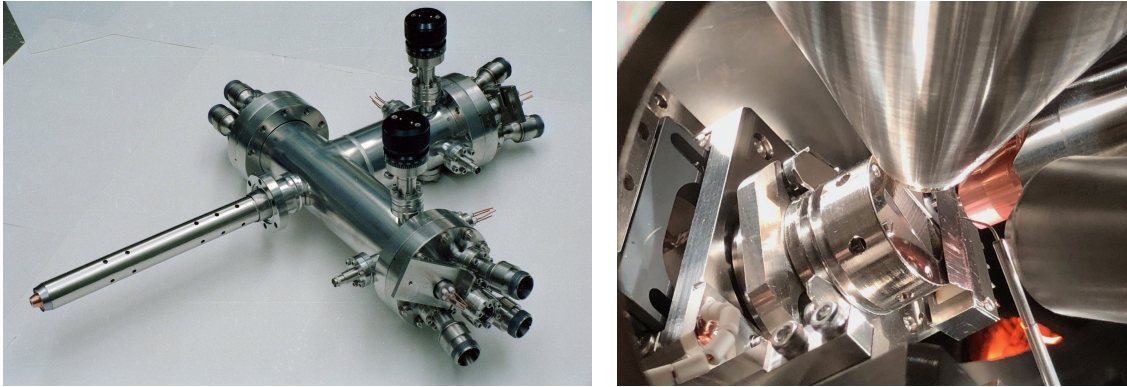
(a) The complete SEMPA assembly removed

(b) The SEMPA input optic is the copper piece at 2 o'clock

Figure 3.31. Still more SEMPA

Figure 3.32 shows a schematic of the optics and Mott detectors.
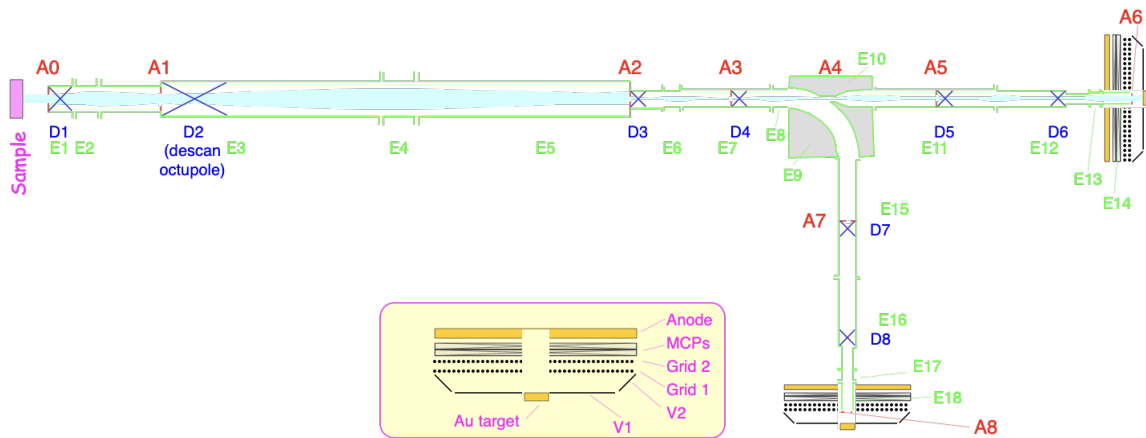
Figure 3.32. Schematic of the ST optics
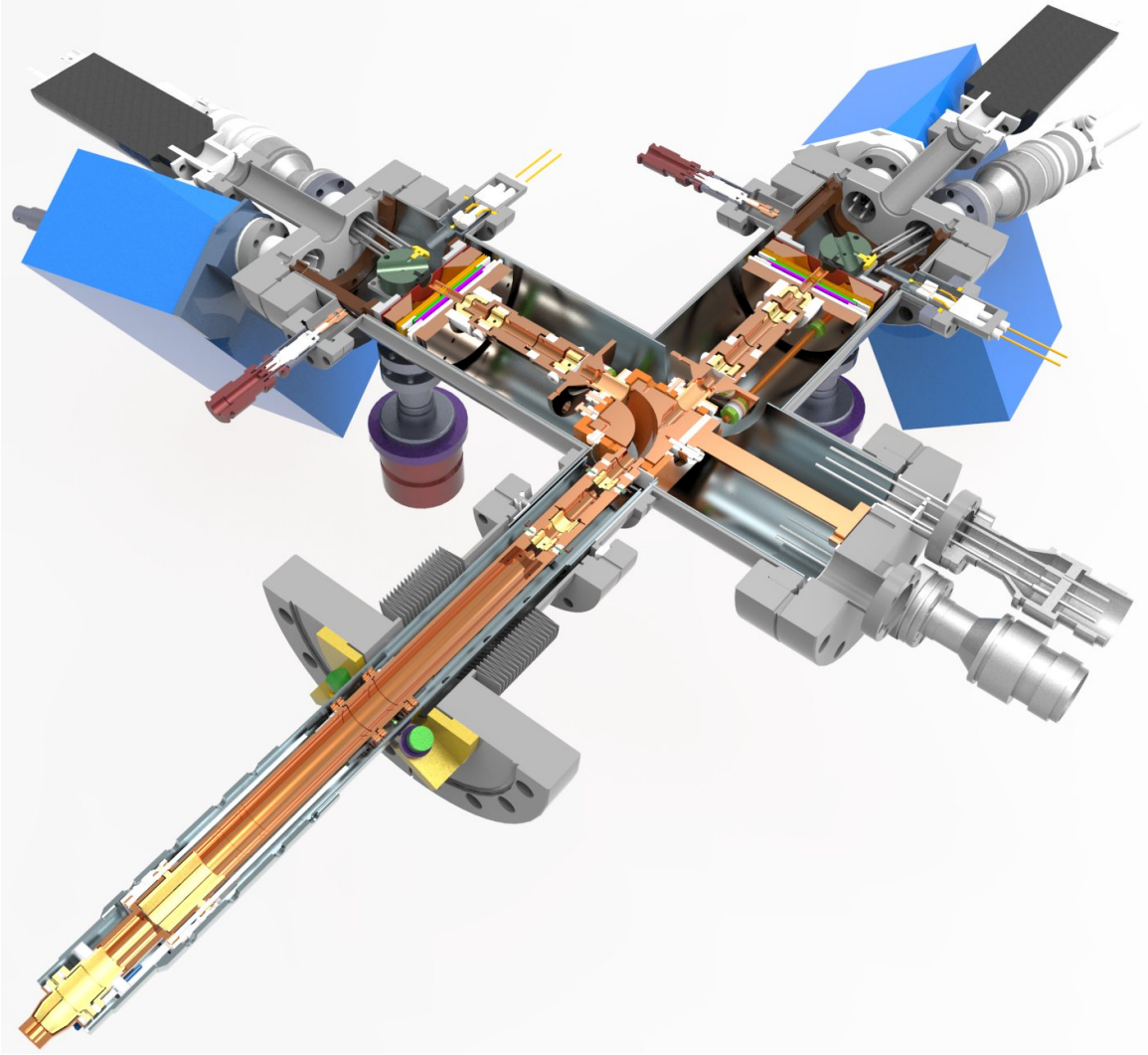
Figure 3.33. A cutaway of the complete ST column

3.16   SEMPA Rack

The rack shown in Figure 3.34 houses the electronics that control voltages throughout the SEMPA. The top three instruments are meters intended to assist with aligning the beam in the system; alignment by eye using the E-T detector detector for each arm is easier and less error-prone.

Figure 3.34. The SEMPA rack

The knob box, shown in Figure 3.35, adjusts the voltage for the electrostatic lenses (knobs labeled with E's) and deflectors (knobs labeled with D's). The first 4 lenses, namely E1-4, are the most frequently adjusted.

(a) The SEMPA knob box   **(b)** The knob box circuitry

Figure 3.35. The knob box

4 cables from the knob box, namely O1-O4, connect to the 4 inputs on the switchyard, namely I-IV. The pinouts are represented in Figure 3.36.

Knob Box Pinouts

Pin	O1			O2			O3			O4		
	Destination	SYD	Voltage	Destination	SYD	Voltage	Destination	ST	Voltage	Destination	RA	Voltage
A				D1 R	III g	± 125	D6 L	III h	± 58	D8 L	III h	± 58
B				D4 B	IV f	± 57.5	D6 R	III f	± 58	D8 R	III f	± 58
C				D4 T	IV e	± 57.5	D6 T	III j	± 58	D8 T	III j	± 58
D				D4 R	IV g	± 57.5	D6 B	III g	± 58	D8 B	III g	± 58
E				D4 L	IV h	± 57.5	E14	III a	141 ± 32	E18	III a	141 ± 32
F				Bertran (N/A)		(N/A)						
G				D3 B	IV b	± 150	E12	III l	358 ± 58	E16	III l	358 ± 58
H							E13	I g	500 ± 100	E17	I g	500 ± 100
J	E8	I l	340 or 1496	E2	III c	550 ± 60						
K	E10	I b	340 or 961	E4	III d	713 ±66.5						
L				E6	III e	384 ± 90						
M				Bertran (N/A)		(N/A)						
N	D2A, D2H	II a, h	± 75	D1 L	III h	± 125						
P	E3	II l	1496 ± 30	E5, E7	III j	1496 ± 30	E11	I b	1496 ± 30	E15	I b	1496 ± 30
R				D3 L	IV d	± 150	D5 L	I h	± 57.5	D7 L	I h	± 57.5
S	D2B, D2C	II b, c	± 75	D3 T	IV a	± 150	D5 T	I j	± 57.5	D7 T	I j	± 57.5
T	D2F, D2G	II f, g	± 75	D3 R	IV c	± 150	D5 R	I l	± 57.5	D7 R	I l	± 57.5
U	D2D, D2E	II d, e	± 75	D1 T	III a	± 125						
V	E9	I j	340 or 2243	D1 B	III b	± 125	D5 B	I c	± 57.5	D7 B	I c	± 57.5

Figure 3.36. Pinout for the knob box

3.17   Computers

There are 3 computers used for SEMPA, shown in Figure 3.37. The computers are laid out in the same orientation as the monitors.

The keyboard and mouse are shared across the machines; which machine is controlled is handled by the small black switch usually found next to the keyboard. The order is whisk > doorbell > bracket > unused.

doorbell (Windows 7 Professional, top center)

> This machine is connected to the Internet. It has most of the SEMPA images and documents in `C:\sempa`.
> The main user account is `sempa`

bracket (CentOS 5.10, top right)

> This machine hosts `Auger Master`. It is not connected to the Internet.
> The main user account is `aes`.

whisk (Debian 6.0.10, bottom center and right)

> This machine hosts the `sempa` software. It is not connected to the Internet.
> The main user account is `sempa`.

Figure 3.37. The computers for the SEMPA

3.18 Software

3.18.1 `Auger Master`

This is the JEOL software for operating the SEM. `Auger Master` is launched from the `Auger Master` icon on the desktop or in the Applications menu. The main windows for controlling the SEM are shown in Figure 3.38.
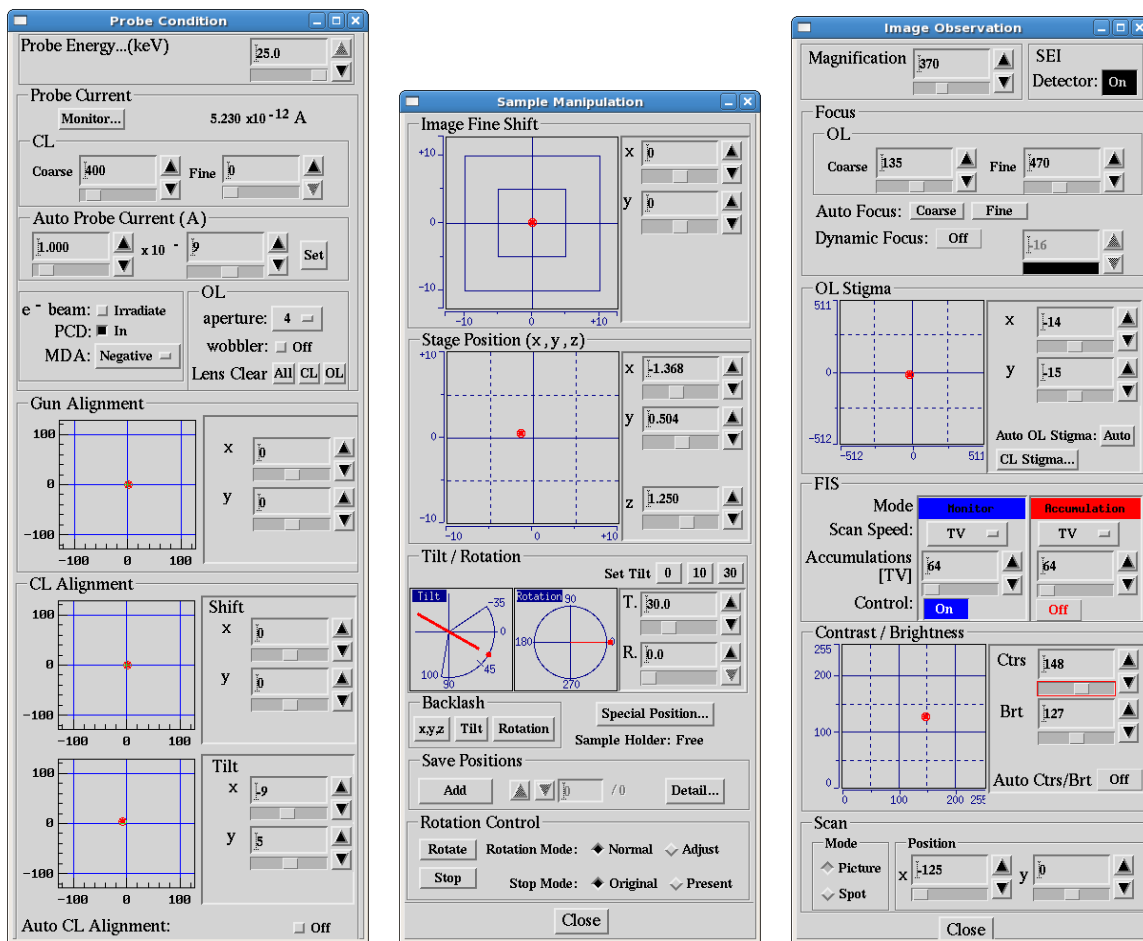
(a) The probe condition window in `Auger Master`

(b) The sample manipulation window in `Auger Master`

(c) The image observation window in `Auger Master`

Figure 3.38. `Auger Master` observation windows

3.18.2 `sempa`

This is the NIST software for operating the SEMPA column. `sempa` is launched from the command line. See Magnetic Domain Imaging for more details.

Chapter 4

Alignments

4.1 Field emission gun (FEG)

The thermally assisted FEG sits atop the electron column. Electrons that are emitted from the tip (first thermally excited, then pulled out by the extraction voltage) need to travel in a well-defined path down to the sample. This process is documented in Technical Material TI-99052AP001 from JEOL, found in a white binder in the SEMPA file cabinet.

As a first step, the FEG is physically aligned by turning the 4 hex head screws as necessary to maximize current to the closed PCD. This should only need to be done with the FEG is changed. Standing in front of the machine, the screw in front on the left is the X+ adjuster; the front right is the Y+ adjuster (opposites on the rear).

- Ensure that the manual valve (knob just above the aperture on the right side of the main column) is fully open.

- Ensure the accelerating voltage is 25 kV.

- Verify the aperture is set in `Auger Master` to 5 (aperture removed from beam path).

- Pull cable `A3` from the back left corner of the console.

- Set all gun and CL alignment values to 0 in `Auger Master > Probe Condition`, as well as `CL Coarse` and `Fine`.

- Insert the PCD.

- Set the `Auger Master > Probe Condition > MDA` to PCD.

- Adjust the upper screws until the probe current is maximized. Opening the probe current monitor can be helpful to see small trends when adjusting.

- Remove the PCD and observe a feature at ~1300x.

- While changing the `CL Coarse` from 0 to ~50 in `Auger Master > Probe Condition`, adjust the upper screws as necessary to keep the feature from moving.

- Turn on the `OL Wobbler` in `Auger Master > Probe Condition`.

- Adjust the CL shift and tilt values until the image does not move.

- Set `CL Coarse` and `Fine` values to 0.

- Reconnect A3.

- While changing the `CL Coarse` from 0 to ~30 in `Auger Master > Probe Condition`, adjust the lower screws as necessary to keep the feature from moving.

- Change CL values from 0 to ~400, zoom in and out, and adjust focus to verify the feature does not move.

- Adjust the aperture as below.

This software part of this process (gun and CL tilt and shift) should be repeated for each desired accelerating voltage.

4.2   Aperture

The aperture alignment might need to be adjusted for each aperture.

- Select aperture.

- Get an image if one doesn't show immediately. This is as much art as science. Keep an eye on the probe current to look for values in the 1×10^{-9} range (less than that is no real current) while adjusting the objective aperture fine tuning knobs. The current likely will start in the 1×10^{-12} A range.

- Once an image is acquired, zoom in to 3000x or higher if possible (this makes astigmatism issues easier to see).

- Adjust focus to best possible, then tweak stigmators as needed.

- Turn on the HT Wobbler and adjust amplitude to something useable.

- Adjust the aperture knobs until the focus racking does not translate.

    – The transverse adjustment knob affects horizontal motion of the wobbler; the axial knob affects vertical motion.
    – It is generally possible to eliminate horizontal motion fairly easily.

- – If the vertical motion persists up until signal cut-off, adjust to the edge that shows least motion, then turn up the probe current/CL coarse adjustment. The image should brighten and the knob should be able to turn farther before stopping the signal. Continue adjusting until the vertical motion is eliminated.

- Zoom in to 10,000x+ and further tweak fine focus and stigmation. It might be worthwhile to also clear the CL and OL lenses (in `Auger Master > Observation > Probe Condition`).

4.3 Micro Ion Etching Device (MIED)

The MIED is finicky on a good day (see The MIED will not mill). The alignment procedure is documented in section 27.3 of the JEOL JAMP-7830F manual. The values shown in Table 4.1 provide a good starting point for aligning the MIED.

Item	X	Y
Energy/Current	2000	200
Intensity/Focus	0	152
Beam Position	-60	-12
Column Alignment	-3	-3
Energy/Current	500	200
Intensity/Focus	0	152
Beam Position	-62	-21
Column Alignment	-3	-3
Energy/Current	200	90
Intensity/Focus	0	152
Beam Position	-60	-12
Column Alignment	-3	-3

Table 4.1. Starting values for MIED channel settings

Chapter 5

Startup and Shutdown

Starting the base instrument, assuming pressures are in reasonable ranges, is a matter of turning on 4 switches on the rack on the bottom left of the console right to left, bottom to top.

- `JEOL HT`

- `ACCEL HT`

- `OPN POWER`

- `ACCEL VOLTAGE`

Shutdowns of the console should happen in the opposite order: left to right, top to bottom.

5.1   Auger Master

`Auger Master` can be started by double-clicking the icon on the desktop on **bracket**. A splash screen will come up with the text `Connecting to console....` Once that completes successfully (see `Auger Master` will not connect on launch in case that does not happen), the main window shown in Figure 5.1 will appear.
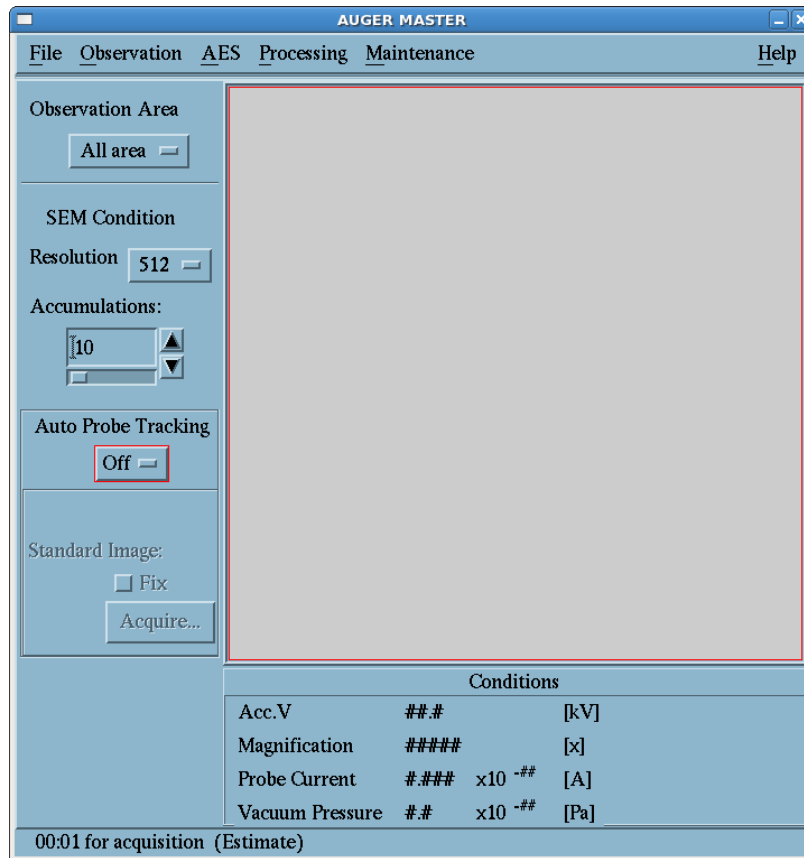
Figure 5.1. Main window for `Auger Master`

To start the FEG, select `Maintenance > FEG Control`, shown in Figure 5.2a. The `Start` button will begin the auto start process.

The progress of startup, as well as realtime condition monitoring, is achieved by selecting `Observation > FEG Monitor`, shown in Figure 5.2b.

The initial conditions used for the gun startup are set by `Maintenance > FEG Start Up Tuning`, shown in Figure 5.3a. Note the startup maximum gun pressure is fixed at 5×10^{-7} Pa. The filament current should be selected to achieve ~90 µA of emission current once warmed up, keeping the filament current below the value that will heat the tip beyond 1,800 K (maximum temperature for the health of the FEG tip). At the time of this writing, that value is 2.41 A for the installed tip. Extraction voltages are typically ~3,000 V.

Once the FEG is running, filament current, suppressor voltage, and extraction voltage can be modified by selecting `Maintenance > FEG Control > Fine tuning...`, shown in Figure 5.3b. Suppressor voltage is typically left at 300 V.
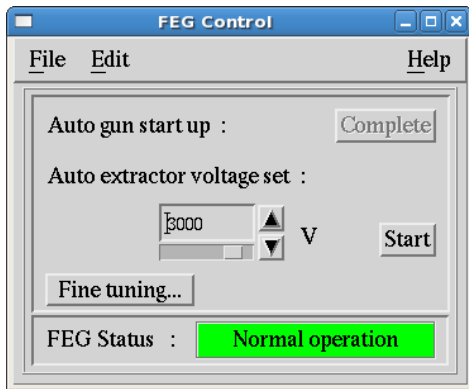
(a) The FEG startup window
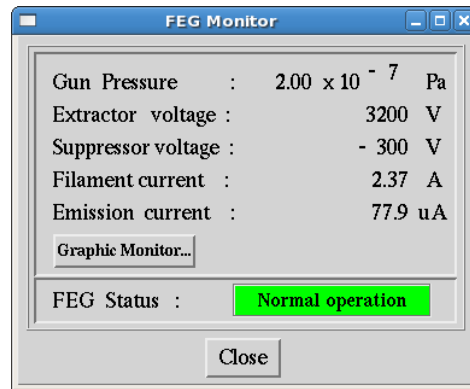
(b) FEG monitor window

Figure 5.2. Windows for starting and monitoring the FEG
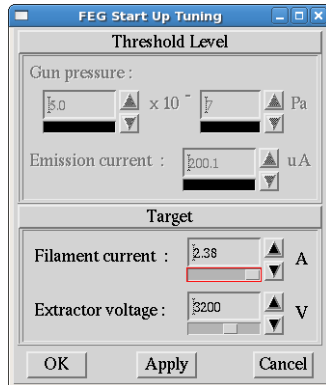
(a) The FEG startup tuning window for initial conditions
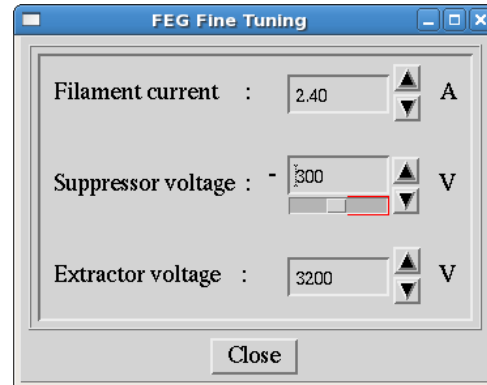
(b) FEG fine tuning window for runtime conditions

Figure 5.3. Windows for adjusting the FEG startup and runtime parameters

5.2 Venting for maintenance

When performing maintenance, often at least some part of the system will need to be vented. The FEG should be turned off for this: `Auger Master > Maintenance > Shutdown FEG`. This will take several seconds.

Close the manual valve located just above the aperture on the right side of the main column. Remember to reopen the valve after the maintenance is complete.

Table 5.1 is reproduced from the JAMP-7830F manual, section 6.3.1d. Select the appropriate vent button on the vacuum control panel (Figure 5.4). Pressing the button again within 5 seconds will cancel the vent process. Once the venting begins, `AV1` will open (and the corresponding LED will illuminate); once the venting is complete, `AV1` will close and `AV2` will open, remaining open throughout the maintenance. At this point it is safe to open the evacuated parts of the system.

Button	Chamber(s)	Vent time
VENT 2EXC	Airlock	2 minutes
VENT CHAM	Airlock Main chamber	5 minutes
VENT eGUN	Electron lens chamber	2 minutes
VENT ALL	Electron lens chamber Main chamber	7 minutes

Table 5.1. Venting options
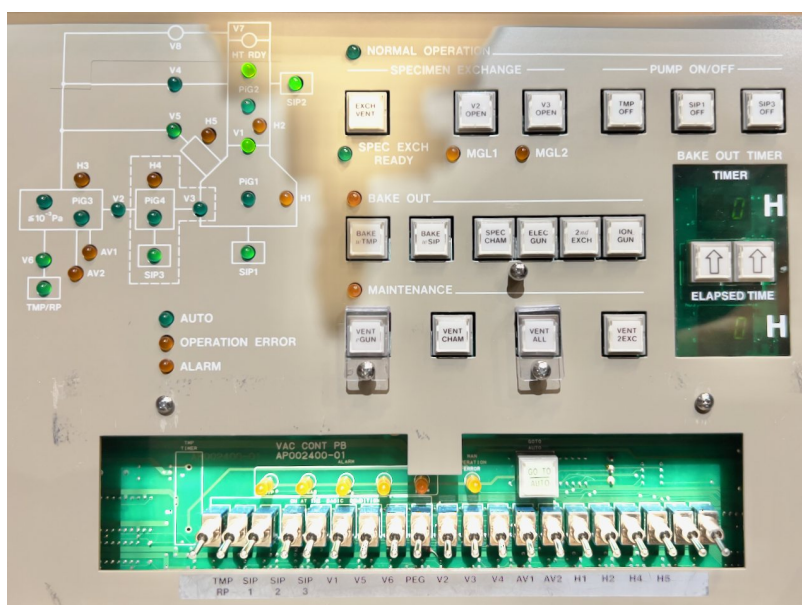
Figure 5.4. Vacuum control panel

After venting, the instrument will automatically initiate a bakeout. How long it should bake depends on what was done; 2 hours is typically the minimum. The bake duration is set with the two ⇑ buttons in the BAKE OUT TIMER section of the panel. The rest of the system should be baked as well to ensure all contaminants get pumped out; see Bakeouts.

Press the button selected above to begin the pump down and bakeout.

5.3 Full shutdown

This procedure is useful when a power outage is anticipated, *e.g.* in the case of building maintenance.

- Turn off the 4 switches listed above.

- ACCEL VOLTAGE

- OPN POWER

- ACCEL HT

- JEOL HT

- Close the manual valve.

- Turn off the `ION GUN POWER` switch.

- Turn off the `FIL ON` switch on the Ionization Gauge for the MIED.

- Turn off the `FIL ON` switch on the Ionization Gauge FEG.

- Turn off the `EMIS` switch on the main chamber gauge (Ionivac IM 520).

- Turn off the `ON` switch on the Parking gauge (GP 307 Vacuum Gauge Controller).

- Toggle off the `POWER` switch for SIP 4.

- Press the `STOP` button on the `TMP STP CONTROL UNIT` against the back wall. The turbo will take ~20 minutes to spin down.

- Turn off the `MAIN POWER` switch

Restarting is the opposite of the above, with the exception of the pressure gauges: if the pressures have fallen sufficiently, the SIPs will be out of range. Allow the system some time to pump back down, checking the ion pumps periodically.

Chapter 6

Standard Imaging

6.1   Sample exchange

The sample exchange chamber must be vented to atmosphere to insert a new sample. Plan ahead and stage any samples you might wish to remove to minimize time pumping down (~90 minutes when the instrument is relatively clean).

- Press the EXCH VENT button on the vacuum control panel (see Figure 5.4).

- Loosen the knob holding the exchange door closed.

- Wait for the chamber to pressurize.

- Remove any sample waiting to come out.

- Place the new sample in the exchange fork. The sample holder's top slot should go into the exchange fork in the instrument.

- Close the door and snug the knob.

- Press the EXCH VENT button and wait for the system to pump back down.

  - The Pfieffer vacuum pump in front of the exchange chamber can be used to help expedite the beginning of the pump down. Note that it shows pressure in mbar; 1 mbar = 100 Pa, so the chamber gauge is 2 orders of magnitude higher than what shows on the pump.

  - The Pfieffer is not useful beyond $\sim 1 \times 10^{-3}$ Pa in the chamber.

  - The chamber is pumped down enough once it reaches 3×10^{-5} Pa.

Once the exchange chamber has pumped down, it is safe to move the new sample into parking.

6.2 Parking

The parking chamber includes an arm that comes in from the back of the machine with 4 slots. This allows for storing samples in vacuum without needing to pump down. Note that the rearmost slot in the parking holder requires V2 to be open (it is ~1 cm too long).

Access the parking chamber from the sample exchange area by opening V2. Note that the exchange arm sticking out from the front of the instrument will need to be fully retracted for V2 to open; the MGL 1 lamp will illuminate if this is not the case.

Open V2 by pressing the V2 OPEN button in the vacuum control panel.

6.3 Main chamber

The main chamber is where the sample is viewed. It is accessed via V3. Again, the exchange arm in front must be fully retracted for V3 to open.

The stage is prepared for sample exchange by selecting Auger Master > Observation > Sample manipulation... > Special Position... > Sample Change Position > Move.

6.4 Eucentric height

To optimize the imaging contrast, milling, or SEMPA operations, the sample must be at eucentric height. This is achieved by setting the Auger Master > Observation > Sample manipulation... > Stage Position > z such that changes to the sample tilt do not cause the image to shift left or right.

Sample exchange lowers the stage to ~-1.1; +1.1 is a good starting point for finding eucentric height.

- Set stage tilt to 0°.

- Find a feature at ~500x zoom and center it.

- Press the Auger Master > Observation > Sample manipulation... > Tilt / Rotation > Set Tilt > 10 button to tilt the stage to 10°. Note that this will increase the signal from the sample: lower the contrast to prevent E-T detector saturation.

- Go back to 0°, then return to 10°to minimize backlash in the stage.

- Adjust the z height until the feature has returned to the center.

  - Movement to the left indicates the stage is too low: increase z.

  - Movement to the right indicates the stage is too high: decrease z.

- Return to 0°and verify the feature is still centered.

- Return to 10°and verify the feature is still centered.

Note that while tweaks to focus ideally should not cause the image to move, in a less-than-perfectly calibrated system there will be some minor impact.

6.5   Controls

The stage control panel, shown in Figure 6.1a, is used for moving the stage.

- Translate across X and Y

- Raise and lower

- Rotate

- Tilt

Note that the HOLD ON lamp indicates that the control is disabled; press HOLD OFF to regain control.

The optics control panel, shown in Figure 6.1b, is used to change the SEM image.

- Fix stigmation/coma in X and Y

- Adjust the condenser lenses to increase or decrease probe current

- Change magnification

- Adjust focus

- Change contrast (difference between darkest and bright signals) and brightness (effectively black level)

- Change scan speed (not typically used)
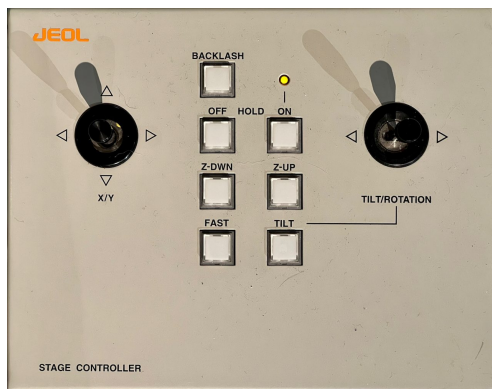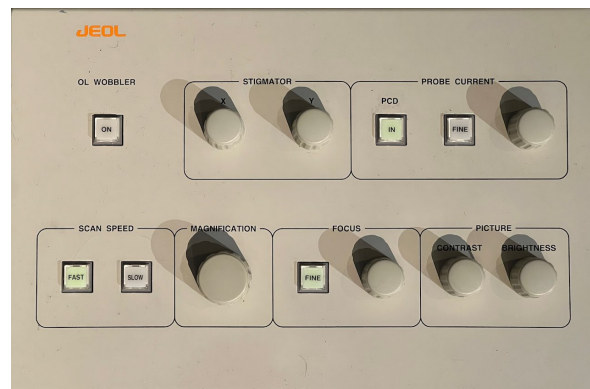
(a) The stage control panel   (b) The optics control panel

Figure 6.1. SEM controls

Chapter 7

Auger Analysis

Auger analysis performs energy spectroscopy on so-called Auger secondary electrons scattered from the Auger effect (though Ben might prefer these be called Meitner electrons and the Meitner effect). When an incoming electron of sufficient energy (25 keV will do) scatters an electron from an inner shell of an atom, it creates a hole. This hole can be filled by an electron from a higher orbital. If the binding energy of the lower orbit is considerably less than the transition energy of the lowered electron, the excess energy can cause another higher shell electron to be ejected. These energies are relatively low, leading to a short mean free path. The electrons that break free from the sample are thus from the top several layers (on the order of 1 nm of the sample.

As Auger analysis requires a clean surface, typically the procedure is to take an initial scan to get a sense of what is on top, then go back and forth between ion milling and scanning.

There are a number of Auger scan types available. In the interest of timeliness (as the scan must go through a range of energies, dwelling on each step for a specified time), it is often useful to run a spectrum scan with a limited set of regions of interest (ROIs).

Figure 7.1 shows an example of an Auger spectrum analysis: here 4 energy ROIs, namely for O, Fe, Gd, and Pt, are examined. O shows an unexpected peak (this was immediately after milling, which would have removed any surface oxygen, suggesting there is oxygen in the sample). Fe shows the 3 characteristic peaks at roughly 650, 700, and 750 eV. Both Gd and Pt show no signal (a Pt capping layer was just milled off, and the Fe layer covers the lower Gd layer).
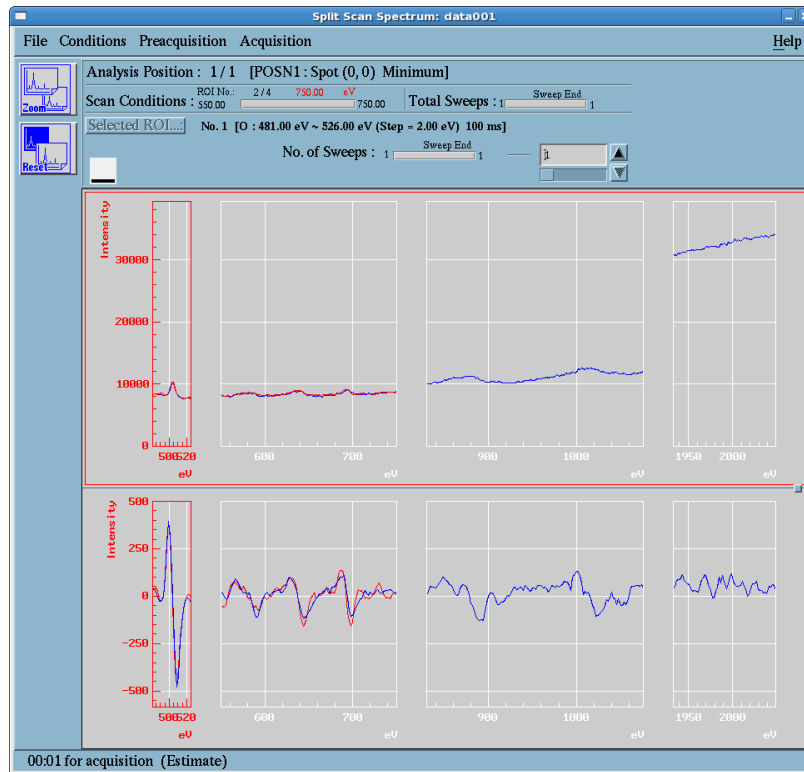
Figure 7.1. A sample spectrum analysis showing O and Fe peaks

Figure 7.2 shows the ROI configuration for the scan above. The selected ROI table includes energy values for all relevant elements, allowing for simply entering the symbol for the element of interest.
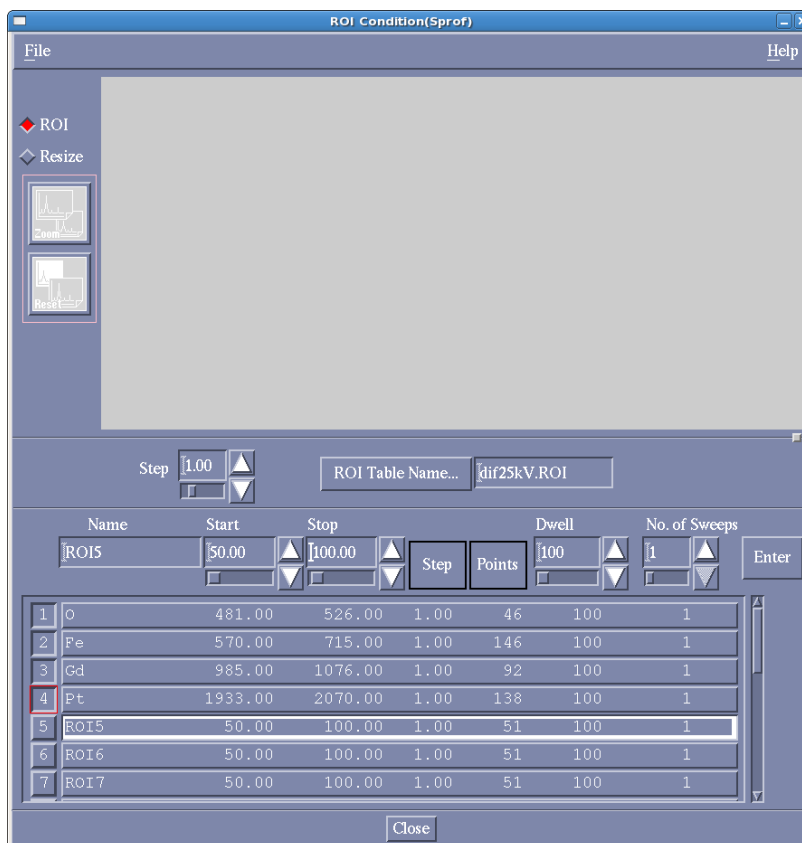
Figure 7.2. ROI configuration window

Chapter 8

Ar Ion Milling with the MIED

The MIED is used to prepare sample surfaces by removing contaminants with a stream of energetic Ar ions.

There are 3 configurations stored in channels 10, 15, and 11, for 2,000 eV, 500 eV, and 200 eV, respectively. The sample being cleaned will drive which energy should be used. Approximate etch rates measured when the instrument was at NIST are in Table 8.1.

The MIED is controlled by the components on the bottom left of the console; see Figure 3.16.

- Ensure the `ION GUN POWER` button is illuminated.

- Ensure the `HEAD`, `MEAS`, and `FIL ON` buttons on the Ionization Gauge are illuminated.

- Press the `AVC` button; the display will show lines.

- Turn on the `POWER` switch on the GP 216 Pressure/Flow Controller. Allow 2-3 minutes for it to settle.

- Turn on the `CONTROL` switch on the GP 216 Pressure/Flow Controller.

- If the gauge spikes and shows `E-H`:

    - Turn off the `CONTROL` switch.
    - Turn the `MEAS` and `FIL ON` buttons on.
    - Turn the Reference knob down.
    - Repeat the previous step.
    - If the pressure stabilizes around 5×10^{-2} Pa, increase Reference back to 5.0.

- Select the channel with the desired energy.

- Press `BEAM ENERGY/EMIS CURRENT` to verify correct energy and current values.

- Press `BEAM SPOT` if appropriate.

- Press `TIMER RESET` if desired.

- Press `TIMER DISPLAY`.

- Turn off `Auger Master > Observation > Image Observation > SEI De-`
  `tector` to minimize damage to the e-t.

- Close the PCD.

- Press `ETCHING ON/OFF` to begin etching. The timer will begin.

- Press `ETCHING ON/OFF` to end etching. The timer will stop.

If appropriate, analyze the sample to see if sufficient milling has been done. Repeat the last 4 steps until done.

- Change to channel 1. This maintains a minimal current through the tip.

- Turn off the `CONTROL` switch on the GP 216 Pressure/Flow Controller.

- Allow 5 minutes for the system to cool down.

- Turn off the `POWER` switch on the GP 216 Pressure/Flow Controller.

- Press the `AVC` button. The pressure should drop to ~1×10^{-5} Pa.

Element	50 eV	100 eV	500 eV	1,000 eV	2,000 eV
Co	0.04	0.3	1.3	2.0	2.8
Cr	0.04	0.25	1.1	2.0	2.6
Pt	0.05	0.3	1.4	2.1	3.0
Au	0.07	0.5	2.1	3.5	5.0
Si	0.005	0.07	0.42	0.7	0.95

Table 8.1. MIED etching rates; units are nm min^{-1}

Chapter 9

Ar Plasma Milling in the Sample Exchange Chamber

The plasma gun sits atop the sample exchange chamber. It can be used to gently mill samples with a low energy Ar plasma.

- Check the water level in the tank next to the pump in the service chaise.

- Turn on the pump.

  - Validate pressure is ~20 psi.
  - Validate flow rate is ~0.5 L min^{-1}.

- Open the leak valve to allow Ar to enter at a pressure of 0.06 Pa to 0.09 Pa.

- Ensure the Magnetron Supply Power knob is turned down.

- Turn on the Magnetron Supply.

- Increase the Power knob slowly until a reading of 40 mA to 50 mA. Ensure there is no purple glow showing in the small window in the gun.

- Ensure the Grid Supply Extraction and Ion Energy knobs are turned down.

- Turn on the Grid Supply.

- Increase the Extraction knob to 200 V. Ensure the current does not go much above 1 mA.

- Increase the Ion Energy knob to the desired beam energy.

- If the power supply clicks, adjust the voltages to make it stop.

When done, decrease the knobs to 0 and turn off the power supplies. Allow a few minutes for cooling and then turn off the water pump.

(a) The rack of controls for the plasma gun
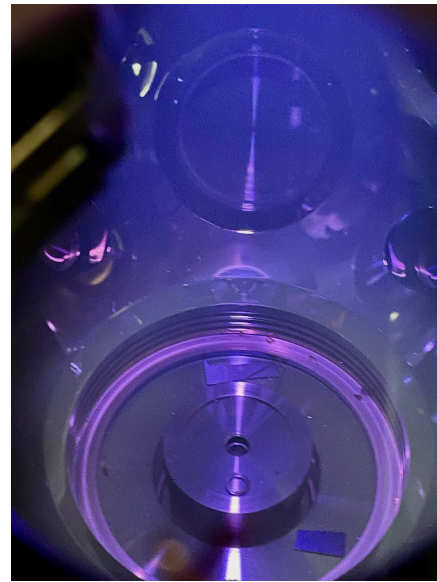
(b) The purple glow of the functioning plasma chamber

Figure 9.1. Plasma controls and glow

Chapter 10

Electromagnet

The electromagnet located at the rear of the SEMPA allows for applying a magnetic field to a sample once in the vacuum. This can be handy in the case of needing to magnetically prepare or modify a sample (*e.g.*, nucleating skyrmions in an Fe/Gd multilayer thin film) after ion cleaning.

The sample to be put in the electromagnet must first be loaded onto the parking arm, then moved all the way rearward until it can be moved onto the electromagnet arm. There is a small wiper that can assist with pushing the sample holder from the parking arm onto the electromagnet arm. The sample is then moved between the poles of the magnet, visible through the glass apertures. The sample can be rotated relative to the poles; there is an angle scale on the rotating dial to the right to help gauge the angle of rotation.

Once in place, turn on the power supply and adjust the current to the desired value. The simplest technique for this is to set all power supply knobs to the their minimum, then increase the current knob(s) to maximum. With the voltage knob(s) down, no current will flow. Slowly increase the voltage, keeping an eye on the current.

There is an FW Bell GH-600 Hall effect sensor in the magnet chamber; unfortunately, at the time of this writing, it appears at least one of the contacts in the vacuum is broken. Ideally this sensor would be used to monitor real-time magnetic flux in the area of the sample.

As an alternative, to get some characterization of the magnet's field strength, Table 10.1 below shows the magnetic field strengths measured with a Lakeshore 410 Gaussmeter inserted between the yoke and one of the coils for given current inputs to the electromagnet. Table 10.2 extrapolates the currents required for given strengths.

A	mT
0.00	22.0
0.50	94.2
1.00	145.6
1.50	216
2.00	296
2.50	365
3.00	434
3.50	505
4.00	576
4.50	646
5.00	718
5.50	775
6.00	837
6.50	898
7.00	963

Table 10.1. Measured fields for given currents

mT	A
100	0.57
150	0.94
185	1.19
200	1.30
250	1.67
300	2.04
400	2.77
500	3.50
600	4.24
700	4.97
800	5.71
900	6.44
1,000	7.17

Table 10.2. Required currents for desired fields

Chapter 11

Magnetic Domain Imaging

11.1 Prepare sample

In order to gather SEMPA images, the sample must have a surface free from magnetic signal blocking elements. Most often this will be a layer of oxygen from oxidation or some capping material added when the sample was created. See Ar Ion Milling with the MIED and Ar Plasma Milling in the Sample Exchange Chamber.

Care should be taken to not overheat the sample, thus modifying or destroying the magnetic texture to be imaged, or even the sample itself (as can happen with transmission electron microscope (TEM) samples in particular due to their thinness).

Once the sample is ready:

- Ensure the MIED is off and pressures have returned to normal.

- Tilt the stage to 52°, adjusting contrast/brightness as necessary.

- Ensure that the stage is at eucentric height.

- Carefully lower the SEMPA optics after removing the aluminum spacer.

- Ensure the sample has a feature that can be tracked easily as turning on the SEMPA optics will move and distort the image. The `Save Positions` feature on the `Auger Master > Observation > Sample Manipulation` window can be particularly helpful: save the spot to be imaged before turning on the SEMPA optics to have a reference point. If the feature used for tracking is in a different location than the region of interest, that spot can also be saved.

11.2 Turn on SEMPA electronics

The viewed area and image settings must be adjusted before imaging. Once the voltages are turned all the way up, the image will shift roughly $250\,\mu$m to the left and $20\,\mu$m down.

- Turn on power supplies

  - kepco power supply AC (left switch)
  - 5V Descan Power
  - NIST HV supply (just above the kepco)
  - UEP 15 NIMS power supply
  - SEMPA 0°/90° DETECTOR SIGNAL MULTIPLEXER
  - JEOL SEMPA APERTURE CURRENT MONITOR

- Ramp up the voltages while keeping the feature to be tracked in view.

  - Turn on the kepco DC voltage (right switch) and set the knob to 400 V to 600 V.
  - Turn on the left-most NIMS power supply (NMQ 102M, labelled "Input Lens") and set to 500 V.
  - While keeping the kepco voltage 100 V to 200 V above the input lens and adjusting contrast and stage position, increase the input lens to 1,500 V and the kepco to 1,600 V to 1,800 V.

- Turn on SEMPA E-T detector

  - Toggle on the `HV ENABLE` switch on the HV supply.
  - Ensure the Scintillator HV power supply is set to 0 and toggle it on.
  - Ensure the E-T detector selector switch is set to `SEMPA ST` of `SEMPA RA` as appropriate.
  - Increase the Scintillator HV dial to 250 (2,500 V).

In all likelihood, the SEM image screen will be dark. The SEMPA column voltages might need tweaking to view an image.

- Turn the target knob on the SEMPA column to 45°.

- If a bright area is not visible, increase contrast/brightness; if still not visible

  - Zoom out to ~50x.
  - Adjust the `D1`, `D2`, and `D3` knobs slightly until the illuminated area is visible.
  - Increase contrast/brightness if necessary; neither should have to go above 200 as reported in `Auger Master Image Observation`.

- Adjust the deflector knobs as required to maximize brightness in the area to be imaged, zooming in to the desired magnification.

- Adjust stigmation as required; typical values are around +100 in Y and +20 in X.

- Adjust focus as required.

- Decrease the Scintillator HV dial to 0.

- Toggle off the `HV ENABLE` switch on the HV supply.

- Turn the target knob on the SEMPA column to 0°(fully counterclockwise).

- Turn on all the supplies in the NHS 6005p power supply.

- Turn on the ST or RA analyzer as required. There are 2 switches each, one for the multi-channel plates (MCP) and one for the anode.

- Increase the MCP and anode voltages, keeping the anode ~100 V above the MCP, to ~1,500 V.

- Adjust the voltages until the sum monitor at the top of the rack reads 30 µA.

11.3   Imaging

Switch the keyboard and mouse over to whisk. If not already running, launch the `sempa` software from the command line. The window shown in Figure 11.1 should open on the bottom center monitor.

- Select the appropriate folder for the data to be collected.

- Set the prefix for the files to be generated.

- Set the first run number.

- Select straight through (`X-Y`) or right angle (`X-Z`).

- Close the PCD and select `sempa > Options > Measure SEMPA Zeros`. If the resultant images are not fairly evenly noise, repeat until they are.

- Add one or more scan specifications as required. X/Y number of points and dwell time will be dependent on the sample material and goal. Note increasing either can have a significant effect on capture time.

- Capture images. The images will be rendered in real time on the bottom left monitor; Figure 11.2 is an example.

  - `Free Run` is often used for lower resolution/shorter dwell times to find interesting features; the resultant images will not save or increment the run number.

  - `Start` saves the four resultant images to the folder selected above with the specified name and run number: *e.g.,*
    `FeGd3x001_ix.sempa, FeGd3x001_iy.sempa, FeGd3x001_mx.sempa, FeGd3x001_my.sempa`

– The `...ix...` and `...iy...` images should be the same: intensity images from the E-T detector, while the `...mx...` and `...my...` images are the magnetization images for X and Y, respectively. Selecting the `X-Z` would result in `...ix2...`, `...iz...`, `...mx2...`, `...mz...` suffixes.

Turn everything off in the reverse order.
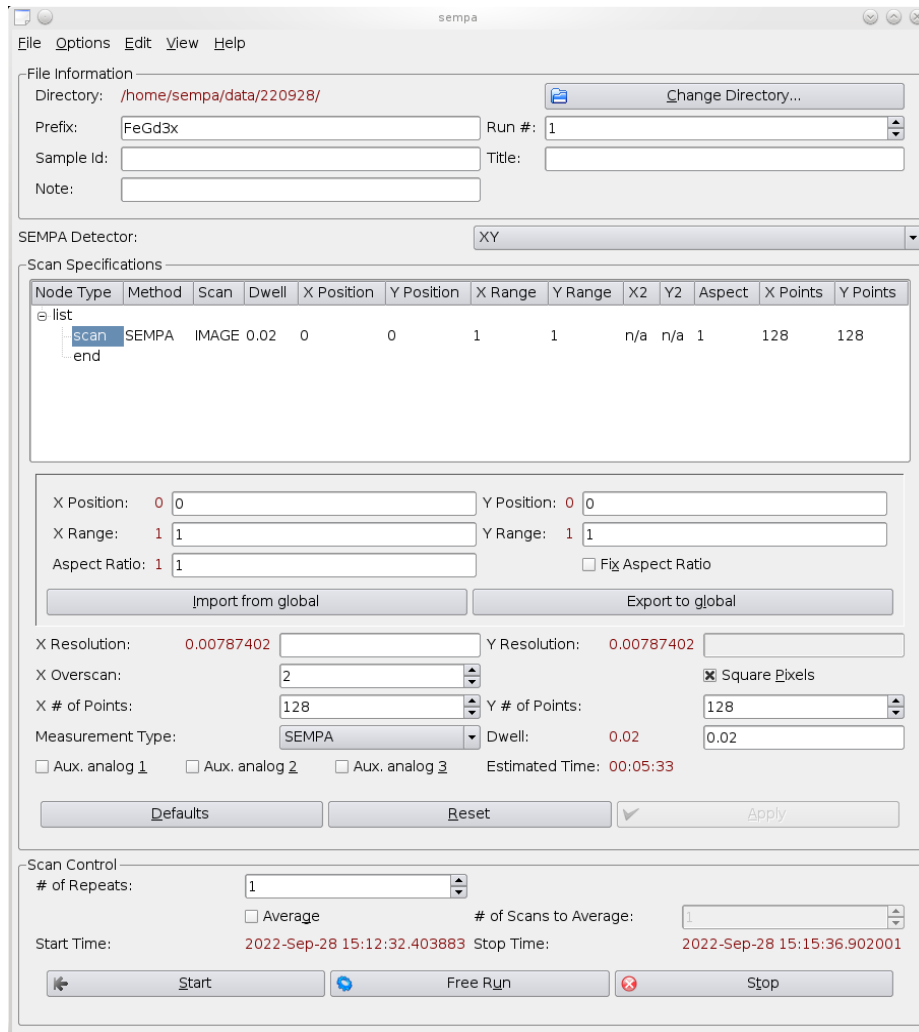
Figure 11.1. The main window for the sempa software
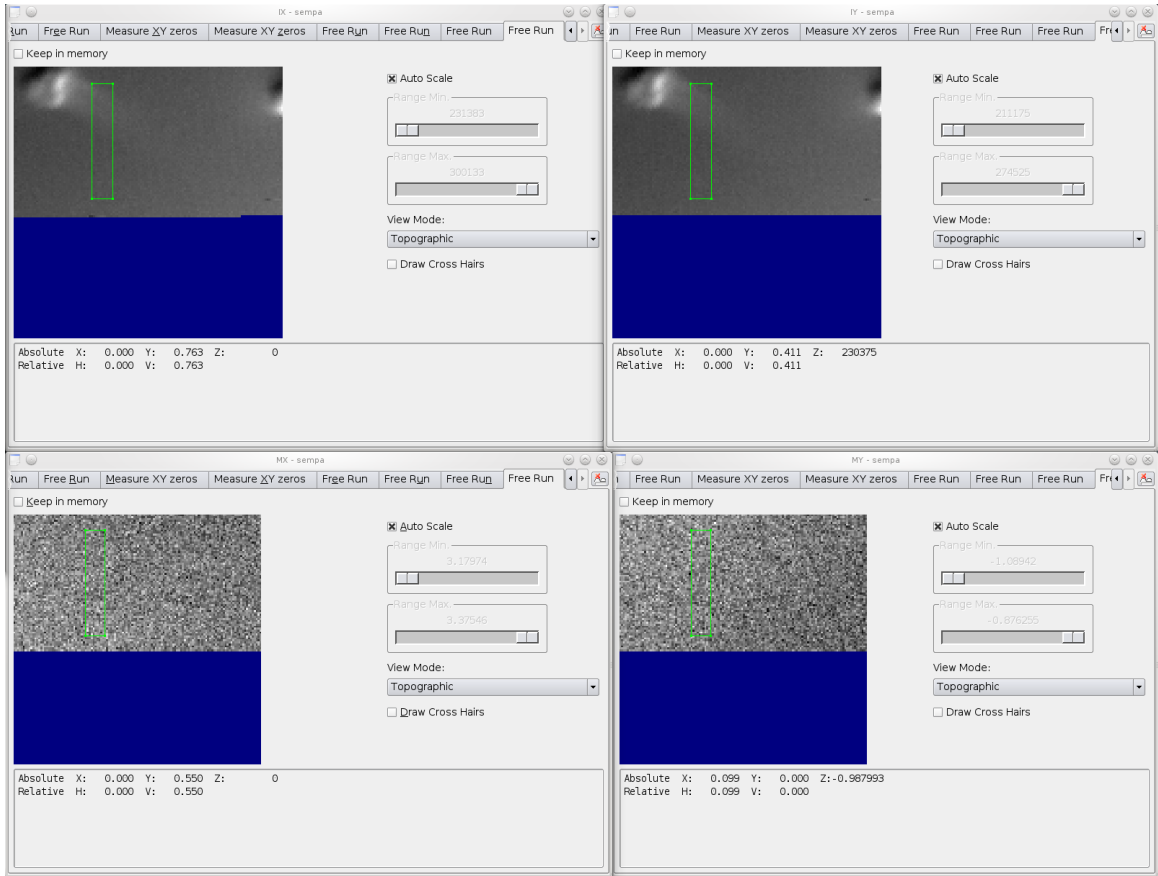
Figure 11.2. Sample images being captured in the X-Y plane

Chapter 12

Maintenance

12.1   Manual mode

Occasionally the instrument must be operated in manual mode. Most often this is after it has shut down for some reason. A number of switches controlling pumps and valves must be manipulated in order to return to automatic mode (the normal operating condition). The instrument must be returned to "basal state" before automatic mode can be resumed.

- Remove the metal cover at the bottom of the vacuum control panel (Figure 5.4).

- Press the `GO TO AUTO` button so that it is deactivated (out).

- Ensure all switches are toggled off (down).

- Turn on the `TMP RP` switch.

- Depending on the pressures, toggle the SIP and valve switches. The correct order involves getting the high pressure out to the turbo pump without upsetting some other part of the system. This can be hit or miss, and might require restarting. Perseverance pays off.

- Once the 3 SIP switches, `V1`, `V5`, `V6`, and `PEG` switch have been turned on without illuminating the `MAN OPERATION ERROR` lamp, press the `GO TO AUTO` button. It should illuminate.

If (when) at any point in the above process the `MAN OPERATION ERROR` lamp illuminates, toggle all switches off and start over again. The process can take multiple iterations as the pressures in the system get sorted out.

12.2 Bakeouts

Even in an ultra high vacuum environment, there are still contaminants that will congregate and collect on the walls of the instrument. Water vapor is a common problem that will build over time as samples as exchanged or any work requiring venting is done.

Periodic bakeouts help the SEMPA maintain the necessary vacuum by increasing the temperature in the instrument above boiling, ideally to ~140 °C.

The main column has heaters built in that will handle this, controlled by the `BAKE OUT` section on the Vacuum control panel. The rest of the instrument will need to be wrapped in heater tape (some is generally left in place).

All cables and water lines should be disconnected. The mu-metal plates should be removed. Finally, the entire system wrapped in aluminum foil to help keep the heat in.

Ensure any samples are either removed from the main chamber or put into Bakeout Position (`Auger Master > Observation > Sample manipulation... > Special Position...  > Bakeout Position > Move`).
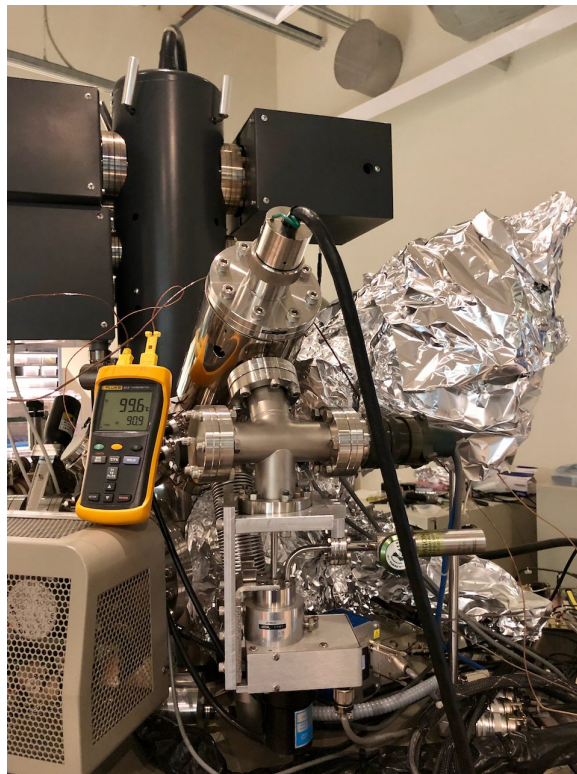
Figure 12.1. The SEMPA column wrapped and ready for bakeout

12.3 TSP

The titanium sublimation pump (TSP) helps to achieve the ultra high vacuum environment required for SEMPA. It works by running a current through a Ti filament. As the filament heats up, Ti atoms boil off and capture contaminants in the chamber before sticking to the chamber walls. Bakeouts help remove the build up that happens with TSP use.

The TSP should be operated weekly during normal operation.

- Ensure the TSP CURRENT ADJ knob is turned fully counterclockwise.

- Press the TSP button. It should illuminate.

- Slowly increase the current by turning the TSP CURRENT ADJ knob clockwise while monitoring the main chamber pressure. The pressure likely will not increase significantly until the current approaches 20 A. A rapid rise in pressure, as well as a pressure above $\sim 1 \times 10^{-5}$ Pa, will cause the system to shut down. The pressure can safely be raised (slowly!) up to $\sim 5 \times 10^{-6}$ Pa without concern.

- After 2 minutes, the TSP cycle will end and the button will begin flashing. Turn the TSP CURRENT ADJ knob fully counterclockwise and press the TSP button. It should extinguish.

Note that the TSP filaments are consumable items.

12.4 Cleaning the gold targets

The gold targets need to be cleaned every few weeks.

- Turn the knobs on the SEMPA columns fully clockwise.

- Attach the blue cables to the columns.

- Attach the high/signal sides of the splitter to the gold targets.

- Attach the low side to the 1,000 V supply.

- Close the butterfly and MIED valves.

- Launch the Granville Philips pressure monitor on doorbell.

- Power on the voltage supplies and set the grids to +180 V, filaments to +30 V.

- Power on the current supplies, set a 2 V limit, reduce the current to 0, and turn on the outputs.

- Power on the high voltage supply and set -1,000 V for the gold targets.

- Turn on the electrometer.

- Increase the current to 1 A. Monitor the pressure in the software.

- Increase the current to 2 A.

- Look for 4 mA of emission.

- Go to manual mode on the vacuum control panel. Ensure all switches are off.

- Turn on SIPs 1 and 2.

- Open the Ar leak valve slowly ~1.5 turns, keeping an eye on the pressure software. Autoscale will help.

- Look for pressure to increase to 1×10^{-2} Pa. The emission current on the electrometer should rise.

- Wait 2 1/2 minutes.

- Close the leak valve.

- Wait 3 minutes.

- Turn down the filament currents and power off supplies.

- Turn the knobs on the SEMPA column fully counterclockwise.

- Open V6, V2, and V3.

- The pressures should drop in the software monitor.

- Power off the voltage supplies.

- Disconnect the cables from the cleaning setup and reconnect the originals.

- Open the remaining valves.

- Go to auto mode.

- Open the butterfly and ion gun valves.

- Turn on the ion gauges.

Chapter 13

Troubleshooting

13.1   Shutdown

Especially when first working with the SEMPA, it seems as though it will shut down if you look at it cross-eyed. There are many safeguards built in that will shut down the FEG in an attempt to prevent damage to the rest of the instrument (not always successfully, unfortunately).

The shutdown reason can be found in `Auger Master` by navigating to `Maintenance > FEG Control` and looking at the `FEG Status` section.

Table 13.1 is reproduced from the JAMP-7830F manual, section 8.2. The majority of shutdowns are related either to FEG emission current or vacuum pressure. With the exception of codes 1 and 2, even numbers generally represent emission current shutdowns, while odd numbers are vacuum pressure spikes.

13.2   `Auger Master` **will not connect on launch**

The base instrument stores a number of states in flipflops throughout the system. These can get out of sync with apparent reality. Recovering from this can be fairly quick or somewhat time consuming.

After stopping the `Auger Master` process, try the following steps in the order listed, attempting to restart and reconnect `Auger Master` after each.

- Select `Applications > AES > Reset AES`

- Turn off `ACCEL VOLTAGE` and `OPN POWER`, then turn on `OPN POWER` and `ACCEL VOLTAGE`

- Turn off `ACCEL VOLTAGE` and `OPN POWER`, then restart **bracket**. Once it is back up, turn on `OPN POWER` and `ACCEL VOLTAGE`

Number	State at shutdown	Cause
0	Unknown	Unknown
1	The system was shut down while the filament was being started up by the automatic gun-startup process.	Emission current
2		Vacuum pressure
3		Excess time
4	The system was shut down while the suppressor voltage was being set by the automatic gun-startup process.	Emission current
5		Vacuum pressure
6	The system was shut down while the extracting voltage was being set by the automatic gun-startup process.	Emission current
7		Vacuum pressure
8		Excess time
9	The system was shut down during the automatic gun-startup process.	Interruption command
10	The system was shut down during the automatic extracting voltage setting process.	Emission current
11		Vacuum pressure
12	The system was shut down during normal operation.	Emission current
13		Vacuum pressure
14		Shutdown command
15	The system was shut down immediately before the automatic gun-startup process was run or immediately before the automatic extracting-voltage setting process was run.	Vacuum pressure
16		Emission current
17		Gun ready

Table 13.1. Shutdown codes

13.3 No SEM image

Check the items below.

- FEG on? Typical emission current is ~90 μA.

- PCD open?

- Contrast and brightness turned up? Typical values are around 150/130, respectively, for normal SEM imaging, a bit higher for SEMPA.

- E-T detector selection switch set correctly?

- Internal/external scan switch set correctly?

- If SEMPA imaging, SEMPA input optics on, HV switch on, scintillator HV on and set to 250, column properly aligned?

13.4 The MIED will not mill

Check the items below for necessary initial conditions.

- Ensure the `ION GUN POWER` button is illuminated.

- Ensure the `HEAD` and `MEAS` buttons on the Ionization Gauge are illuminated.

- Ensure the `AVC` button on the Ionization Gauge is illuminated.

- Ensure the `FIL ON` button on the Ionization Gauge is illuminated.

- Ensure both the `POWER` and `CONTROL` switches on the GP 216 Pressure/Flow Controller are on.

- Ensure the pressure in the ionization chamber is ~5×10^{-2} Pa.

If all of that checks out but the `ETCHING ON/OFF` button seems to have no real effect, check the fuses in the Micro Ion Etching Device rack unit, shown in Figure 13.1.
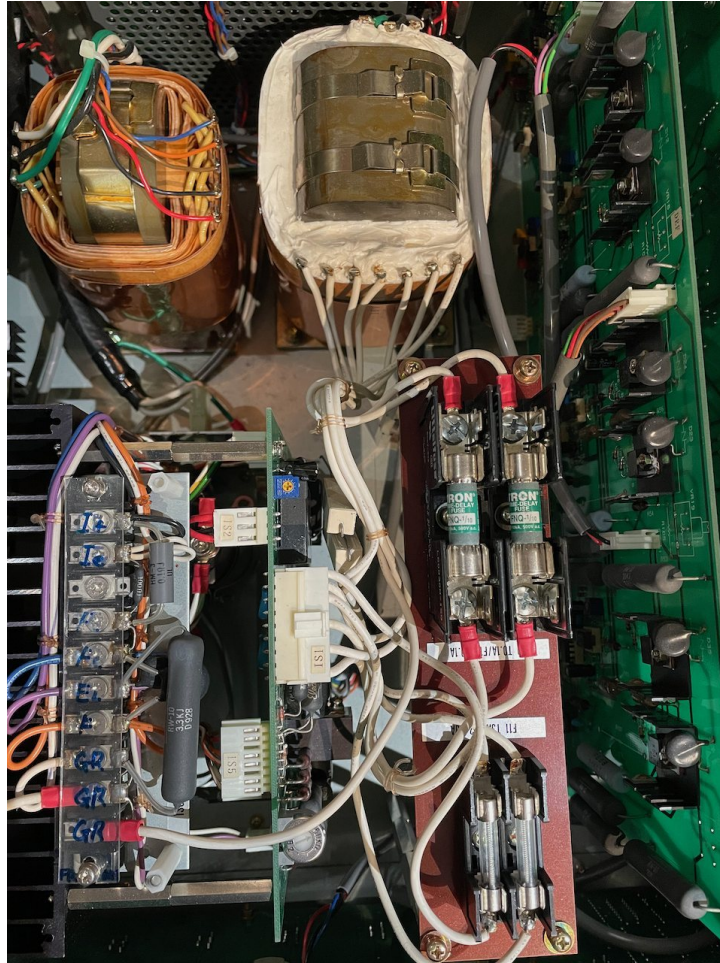
Figure 13.1. The two large gray fuses center right are prone to failing

13.5   `V2` **or** `V3` **will not open**

Ensure that the 2nd transfer arm is fully retracted. There is a safeguard built in to prevent the valves from opening if the arm is not all the way back.

13.6   Pulsing SEM image

The most frequent culprit for this is sample charging. This should be handled by grounding the sample to the holder (which is held at instrument ground).

Less frequent is a damaged light pipe. Light pipes are consumable items. The E-T detector works by electrons hitting a phosphor screen. Over time the electrons will erode a hole through the phosphor.

(a) A light pipe with the phosphor burned in the center
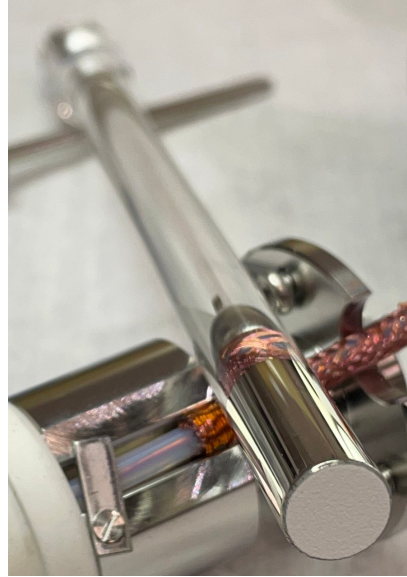
(b) A new (reconditioned) light pipe

Figure 13.2. New vs. used light pipes

Light pipes can be refurbished by Applied Beams LLC in Beaverton. As of 2021 the price was $725 per pipe.

13.7 SEM image darkens and brightens but does not zoom or focus

If the zoom is left very low (<100 x) for an extended period of time (no set time for that), the required current for the coils can cause significant Joule heating, eventually blowing fuses.

Check the deflection coil fuses on the right side of the console. There are 2 8 A fuses toward the back.
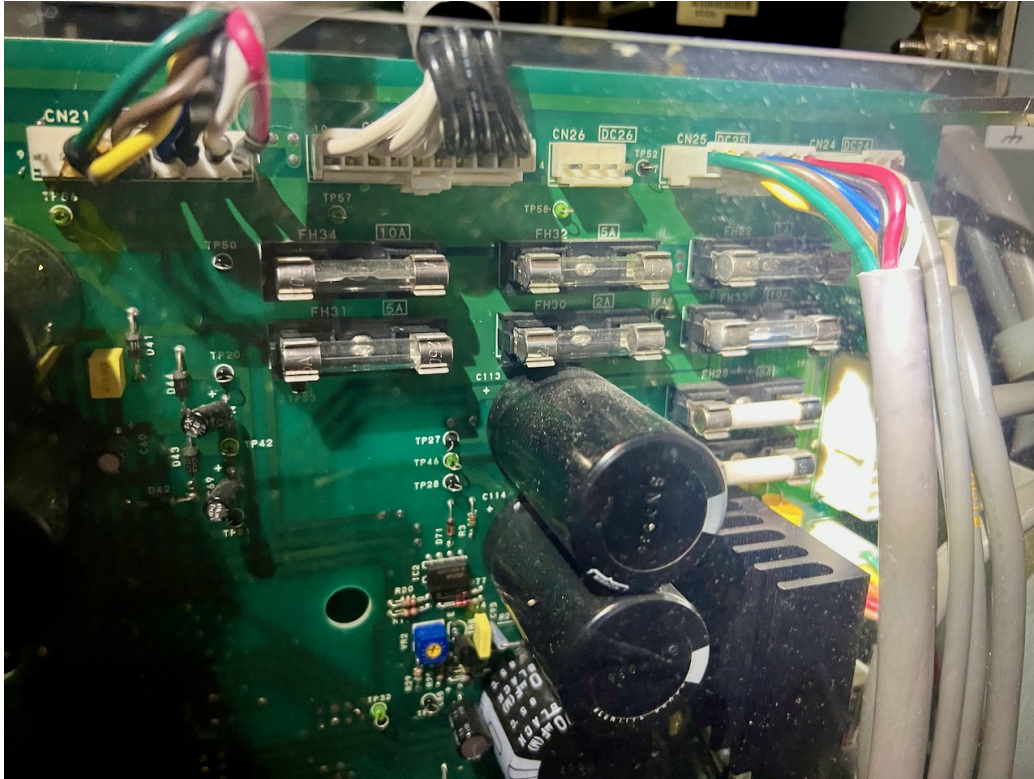
Figure 13.3. The two white fuses center right sometimes blow when zoomed out (<100 x) for an extended period

13.8 Accelerating voltage stuck at one value

It is possible for some components inside the high tension tank to fail. This has been known to peg the voltage to 30 kV.

There should be a ground wire between the Cockroft-Walton multiplier and the floating FEG power supply that is connected between 2 large resistors nearby. This wire was missing/vaporized at one point.

Several ICs were previously damaged. The schematics were marked with Δ's to indicate changed parts.

Be sure to use a high voltage probe and exercise extreme caution when working on the high tension tank. Also be sure to refill the tank with SF_6 to the marked pressure on the gauge.

Figure 13.4. There are several transistors hiding within

13.9 FEG emission current limited to ~1.9 A despite higher command

If the emission current from the FEG cannot go above ~1.9 A (normal operating condition is ~2.3 A or a bit higher), it is possibly a transistor buried in the high tension tank has failed.

Previous testing to determine the root cause:

- Removed the tip power cable and put the dummy load in (perpendicular to the guide pin axis). Attempted to run the current up and hit the same 1.9 A limit.

- Pulled the power supply out of the tank and hooked things up on the cart. Checked all the pins for the DACs (ICs 17 and 18) and found good values. Checked the output of the op-amps (ICs 5, 6, and 10) and found good values.

- Checked the voltage going to the last transistor before the tip and found a relatively low collector voltage (~2.8 V; expected at least 5 V; the output of IC 10 was at 15 V).

- Built a reproduction of the power filtering circuit (a couple capacitors and a load resistor) and checked the characteristics of the incoming voltage. The circuit behaved the same (unloaded voltage across the circuit of ~3.5 V that dropped to 2.5-2.9 when shown a load). Steve found that peculiar, but couldn't call it the real problem.

- Replaced the power supply coming into the filter with a lab power supply. This had the added benefit of letting us see the current drawn. Set the lab supply to 3.5 A and commanded the filament current to 1 A, supply showed 1 A. Went to 2 A, supply showed 1.9 A. 2.5 A also showed 1.9 A. This is the behavior we saw that started this line of investigation. This allowed us to narrow down the problem to 1 or more of 3 transistors.

- After replacement, a command of 2.5 A showed 2.5 A through the circuit.

- Adjust the read back variable resistor to fix a small offset.

Replacing these parts is best done with Steve Weimholt's assistance as high voltages are involved.

- Vent the eGun chamber (see Venting for maintenance).

- Set bakeout timer to 10 hours.

- Remove the hex head bolts holding the high tension line in place at the top of the instrument.

- Remove the tip being careful not to hit the sides.

- Replace the tip, aligning with 3 set screws as best possible while looking down through the end of the holder.

- Add SF_6 into the gun chamber until it visibly overflows (~2-3 seconds).

- Pump back down. At low enough pressure, a bake out to TMP will kick off (and run for 10 hours).

- Bake out to SIP for at least 24 more hours.

13.10 No FEG emission current at normal operating condition

If there is no emission current from the FEG, it is most likely that the tip has failed. This can be verified by checking the tip's resistance: it should be below 1 Ω.

The replacement part, available from Ted Pella, is TFE174C SE4 Tip for JEOL JAMP-7830F. As of summer 2021 the part was $5,500.

Replacing the part is best done with Steve Weimholt's assistance as the alignment in the holder is critical (see Figure 3.5).

- Vent the eGun chamber (see section 5.2).

- Set bakeout timer to 10 hours.

- Remove the hex head bolts holding the high tension line in place at the top of the instrument.

- Remove the tip being careful not to hit the sides.

- Replace the tip, aligning with 3 set screws as best possible while looking down through the end of the holder.

- Pump back down. At low enough pressure, a bake out to TMP will kick off (and run for 10 hours).

- Bake out to SIP for at least 24 more hours.

- Replacement instructions can be found at `C:\SEMPA\Instructions_and_-Manuals\FESAM\7830F FE tip Replacement.doc`.

Adjusting the accelerating voltage was also an important part of this process: high accelerating voltage sends the beam pretty straight down the column, while lower voltages cause the electron beam to spread out a bit, illuminating more of the FEG chamber (and knocking a lot of stuff off). Adjustements started around 10 keV and worked down to ~3 keV, as pressures permitted. This took several days.

Another much less obvious possibility is a blown opto-coupler. Several opto-couplers are used to electronically isolate the high voltage parts of the system from the circuits. Perhaps coincidentally, one of these seems to have been damaged during an arc-related shutdown. Examine page HT I/O PB (FE) 3 in the schematics.

13.11 Cannot get SEMPA electrons to E-T detector or targets

Stray currents or improper voltages anywhere along the SEMPA column can deflect the beam.

It is possible that a microscopic (though hopefully larger) bit of contamination can short the electrostatic lenses in the SEMPA column; this happened to the joint shown in Figure 13.5. In the worst case, this can prevent the electron beam from making it to the end of the column where the sensors are.

This was remedied by shutting down the instrument and removing the SEMPA optics, then testing continuity between adjacent lenses. Each lens should be electrically isolated from the next. There was nothing visible, but there was a short between two of the lenses. The fix was to blow compressed air across the joint and retest continuity. If that is insufficient, the lenses will need to be separated and the interface between them cleaned.
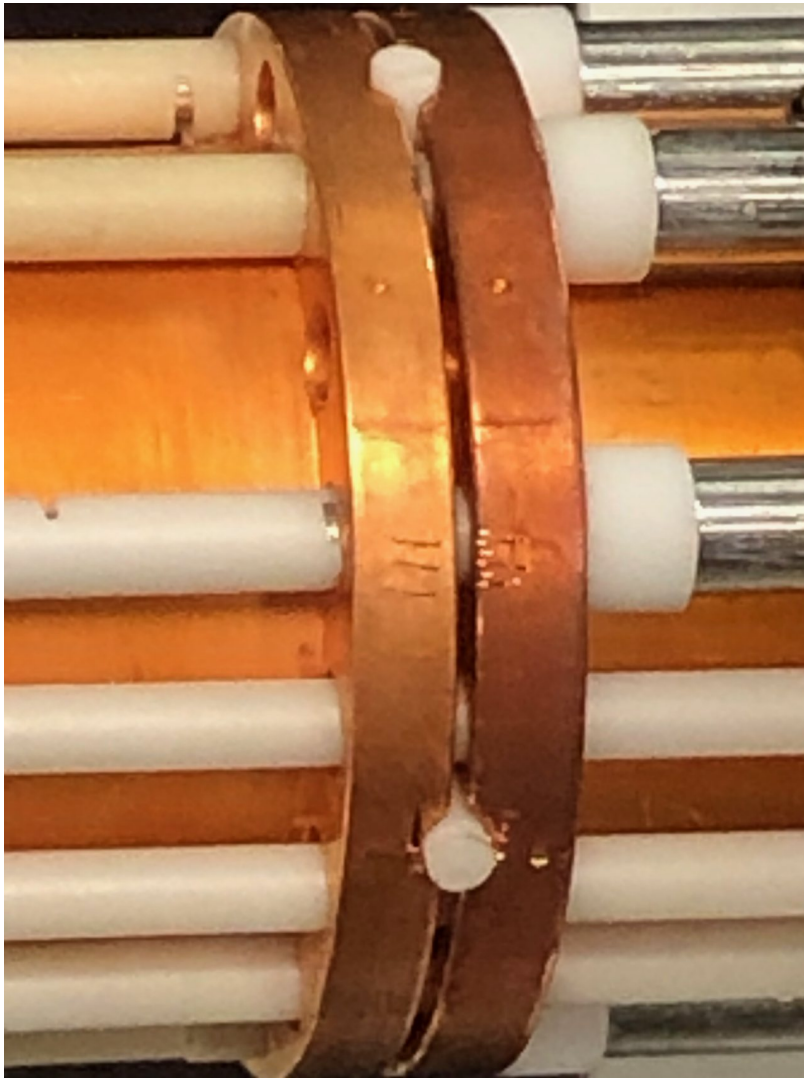
Figure 13.5. There was an invisible short in the space between two of the electrostatic lenses

Another possible culprit is an issue with the nanoammeters at the top of the SEMPA rack. There are 8 identical cards in the chassis, selectable by the dial on the

front. The original design for these was overly reliant on an accurate voltage supply (needed to be within a few percent of $\pm$ 15 volt). The unit was modified by Cliff at Technical Services to be adjustable to handle drift over time.

It is also possible that one or more of the cards can develop a short. They measure small currents at high voltages (thus the floating design) and can be damaged by arcs.

Figure 13.6. This unit houses 8 nanoammeters, each on a separate card
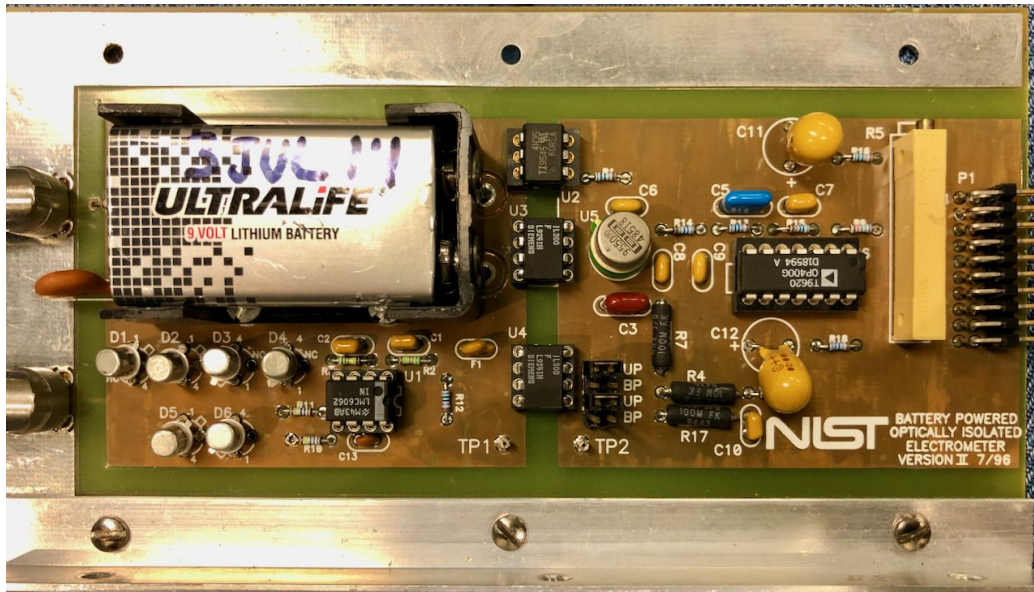
Figure 13.7. These are designed to measure tiny currents and are susceptible to damage during arcing events

Acronyms

E-T detector   Everhart-Thornley detector. 117, 120, 130, 143, 155, 157, 165, 166

FEG   field emission gun. 106, 107, 109, 124, 134, 138, 139, 141, 163, 165, 168, 169, 171

MCP   multi-channel plates. 156

MIED   Micro Ion Etching Device. 112, 116, 120, 136, 141, 148, 154, 161

NIST   National Institute of Standards and Technology. 103, 133, 148

PCD   probe current detector. 106, 134, 149, 156, 165

RA   right angle. 126, 127, 156

ROI   region of interest. 145, 146

SEM   scanning electron microscope. 99, 111, 117, 120, 133, 144, 155, 165

SEMPA   Scanning Electron Microscopy with Polarization Analysis. 99, 103, 105, 111, 112, 117, 126, 130, 132–134, 143, 152, 154–156, 160–163, 165, 171, 172

SIP   sputter ion pump. 109, 123, 141, 159, 162, 170, 171

REFERENCES CITED

[1] *Data Center Power: Global Strategic Business Report*. (Visited on 11/13/2022) (cit. on p. 4).

[2] George Kamiya. *Data Centres and Data Transmission Networks, IEA, Paris*. (Visited on 11/13/2022) (cit. on p. 4).

[3] *Spintronics for Low-Power Computing*. Design, Automation, Test in Europe Conference, and Exhibition (DATE). 2014 (cit. on pp. 4, 16).

[4] R. Tomasello et al. "A strategy for the design of skyrmion racetrack memories". In: *Scientific Reports* 4.1 (Oct. 2014), p. 6784. ISSN: 2045-2322. DOI: 10.1038/sr ep06784. URL: https://doi.org/10.1038/srep06784 (cit. on p. 4).

[5] Guoqiang Yu et al. "Room-temperature skyrmion shift device for memory application". In: *Nano letters* 17.1 (2017), pp. 261–268 (cit. on p. 4).

[6] R Tomasello et al. "Performance of synthetic antiferromagnetic racetrack memory: domain wall versus skyrmion". In: *Journal of Physics D: Applied Physics* 50.32 (2017), p. 325302 (cit. on p. 4).

[7] R. C. Sherwood, J. P. Remeika, and H. J. Williams. "Domain Behavior in Some Transparent Magnetic Oxides". In: *Journal of Applied Physics* 30.2 (1959), pp. 217–225. DOI: 10.1063/1.1735136. eprint: https://doi.org/10.1063/1.1735136. URL: https://doi.org/10.1063/1.1735136 (cit. on p. 15).

[8] C. Kooy and U. Enz. "Experimental and theoretical study of the domain configuration in thin layers of BaFe12019". In: *PHILIPS RESEARCH REPORTS*. Vol. 15. 1960, pp. 7–19 (cit. on p. 15).

[9] C. D. Mee. "Recent measurements of the magneto-optical properties of some garnets". In: *Contemporary Physics* 8.4 (1967), pp. 385–400. DOI: 10.1080/0010 7516708202161. eprint: https://doi.org/10.1080/00107516708202161. URL: https://doi.org/10.1080/00107516708202161 (cit. on p. 15).

[10] J. M. Nemchik. "Circular Domain Configuration in GdIG". In: *Journal of Applied Physics* 40.3 (1969), pp. 1086–1087. DOI: 10.1063/1.1657535. eprint: https://doi.org/10.1063/1.1657535. URL: https://doi.org/10.1063/1.1 657535 (cit. on p. 15).

[11] Andrew H Bobeck and H E D Scovil. "MAGNETIC BUBBLES". en. In: *SCIENTIFIC AMERICAN* (1971), p. 15 (cit. on p. 15).

[12] L.A. Russell. "High-Speed Magnetic-Core Memory Technology". In: ed. by L. Marton. Vol. 21. Advances in Electronics and Electron Physics. Academic Press, 1966, pp. 249–286. DOI: `https://doi.org/10.1016/S0065-2539(08)61011-2`. URL: `https://www.sciencedirect.com/science/article/pii/S0065253908610112` (cit. on p. 15).

[13] *IBM Archives: IBM 2305 fixed head storage*. URL: `https://www.ibm.com/ibm/history/exhibits/storage/storage_2305.html` (cit. on p. 15).

[14] K.F. Baker. "A review of magnetic bubble memories and their applications". English. In: *Radio and Electronic Engineer* 51 (3 Mar. 1981), 105–115(10). ISSN: 0033-7722. URL: `https://digital-library.theiet.org/content/journals/10.1049/ree.1981.0014` (cit. on p. 15).

[15] R. Suzuki. "Recent development in magnetic-bubble memory". In: *Proceedings of the IEEE* 74.11 (1986), pp. 1582–1590. DOI: `10.1109/PROC.1986.13670` (cit. on p. 15).

[16] J.Egil Juliussen. "Bubble memory as small mass storage". In: *Microelectronics Reliability* 16.4 (1977), pp. 427–430. ISSN: 0026-2714. DOI: `https://doi.org/10.1016/0026-2714(77)90441-3`. URL: `https://www.sciencedirect.com/science/article/pii/0026271477904413` (cit. on p. 15).

[17] Tina-Marie D'Ercole. *A solid state data recorder for space-based applications using magnetic bubble memory.* Tech. rep. NAVAL POSTGRADUATE SCHOOL MONTEREY CA, 1986 (cit. on p. 15).

[18] WC Mavity. "Bubble memory system applications". In: *NASA STI/Recon Technical Report N* 77 (1977), p. 19391 (cit. on p. 15).

[19] H Kohara et al. "True swap gate design for on chip cache organization megabit bubble memory". In: *IEEE Transactions on Magnetics* 17.6 (1981), pp. 3038–3040 (cit. on p. 15).

[20] Mona Berciu and Sajeev John. "Charged bosons in a doped Mott insulator: Electronic properties of domain-wall solitons and meron vortices". In: *Physical Review B* 57.16 (1998), p. 9521 (cit. on p. 15).

[21] Ronald Johannes Keizer et al. *Evolution of magnetism and its interplay with superconductivity in heavy-fermion U (Pt, Pd) 3.* Universiteit van Amsterdam [Host], 1999 (cit. on p. 15).

[22] A Knigavko and Baruch Rosenstein. "Magnetic Skyrmion Lattices in Heavy Fermion Superconductor UPt 3". In: *Physical review letters* 82.6 (1999), p. 1261 (cit. on p. 15).

[23] Tony Hilton Royle Skyrme. "A non-linear field theory". In: *Proceedings of the Royal Society of London. Series A. Mathematical and Physical Sciences* 260.1300 (1961), pp. 127–138 (cit. on pp. 15, 18).

[24] T.H.R. Skyrme. "A unified field theory of mesons and baryons". en. In: *Nuclear Physics* 31 (Mar. 1962), pp. 556–569. ISSN: 00295582. DOI: 10.1016/0029-5582(62)90775-7. URL: https://linkinghub.elsevier.com/retrieve/pii/0029558262907757 (visited on 11/10/2021) (cit. on p. 15).

[25] Qi Li, John Toner, and D. Belitz. "Skyrmion versus vortex flux lattices in p-wave superconductors". In: *Phys. Rev. B* 79 (1 Jan. 2009), p. 014517. DOI: 10.1103/PhysRevB.79.014517. URL: https://link.aps.org/doi/10.1103/PhysRevB.79.014517 (cit. on pp. 15, 86).

[26] Qi Li, John Toner, and D. Belitz. "Elasticity and Melting of Skyrmion Flux Lattices in p-Wave Superconductors". In: *Phys. Rev. Lett.* 98 (18 May 2007), p. 187002. DOI: 10.1103/PhysRevLett.98.187002. URL: https://link.aps.org/doi/10.1103/PhysRevLett.98.187002 (cit. on p. 15).

[27] Eslam Khalaf et al. "Charged skyrmions and topological origin of superconductivity in magic-angle graphene". In: *Science advances* 7.19 (2021), eabf5299 (cit. on p. 15).

[28] Eric Mascot et al. "Topological superconductivity in skyrmion lattices". In: *npj Quantum Materials* 6.1 (2021), pp. 1–6 (cit. on p. 15).

[29] Alexei N Bogdanov and DA Yablonskii. "Thermodynamically stable "vortices" in magnetically ordered crystals. The mixed state of magnets". In: *Zh. Eksp. Teor. Fiz* 95.1 (1989), p. 178 (cit. on p. 15).

[30] Ulrich K Roessler, AN Bogdanov, and C Pfleiderer. "Spontaneous skyrmion ground states in magnetic metals". In: *Nature* 442.7104 (2006), pp. 797–801 (cit. on p. 15).

[31] Benedikt Binz, Ashvin Vishwanath, and Vivek Aji. "Theory of the helical spin crystal: a candidate for the partially ordered state of MnSi". In: *Physical review letters* 96.20 (2006), p. 207202 (cit. on p. 15).

[32] S. Mühlbauer et al. "Skyrmion Lattice in a Chiral Magnet". en. In: *Science* 323.5916 (Feb. 2009), pp. 915–919. ISSN: 0036-8075, 1095-9203. DOI: 10.1126/science.1166767. URL: https://www.science.org/doi/10.1126/science.1166767 (visited on 11/10/2021) (cit. on pp. 15, 17, 24).

[33] XZ Yu et al. "Real-space observation of a two-dimensional skyrmion crystal". In: *Nature* 465.7300 (2010), pp. 901–904 (cit. on p. 15).

[34] Akira Tonomura et al. "Real-space observation of skyrmion lattice in helimagnet MnSi thin samples". In: *Nano letters* 12.3 (2012), pp. 1673–1677 (cit. on pp. 15, 24).

[35] Gareth Williams. "Stability of skyrmions in thin films of superfluid A 3". In: *Physical Review B* 48.10 (1993), p. 7704 (cit. on p. 15).

[36] VL Pokrovsky and WM Saslow. *Information-bearing structures and magnetism of thin films. Annual report, 1997–1998*. Tech. rep. Texas A and M Univ., College Station, TX (United States). Dept. of Physics, 1998 (cit. on p. 15).

[37] V Ilkovič, S Tuleja, and D Blažek. "Magnetic properties of superlattice-configured thin films with variable interlayer couplings". In: *Journal of magnetism and magnetic materials* 193.1-3 (1999), pp. 177–180 (cit. on p. 15).

[38] SD Bader and SSP Parkin. "Spintronics". In: *Annu. Rev. Condens. Matter Phys.* 1.1 (2010), pp. 71–88 (cit. on p. 15).

[39] Igor Žutić, Jaroslav Fabian, and S Das Sarma. "Spintronics: Fundamentals and applications". In: *Reviews of modern physics* 76.2 (2004), p. 323 (cit. on p. 15).

[40] David D Awschalom, Michael E Flatté, and Nitin Samarth. "Spintronics". In: *Scientific American* 286.6 (2002), pp. 66–73 (cit. on p. 15).

[41] Fabio Pulizzi. "Spintronics". In: *Nature materials* 11.5 (2012), pp. 367–367 (cit. on p. 15).

[42] Mamoru Matsuo, Junichi Ieda, and Sadamichi Maekawa. "Mechanical generation of spin current". In: *Frontiers in Physics* 3 (2015). ISSN: 2296-424X. DOI: 10.3389/fphy.2015.00054. URL: https://www.frontiersin.org/articles/10.3389/fphy.2015.00054 (cit. on p. 15).

[43] Niklas Romming et al. "Writing and deleting single magnetic skyrmions". In: *Science* 341.6146 (2013), pp. 636–639 (cit. on p. 16).

[44] X.Z. Yu et al. "Skyrmion flow near room temperature in an ultralow current density". In: *Nature Communications* 3.1 (Aug. 2012), p. 988. ISSN: 2041-1723. DOI: 10.1038/ncomms1990. URL: https://doi.org/10.1038/ncomms1990 (cit. on p. 16).

[45] N S Kiselev et al. "Chiral skyrmions in thin magnetic films: new objects for magnetic storage technologies?" In: *Journal of Physics D: Applied Physics* 44.39 (Sept. 2011), p. 392001. DOI: 10.1088/0022-3727/44/39/392001. URL: https://doi.org/10.1088/0022-3727/44/39/392001 (cit. on p. 17).

[46] Xiuzhen Yu et al. "Magnetic stripes and skyrmions with helicity reversals". In: *Proceedings of the National Academy of Sciences* 109.23 (2012), pp. 8856–8860 (cit. on p. 17).

[47] R Tolley, SA Montoya, and EE Fullerton. "Room-temperature observation and current control of skyrmions in Pt/Co/Os/Pt thin films". In: *Physical Review Materials* 2.4 (2018), p. 044404 (cit. on p. 17).

[48] Naoto Nagaosa and Yoshinori Tokura. "Topological properties and dynamics of magnetic skyrmions". en. In: *Nature Nanotechnology* 8.12 (Dec. 2013), pp. 899–911. ISSN: 1748-3387, 1748-3395. DOI: 10.1038/nnano.2013.243. URL: http://www.nature.com/articles/nnano.2013.243 (visited on 11/10/2021) (cit. on pp. 18, 24).

[49] Gong Chen et al. "Tailoring the chirality of magnetic domain walls by interface engineering". In: *Nature Communications* 4.2671 (2013) (cit. on pp. 18, 26).

[50] Tôru Moriya. "New Mechanism of Anisotropic Superexchange Interaction". In: *Phys. Rev. Lett.* 4 (5 Mar. 1960), pp. 228–230. DOI: 10.1103/PhysRevLett.4.228. URL: https://link.aps.org/doi/10.1103/PhysRevLett.4.228 (cit. on p. 24).

[51] M. Bode et al. "Chiral magnetic order at surfaces driven by inversion asymmetry". In: *Nature* 447.7141 (May 2007), pp. 190–193. ISSN: 1476-4687. DOI: 10.1038/nature05802. URL: https://doi.org/10.1038/nature05802 (cit. on p. 24).

[52] M. Heide, G. Bihlmayer, and S. Blügel. "Dzyaloshinskii-Moriya interaction accounting for the orientation of magnetic domains in ultrathin films: Fe/W(110)". In: *Phys. Rev. B* 78 (14 Oct. 2008), p. 140403. DOI: 10.1103/PhysRevB.78.140403. URL: https://link.aps.org/doi/10.1103/PhysRevB.78.140403 (cit. on p. 24).

[53] Taro Nakajima et al. "Skyrmion lattice structural transition in MnSi". In: *Science Advances* 3.6 (2017), e1602562. DOI: 10.1126/sciadv.1602562. eprint: https://www.science.org/doi/pdf/10.1126/sciadv.1602562. URL: https://www.science.org/doi/abs/10.1126/sciadv.1602562 (cit. on p. 24).

[54] Won-Young Choi et al. "Skyrmion Phase in MnSi Thin Films Grown on Sapphire by a Conventional Sputtering". In: *Nanoscale Research Letters* 16.1 (Jan. 2021), p. 7. ISSN: 1556-276X. DOI: 10.1186/s11671-020-03462-2. URL: https://doi.org/10.1186/s11671-020-03462-2 (cit. on p. 24).

[55] D. Okuyama et al. "Deformation of the moving magnetic skyrmion lattice in MnSi under electric current flow". In: *Communications Physics* 2.1 (July 2019), p. 79. ISSN: 2399-3650. DOI: 10.1038/s42005-019-0175-z. URL: https://doi.org/10.1038/s42005-019-0175-z (cit. on p. 24).

[56] B. Lebech, J. Bernhard, and T. Freltoft. "Magnetic structures of cubic FeGe studied by small-angle neutron scattering". In: *Journal of Physics Condensed Matter* 1.35 (Sept. 1989), pp. 6105–6122. DOI: 10.1088/0953-8984/1/35/010 (cit. on p. 24).

[57] X. Z. Yu et al. "Near room-temperature formation of a skyrmion crystal in thin-films of the helimagnet FeGe". en. In: *Nature Materials* 10.2 (Feb. 2011), pp. 106–109. ISSN: 1476-1122, 1476-4660. DOI: 10.1038/nmat2916. URL: http://www.nature.com/articles/nmat2916 (visited on 11/10/2021) (cit. on p. 24).

[58] Maxime Leroux et al. "Skyrmion Lattice Topological Hall Effect near Room Temperature". In: *Scientific Reports* 8.1 (Oct. 2018), p. 15510. ISSN: 2045-2322. DOI: 10.1038/s41598-018-33560-2. URL: https://doi.org/10.1038/s41598-018-33560-2 (cit. on p. 24).

[59] Alison C. Twitchett-Harrison et al. "Confinement of Skyrmions in Nanoscale FeGe Device-like Structures". In: *ACS Applied Electronic Materials* 4.9 (2022), pp. 4427–4437. DOI: 10.1021/acsaelm.2c00692. eprint: https://doi.org/10.1021/acsaelm.2c00692. URL: https://doi.org/10.1021/acsaelm.2c00692 (cit. on p. 24).

[60] Sujan Budhathoki et al. "Room-temperature skyrmions in strain-engineered FeGe thin films". In: *Phys. Rev. B* 101 (22 June 2020), p. 220405. DOI: 10.1103/PhysRevB.101.220405. URL: https://link.aps.org/doi/10.1103/PhysRevB.101.220405 (cit. on p. 24).

[61] András Kovács et al. "Mapping the magnetization fine structure of a lattice of Bloch-type skyrmions in an FeGe thin film". In: *Applied Physics Letters* 111.19 (2017), p. 192410. DOI: 10.1063/1.5004394. eprint: https://doi.org/10.1063/1.5004394. URL: https://doi.org/10.1063/1.5004394 (cit. on p. 24).

[62] Albert Fert and Peter M Levy. "Role of anisotropic exchange interactions in determining the properties of spin-glasses". In: *Physical Review Letters* 44.23 (1980), p. 1538 (cit. on p. 24).

[63] Tsuyoshi Okubo, Sungki Chung, and Hikaru Kawamura. "Multiple-q States and the Skyrmion Lattice of the Triangular-Lattice Heisenberg Antiferromagnet under Magnetic Fields". In: *Phys. Rev. Lett.* 108 (1 Jan. 2012), p. 017206. DOI: 10.1103/PhysRevLett.108.017206. URL: https://link.aps.org/doi/10.1103/PhysRevLett.108.017206 (cit. on p. 25).

[64] S. von Malottki et al. "Enhanced skyrmion stability due to exchange frustration". In: *Scientific Reports* 7.1 (Sept. 2017), p. 12299. ISSN: 2045-2322. DOI: 10.1038/s41598-017-12525-x. URL: https://doi.org/10.1038/s41598-017-12525-x (cit. on p. 25).

[65] Thomas T. J. Mutter, Andrey O. Leonov, and Katsuya Inoue. "Skyrmion instabilities and distorted spiral states in a frustrated chiral magnet". In: *Phys. Rev. B* 100 (6 Aug. 2019), p. 060407. DOI: 10.1103/PhysRevB.100.060407. URL: https://link.aps.org/doi/10.1103/PhysRevB.100.060407 (cit. on p. 25).

[66] Stefan Heinze et al. "Spontaneous atomic-scale magnetic skyrmion lattice in two dimensions". en. In: *Nature Physics* 7.9 (Sept. 2011), pp. 713–718. ISSN: 1745-2473, 1745-2481. DOI: 10.1038/nphys2045. URL: http://www.nature.com/articles/nphys2045 (visited on 11/10/2021) (cit. on p. 25).

[67] Souvik Paul et al. "Role of higher-order exchange interactions for skyrmion stability". In: *Nature Communications* 11.1 (Sept. 2020), p. 4756. ISSN: 2041-1723. DOI: 10.1038/s41467-020-18473-x. URL: https://doi.org/10.1038/s41467-020-18473-x (cit. on p. 25).

[68] Nguyen Duy Khanh et al. "Nanometric square skyrmion lattice in a centrosymmetric tetragonal magnet". In: *Nature Nanotechnology* 15.6 (2020), pp. 444–449 (cit. on p. 25).

[69] F. J. A. den Broeder et al. "Perpendicular Magnetic Anisotropy of Co-Au Multi-layers Induced by Interface Sharpening". In: *Phys. Rev. Lett.* 60 (26 June 1988), pp. 2769–2772. DOI: 10.1103/PhysRevLett.60.2769. URL: https://link.aps.org/doi/10.1103/PhysRevLett.60.2769 (cit. on p. 25).

[70] N. Nakajima et al. "Perpendicular Magnetic Anisotropy Caused by Interfacial Hybridization via Enhanced Orbital Moment in Co/Pt Multilayers: Magnetic Circular X-Ray Dichroism Study". In: *Phys. Rev. Lett.* 81 (23 Dec. 1998), pp. 5229–5232. DOI: 10.1103/PhysRevLett.81.5229. URL: https://link.aps.org/doi/10.1103/PhysRevLett.81.5229 (cit. on p. 25).

[71] Nam-Hui Kim et al. "Interfacial Dzyaloshinskii-Moriya interaction, surface anisotropy energy, and spin pumping at spin orbit coupled Ir/Co interface". In: *Applied Physics Letters* 108.14 (2016), p. 142406 (cit. on p. 25).

[72] Woo Seung Ham et al. "Dzyaloshinskii–Moriya interaction in noncentrosymmetric superlattices". In: *npj Computational Materials* 7.1 (Aug. 2021), p. 129. ISSN: 2057-3960. DOI: 10.1038/s41524-021-00592-8. URL: https://doi.org/10.1038/s41524-021-00592-8 (cit. on p. 25).

[73] P. F. Carcia. "Perpendicular magnetic anisotropy in Pd/Co and Pt/Co thin-film layered structures". In: *Journal of Applied Physics* 63.10 (1988), pp. 5066–5073. DOI: 10.1063/1.340404. eprint: https://doi.org/10.1063/1.340404. URL: https://doi.org/10.1063/1.340404 (cit. on p. 25).

[74] MA Slonczewski and AP Malozemoff. "Magnetic domain walls in bubble materials". In: *Suppl* (1979) (cit. on p. 25).

[75] Motohiko Ezawa. "Giant Skyrmions Stabilized by Dipole-Dipole Interactions in Thin Ferromagnetic Films". en. In: *Physical Review Letters* 105.19 (Nov. 2010), p. 197202. ISSN: 0031-9007, 1079-7114. DOI: 10.1103/PhysRevLett.105.197202. URL: https://link.aps.org/doi/10.1103/PhysRevLett.105.197202 (visited on 10/18/2022) (cit. on p. 25).

[76] Jordan J. Chess et al. "Determination of domain wall chirality using in situ Lorentz transmission electron microscopy". In: *AIP Advances* 7.5 (2017), p. 056807. DOI: 10.1063/1.4977500 (cit. on p. 26).

[77] S. A. Montoya et al. "Resonant properties of dipole skyrmions in amorphous Fe/Gd multilayers". In: *PHYSICAL REVIEW B* 95.224405 (2017) (cit. on p. 26).

[78] J. C. T Lee et al. "Synthesizing skyrmion bound pairs in Fe-Gd thin films". In: *Applied Physics Letters* 109.2 (2016), p. 022402. DOI: 10.1063/1.4955462. eprint: https://doi.org/10.1063/1.4955462. URL: https://doi.org/10.1063/1.4955462 (cit. on pp. 26, 27, 86).

[79] Soong-Geun Je et al. "Direct demonstration of topological stability of magnetic skyrmions via topology manipulation". In: *ACS nano* 14.3 (2020), pp. 3251–3258 (cit. on p. 26).

[80] MH Seaberg et al. "Spontaneous fluctuations in a magnetic fe/gd skyrmion lattice". In: *Physical Review Research* 3.3 (2021), p. 033249 (cit. on p. 26).

[81] Yuqing Zhou et al. "A comparative study of the domain wall motion in ferrimagnets (Fe, Co) 1- x (Gd, Tb) x". In: *Nanoscale* 14.37 (2022), pp. 13526–13531 (cit. on p. 26).

[82] Bert Koopmans. "Femto-magnetism meets spintronics-toward integrated magneto-photonics". In: *IEEE Transactions on Magnetics* 55.12 (2019), p. 1 (cit. on p. 26).

[83] Felipe M de Souza and Ram K Gupta. "Magnetic Nanomaterials for Flexible Spintronics". In: *Emerging Applications of Low Dimensional Magnets*. CRC Press, pp. 303–318 (cit. on p. 26).

[84] SA Montoya et al. "Tailoring magnetic energies to form dipole skyrmions and skyrmion lattices". In: *Physical Review B* 95.2 (2017), p. 024415 (cit. on p. 26).

[85] Jordan J Chess. "Mapping Topological Magnetization and Magnetic Skyrmions". PhD thesis. University of Oregon, 2017 (cit. on pp. 26, 43).

[86] Gong Chen and Andreas K. Schmid. "Imaging and Tailoring the Chirality of Domain Walls in Magnetic Films". In: *Advanced Materials* 27.38 (2015), pp. 5738–5743. DOI: https://doi.org/10.1002/adma.201500160. eprint: https://onlinelibrary.wiley.com/doi/pdf/10.1002/adma.201500160. URL: https://onlinelibrary.wiley.com/doi/abs/10.1002/adma.201500160 (cit. on p. 26).

[87] Alice T Greenberg. "The Application of Interferometric Electron Microscopy for Nanomagnetic Imaging". PhD thesis. University of Oregon, 2020 (cit. on pp. 27, 43, 75).

[88] Xiuzhen Yu et al. "Observation of the magnetic skyrmion lattice in a MnSi nanowire by Lorentz TEM". In: *Nano letters* 13.8 (2013), pp. 3755–3759 (cit. on p. 27).

[89] Jin Tang et al. "Lorentz transmission electron microscopy for magnetic skyrmions imaging". In: *Chinese Physics B* 28.8 (2019), p. 087503 (cit. on p. 27).

[90] Yoshinori Tokura and Naoya Kanazawa. "Magnetic skyrmion materials". In: *Chemical Reviews* 121.5 (2020), pp. 2857–2897 (cit. on p. 27).

[91] Ryan D. Desautels et al. "Realization of ordered magnetic skyrmions in thin films at ambient conditions". In: *Phys. Rev. Materials* 3 (10 Oct. 2019), p. 104406. DOI: 10.1103/PhysRevMaterials.3.104406. URL: https://link.aps.org/doi/10.1103/PhysRevMaterials.3.104406 (cit. on p. 27).

[92] Seonghoon Woo et al. "Deterministic creation and deletion of a single magnetic skyrmion observed by direct time-resolved X-ray microscopy". In: *Nature Electronics* 1.5 (2018), pp. 288–296 (cit. on p. 27).

[93] V Ukleev et al. "Element-specific soft x-ray spectroscopy, scattering, and imaging studies of the skyrmion-hosting compound Co 8 Zn 8 Mn 4". In: *Physical Review B* 99.14 (2019), p. 144408 (cit. on p. 27).

[94] MT Birch et al. "Real-space imaging of confined magnetic skyrmion tubes". In: *Nature communications* 11.1 (2020), pp. 1–8 (cit. on p. 27).

[95] Mahdi Mehrnia, Jeremy Trimble, and Jesse Berezovsky. "3D Kerr Microscopy of Magnetic Vortex States in the Presence and Absence of Uniaxial Anisotropy". In: *Conference on Lasers and Electro-Optics*. Optica Publishing Group, 2020, JW2F.1. DOI: 10 . 1364 / CLEO _ AT . 2020 . JW2F . 1. URL: https://opg.optica.org/abstract.cfm?URI=CLEO_AT-2020-JW2F.1 (cit. on p. 28).

[96] DA Allwood et al. "Magneto-optical Kerr effect analysis of magnetic nanostructures". In: *Journal of Physics D: Applied Physics* 36.18 (2003), p. 2175 (cit. on p. 28).

[97] Mark R Freeman and Wayne K Hiebert. "Stroboscopic microscopy of magnetic dynamics". In: *Spin Dynamics in Confined Magnetic Structures I*. Springer, 2002, pp. 93–126 (cit. on p. 28).

[98] S Imada et al. "Magnetic microspectroscopy by a combination of XMCD and PEEM". In: *Surface Review and Letters* 9.02 (2002), pp. 877–881 (cit. on p. 28).

[99] Frederik Wegelin et al. "Stroboscopic XMCD–PEEM imaging of standing and propagating spinwave modes in permalloy thin-film structures". In: *Surface Science* 601.20 (2007). Proceedings of the Fifth International Conference on LEEM/PEEM, pp. 4694–4699. ISSN: 0039-6028. DOI: https://doi.org/10.1016/j.susc.2007.05.060. URL: https://www.sciencedirect.com/science/article/pii/S0039602807006036 (cit. on p. 28).

[100] Robert Streubel et al. "Equilibrium magnetic states in individual hemispherical permalloy caps". In: *Applied Physics Letters* 101.13 (2012), p. 132419 (cit. on p. 29).

[101] E Bauer. "Spleem". In: *Magnetic Microscopy of Nanostructures*. Springer, 2005, pp. 111–136 (cit. on p. 29).

[102] E Bauer, T Duden, and R Zdyb. "Spin-polarized low energy electron microscopy of ferromagnetic thin films". In: *Journal of Physics D: Applied Physics* 35.19 (2002), p. 2327 (cit. on p. 29).

[103] Qiang Wu, Chenlu Ji, and Michael Scott Altman. "SPLEEM Imaging of Thin Film Magnetic Interfacial Effects". In: (2013) (cit. on p. 29).

[104] E Bauer. "Low energy electron microscopy". In: *Reports on Progress in Physics* 57.9 (Sept. 1994), p. 895. DOI: 10.1088/0034-4885/57/9/002. URL: https://dx.doi.org/10.1088/0034-4885/57/9/002 (cit. on p. 29).

[105] Kazuyuki Koike. "Spin-polarized scanning electron microscopy". In: *Microscopy* 62.1 (Jan. 2013), pp. 177–191. ISSN: 2050-5698. DOI: 10.1093/jmicro/dfs092. eprint: https://academic.oup.com/jmicro/article-pdf/62/1/177/5855419/dfs092.pdf. URL: https://doi.org/10.1093/jmicro/dfs092 (cit. on p. 29).

[106] M R Scheinfein et al. "Scanning Electron Microscopy with Polarization Analysis (SEMPA)". In: *Scanning electron microscopy* (Apr. 1990), p. 28 (cit. on pp. 29, 38).

[107] Teruo Kohashi, Makoto Konoto, and Kazuyuki Koike. "High-resolution spin-polarized scanning electron microscopy (spin SEM)". In: *Journal of Electron Microscopy* 59.1 (Oct. 2009), pp. 43–52. ISSN: 0022-0744. DOI: 10.1093/jmicro/dfp047. eprint: https://academic.oup.com/jmicro/article-pdf/59/1/43/5853696/dfp047.pdf. URL: https://doi.org/10.1093/jmicro/dfp047 (cit. on p. 29).

[108] Hideo Matsuyama and Kazuyuki Koike. "A data acquisition and display system for spin-polarized scanning electron microscopy (spin SEM)". In: *Review of scientific instruments* 62.4 (1991), pp. 970–981 (cit. on p. 29).

[109] John Unguris. "Scanning electron microscopy with polarization analysis (SEMPA) and its applications". en. In: *Experimental Methods in the Physical Sciences*. Vol. 36. Elsevier, 2001, pp. 167–XVI. ISBN: 978-0-12-475983-1. DOI: 10.1016/S1079-4042(01)80040-0. URL: https://linkinghub.elsevier.com/retrieve/pii/S1079404201800400 (visited on 11/10/2021) (cit. on pp. 29, 33).

[110] Kazuyuki Koike and Kazunobu Hayakawa. "Scanning Electron Microscope Observation of Magnetic Domains Using Spin-Polarized Secondary Electrons". en. In: *Japanese Journal of Applied Physics* 23.Part 2, No. 3 (Mar. 1984), pp. L187–L188. ISSN: 0021-4922. DOI: 10.1143/JJAP.23.L187. URL: https://iopscience.iop.org/article/10.1143/JJAP.23.L187 (visited on 11/10/2021) (cit. on p. 31).

[111] David R. Penn, S. Peter Apell, and S. M. Girvin. "Theory of spin-polarized secondary electrons in transition metals". In: *Phys. Rev. Lett.* 55 (5 July 1985), pp. 518–521. DOI: 10.1103/PhysRevLett.55.518. URL: https://link.aps.org/doi/10.1103/PhysRevLett.55.518 (cit. on p. 31).

[112] David R. Penn, S. Peter Apell, and S. M. Girvin. "Spin polarization of secondary electrons in transition metals: Theory". In: *Physical Review B* 32.12 (Dec. 1985). Publisher: American Physical Society, pp. 7753–7768. DOI: 10.1103/PhysRevB.32.7753. URL: https://link.aps.org/doi/10.1103/PhysRevB.32.7753 (visited on 10/23/2022) (cit. on p. 32).

[113] Demetrios Matsakis et al. "A renaming proposal: "The Auger–Meitner effect"". In: *Physics Today* 72.9 (2019), pp. 10–11. DOI: 10.1063/PT.3.4281. eprint: https://physicstoday.scitation.org/doi/pdf/10.1063/PT.3.4281. URL: https://physicstoday.scitation.org/doi/abs/10.1063/PT.3.4281 (cit. on p. 33).

[114] Kenjiro Oura et al. *Surface science: an introduction*. Springer Science & Business Media, 2013 (cit. on p. 33).

[115] Joachim Kessler. *Polarized electrons*. Vol. 1. Springer Science & Business Media, 1985 (cit. on p. 34).

[116] D. L. Abraham and H. Hopster. "Magnetic probing depth in spin-polarized secondary electron spectroscopy". In: *Phys. Rev. Lett.* 58 (13 Mar. 1987), pp. 1352–1354. DOI: 10.1103/PhysRevLett.58.1352. URL: https://link.aps.org/doi/10.1103/PhysRevLett.58.1352 (cit. on p. 34).

[117] Ethan Rublee et al. "ORB: An efficient alternative to SIFT or SURF". In: *2011 International conference on computer vision*. Ieee. 2011, pp. 2564–2571 (cit. on p. 51).

[118] Börge Göbel, Ingrid Mertig, and Oleg A Tretiakov. "Beyond skyrmions: Review and perspectives of alternative magnetic quasiparticles". In: *Physics Reports* 895 (2021), pp. 1–28 (cit. on p. 75).

[119] Radha Balakrishnan, Rossen Dandoloff, and Avadh Saxena. "Exact Hopfions in a 3D Heisenberg Ferromagnet". In: *arXiv preprint arXiv:2202.07195* (2022) (cit. on p. 75).